

DISSERTATION

EXPANDING THE KNOCK/EMISSIONS LIMITS FOR THE REALIZATION OF
ULTRA-LOW EMISSIONS, HIGH-EFFICIENCY HEAVY-DUTY NATURAL GAS
ENGINES

Submitted by

Juan Felipe Rodriguez Rueda

Department of Mechanical Engineering

In partial fulfillment of the requirements

For the Degree of Doctor of Philosophy

Colorado State University

Fort Collins, Colorado

Fall 2023

Doctoral Committee:

Advisor: Daniel B. Olsen

Bret Windom
Daniel Baker
Jason Quinn

Copyright by Juan Felipe Rodriguez Rueda 2023

All Rights Reserved

ABSTRACT

EXPANDING THE KNOCK/EMISSIONS LIMITS FOR THE REALIZATION OF ULTRA-LOW EMISSIONS, HIGH-EFFICIENCY HEAVY-DUTY NATURAL GAS ENGINES

Heavy-duty on-highway natural gas (NG) engines are a promising alternative to diesel engines to reduce greenhouse gas and harmful pollutant emissions if the limitations (knock and misfire) for achieving diesel-like efficiencies are addressed. This study shows innovative technologies for developing high-efficiency stoichiometric, spark-ignited (SI) natural gas engines.

To develop the base knowledge required to reach the desired efficiency, a Single Cylinder Engine (SCE) is the most effective platform for acquiring reliable and repeatable data. An SCE test cell was developed using a Cummins 15-liter six-cylinder heavy-duty engine block modified to fire one cylinder (2.5-liter displacement). A Woodward Large Engine Control Module (LECM) is integrated to permit real-time advanced combustion control implementation. Fixed location of 50% burn and Controlled End Gas Auto-Ignition (C-EGAI) were used to define the ignition timing. C-EGAI allows operation with an optimized fraction of end gas auto-ignition combustion. Intake and exhaust characteristics, fuel composition, and exhaust gas recirculated substitution rate (EGR) are fully adjustable. A high-speed data acquisition system acquires in-cylinder, intake, and exhaust pressure for combustion analysis.

Further development includes advanced control methodologies to maintain stable operation and higher dilution tolerance. Controlled end-gas autoignition (C-EGAI) is used as a combustion control strategy to improve efficiency. A Combustion Intensity Metric (CIM) is used for ignition control while operating the engine under C-EGAI.

During the baseline testing of the developed SCE test cell, effective control of intake manifold pressure, exhaust manifold pressure, engine equivalence ratio, speed, torque, jacket water temperature, and oil temperature was demonstrated. The baseline testing shows reliable and consistent results for engine thermal efficiency, indicated mean effective pressure (IMEP), and coefficient of variance of the IMEP over a wide range of operating conditions.

High Brake Thermal Efficiency (BTE) was achieved using improved hardware and a high EGR rate. Due to the correlation of CIM to the fraction of EGAI (f-EGAI), CIM was used as the reference variable to implement C-EGAI. Achieving conditions of C-EGAI allowed for the utilization of high EGR at high IMEP without inducing knock. The operation of the engine under these conditions showed peak brake thermal efficiency above 46% using an EGR ratio of 30%

The work described proves the concept of using new and innovative control algorithms and CFD-optimized combustion chamber designs, allowing ultra-high efficiency and low emissions for NG ICE's heavy-duty on-road applications.

Keywords: Single Cylinder Engine, Heat Release, Heavy-duty, Natural Gas, End Gas Auto-Ignition

ACKNOWLEDGMENTS

The Department of Energy funded the work presented in this document through the Office of Energy Efficiency and Renewable Energy under grant number DE-EE0008331. Fulbright Scholarship “Fulbright Colombia – Pasaporte a la ciencia 2019” supported the author. The author acknowledges the valuable contributions of project partners Cummins Inc. and Woodward Inc.

DEDICATION

This is dedicated to my mom Laudice and my sisters Lisandra, Carolina, and Yamile. You are the example, the force, and the shelter that allowed me to look further, try harder and come back from the darkest moments. This is all yours. And is dedicated to Ramon. You were there all the time, my loyal friend.

LIST OF DEFINITIONS

AHRR - Apparent Heat Release Rate

ATDC - After Top Dead Centre

BD - Burn duration

BTE – Brake thermal efficiency

BMEP – Brake Mean Effective Pressure

BP – Brake Power

BS - Brake-specific

BTDC - Before Top Dead Centre

BTE - Brake Thermal Efficiency

CA - Crank Angle

CAD - Crank Angle Degrees

CA50 - Location 50% Mass Burned Crank Angle

C-EGAI - Controlled End-Gas Auto-Ignition

CIM – Combustion intensity metric

CFR - Cooperative Fuel Research

CFD – Computational Fluid Dynamics

CH₄ – Methane

C₃H₈ - Propane

CO - Carbon Monoxide

COV IMEP – Coefficient of Variance IMEP

COV PP – Coefficient of Variance PP

C-EGAI – Controlled End Gas Autoignition

degATDC – degrees after top dead center

degBTDC - degrees before top dead center

EGR - Exhaust Gas Recirculation

EGT – Exhaust Gas Temperature

EU - Europe

f-EGAI – Fraction End Gas Autoignition

FFT - Fast Fourier Transform

FID - Flame Ionization Detection

FMEP – Friction Mean Effective Pressure

FTIR - Fourier Transforms Infrared

HRRs - Slope of Heat Release Rise Rate

ICE – Internal Combustion Engine

IMAP - Intake Manifold Air Pressure

IMEP - Indicated Mean Effective Pressure

IR - Infrared

KOCA - Knock Occurrence Crank Angle

LECM - Large Engine Control Module

NAHRR – Normalized Apparent Heat Release Rate

NMHC - Non-Methane Hydrocarbons

NMNEHC – non-methane non-ethane hydrocarbons

NOx – Nitrogen Oxides

PP – Peak Pressure inside the cylinder

PRR - Pressure Rise Rate

SI - Spark Ignition

SCE – Single Cylinder Engine

THC - Total Hydrocarbon

TPA – Tree Pressure Analysis

US - United States

VOC - Volatile Organic Compounds

TABLE OF CONTENTS

ABSTRACT.....	ii
ACKNOWLEDGMENTS	iv
DEDICATION.....	v
LIST OF DEFINITIONS	vi
LIST OF TABLES.....	xi
LIST OF FIGURES	xii
Chapter 1 - Introduction.....	1
ICE Concepts.....	5
Performance Metrics.....	5
Knock Quantification	5
EGAI.....	6
Combustion Intensity Metric	7
Research Objectives	8
Chapter 2 - Single Cylinder Research Engine Installation, Commissioning, and Baseline Testing.	
.....	10
SCE Test Cell	10
Engine.....	10
Test cell.....	12
Controls	17
Emissions Measurement	21
Exhaust Gas Recirculated Rate.....	21
Baseline Testing	23

Chapter 3 - Controlled End Gas Auto Ignition	29
Pistons	29
Test Cell Modifications.....	30
Engine Test Procedure	31
Prototype A piston.....	32
Engine Performance	33
Brake Power and Efficiency	33
Combustion Characteristics.....	36
In-Cylinder Pressure, Indicated Mean Effective Pressure, and Heat Release Rate.....	36
Combustion Duration	40
Combustion stability.....	41
Fraction End Gas Auto Ignition f-EGAI	43
Analysis of Best BTE Case	45
Piston B.....	45
Piston C.....	48
Uncertainty analysis	49
Chapter 4 – Exhaust Emissions from high-efficiency NG engine.....	52
Nitrogen Oxides.....	52
Total Hydrocarbons	53
Carbon Monoxide	55
Volatile Organic Compounds	56
Exhaust Gas Temperature.....	57
Chapter 5 – Practical Application of Controlled End-Gas Autoignition	59
Low-cost in-cylinder pressure sensors	59
Effect of fuel composition on engine combustion control	69

GT-Power Modeling	72
X15 6-Cylinder1-D TPA Model.....	73
References	85
Appendix.....	90
Detailed X15 SCE information	90
LECM wiring diagram	100

LIST OF TABLES

Table 1. LECM technical specifications.....	20
Table 2. Prototype pistons CR and Squish ratio.....	30
Table 3: Tested Cummins ISX15 engine operating conditions.....	31
Table 4: NG compositions used during the Cummins ISX15 engine testing.....	31
Table 5. Uncertainty estimated for measured variables.....	49
Table 6. Technical specifications of the in-cylinder pressure sensors tested.....	59
Table 7. Operative conditions for low-cost sensor test.....	63
Table 8. Engine operative conditions for the effect of fuel composition test.....	69
Table 9. Fuel composition of NG and NG+C ₃ H ₈ mix.....	69
Table 10. Fuel blending control trends summary.....	71
Table 11. Experimental operative conditions used for TPA GT-Power model calibration.....	74
Table 12. Turbine characteristics.....	75
Table 13 Compressor characteristics.....	76
Table 14. Cylinder variation of performance metrics.....	78
Table 15. Performance results 6-cylinder simulation.....	80

LIST OF FIGURES

Figure 1. Scenarios for GHG reductions involving demand reductions, efficiency improvements, and the introduction of low-carbon fuel [6]	2
Figure 2. Energy consumption by fuel AEO2022 Reference case. quadrillion British thermal units. Source: https://www.eia.gov/outlooks/aoe/ [4].....	3
Figure 3. Pathway to “Diesel-like” Efficiency and Performance [15].....	4
Figure 4. End gas autoignition on a normalized apparent heat release rate trace.	6
Figure 5. X15 SCE Cummins engine. Deactivated cylinders are #1 to #5; the firing cylinder is #6.	10
Figure 6. Piston comparison X15 SCE. Right, Single Cylinder Engine Spark Ignition baseline piston installed in cylinder #6. Center, Dummy hollow pistons in cylinders #1-5. Right, original diesel X15 piston.....	11
Figure 7. SCE camshaft configuration with rocker arm spacers for cylinders #1-#5.....	11
Figure 8. Left: spark plug with spark plug adapter in place of original diesel injector in cylinder #6. Right: the pressure sensor was installed in cylinder #6 using a machined adapter.	12
Figure 9. Location of high-speed pressure transducers on exhaust and intake manifolds.....	12
Figure 10. Cummins X15 SCE Test Cell.....	13
Figure 11. Oil heating system.	14
Figure 12. Oil heater system installed on the SEC X15 engine.....	15
Figure 13. Fuel blender on SCE.....	16
Figure 14. EGR cart schematic.	17
Figure 15. EGR cart modified for SCE.....	17
Figure 16. X15 SCE LECM schematic.....	18
Figure 17. Woodward’s large engine control module LECM overview.	19
Figure 18. X15 SCE LabVIEW schematic.	21
Figure 19. EGR flow calibration, CO ₂ mass balance vs orifice flow meter measurement.	23
Figure 20. 50% Mass burned crank angle vs. brake power for different EGR rates. Operation conditions: 1200RPM, target IMEP 16 bar.....	24

Figure 21. 50% Mass burned crank angle vs. brake thermal efficiency for different EGR rates. Operation conditions: 1200RPM, IMEP 16 bar.....	24
Figure 22. 50% Mass burned crank angle vs. peak pressure COV and IMEP COV for different EGR rates. Operation conditions 1200RPM, IMEP 16 bar.	25
Figure 23. 50% Mass burned crank angle vs. COV and IMEP COV for different EGR rates. Operation conditions 1200RPM, IMEP 16 bar.....	25
Figure 24. 50% Mass burned crank angle vs. 0-10% Burn Duration. Operation conditions 1200RPM, IMEP 16 bar.	26
Figure 25. 50% Mass burned crank angle vs. 10-90% Mass Burned. Operation conditions 1200RPM, IMEP 16 bar.	26
Figure 26. Combustion Intensity vs Brake Torque and Brake Thermal Efficiency. Operation conditions IMEP 16 bar, EGR 20%.....	26
Figure 27. Efficiency map showing contours of constant BTE with respect to Left: EGR rate [%] and BMEP [bar]; Right: Location 50% Mass Burned [deg ATDC] and Brake Mean Effective Pressure [bar]	27
Figure 28. Effect of EGR rate: Left: Crank Angle Degree After TDC vs. Mean In-Cylinder Pressure Trace [bar]; Right: Crank Angle Degree After TDC vs Normalized Accumulated Heat Release	28
Figure 29. Effect of Ignition Timing, Location 50% Mass Burned (CA50): Left: Crank Angle Degree After TDC vs. Mean In-Cylinder Pressure Trace [bar]; Right: Crank Angle Degree After TDC vs Normalized Accumulated Heat Release.....	28
Figure 30. Top: Prototype A piston. CR 16; Middle: Prototype B piston. CR 13.3:1; Bottom: Prototype C piston. CR 15:1.....	30
Figure 31: Woodward FTI pre-chamber spark plug.	31
Figure 32. Top: Cylinder pressure vs. crank angle for piston A 16:1 CR. Engine operating conditions: 1200 RPM, $\phi = 1$, IMAP1.4 bar, EGR rate 30%, IMT 30°C. Bottom: Piston A as removed from the engine.	32
Figure 33. Location 50% Mass Burned Crank Angle vs. Brake Power for all EGR substitution rates piston B 13.3:1 CR. Engine operating conditions: 1200 RPM, $\phi = 1$, IMAP2.2 bar.	33

Figure 34. Location 50% Mass Burned Crank Angle vs. Brake Thermal Efficiency for all EGR substitution rates piston B 13.3:1 CR. Engine operating conditions: 1200 RPM, $\varphi = 1$, IMAP2.2 bar.	34
Figure 35. Location 50% Mass Burned Crank Angle vs. Indicated Mean Effective Pressure for all EGR substitution rates piston B 13.3:1 CR. Engine operating conditions: 1200 RPM, $\varphi = 1$, IMAP2.2 bar.	34
Figure 36. Location 50% Mass Burned Crank Angle vs. brake power for all EGR substitution rates piston C 15:1 CR. Engine operating conditions: 1200 RPM, $\varphi = 1$, IMAP 1.8 bar.	35
Figure 37. Location 50% Mass Burned Crank Angle vs. Brake Thermal efficiency for all EGR piston C 15:1 CR substitution rates. Engine operating conditions: 1200 RPM, $\varphi = 1$, IMAP 1.8 bar.	36
Figure 38. Location 50% Mass Burned Crank Angle vs. Indicated Mean Effective Pressure for all EGR piston C 15:1 CR substitution rates. Engine operating conditions: 1200 RPM, $\varphi = 1$, IMAP 1.8 bar.	36
Figure 39. Variation of Cylinder Pressure vs. Crank angle for different locations 50% mass burned for 13.3:1 CR piston. Engine operating conditions: 1200 RPM, $\varphi = 1$, EGR substitution rate 30%, IMAP 2.2 bar.	37
Figure 40. Variation of Cylinder Pressure vs. Crank angle for different locations 50% mass burned for 15:1 CR piston. Engine operating conditions: 1200 RPM, $\varphi = 1$, EGR substitution rate 30%, IMAP 1.8 bar.	38
Figure 41. Left: Variation of AHRR vs. Crank angle for different locations 50% mass burned. Right: Normalized AHRR and AIHR vs. Crank angle for multiple locations 50% mass burned. Piston B 13.3:1 CR. Engine operating conditions: 1200 RPM, $\varphi = 1$, EGR rate 30%, IMAP 2.2 bar.	39
Figure 42. Left: Variation of AHRR vs. Crank angle for different locations 50% mass burned. Right: Normalized AHRR and AIHR vs. Crank angle. Piston C 15:1 CR. Engine operating conditions: 1200 RPM, $\varphi = 1$, EGR rate 30%, IMAP 1.8 bar.	40
Figure 43. Brake Thermal Efficiency vs Combustion Duration. Engine Piston B 13.3:1 CR. Engine operating conditions: 1200 RPM, $\varphi = 1$, EGR rate 30%, IMAP 2.2 bar.	41
Figure 44. Brake Thermal Efficiency vs Combustion Duration. Engine piston C 15:1 CR Engine operating conditions: 1200 RPM, $\varphi = 1$, IMAP 1.8 bar.....	41

Figure 45. Location 50% Mass Burned Crank Angle vs Peak Pressure Coefficient of Variance. Top: piston B 13.3:1 CR. Engine operating conditions: 1200 RPM, $\phi = 1$, IMAP 2.2 bar. Bottom: piston C 15:1 CR Engine operating conditions: 1200 RPM, $\phi = 1$, IMAP 1.8 bar	42
Figure 46. Location 50% Mass Burned Crank Angle vs IMEP Coefficient of Variance. Top: piston B 13.3:1 CR. Engine operating conditions: 1200 RPM, $\phi = 1$, IMAP 2.2 bar. Bottom: piston C 15:1 CR Engine operating conditions: 1200 RPM, $\phi = 1$, IMAP 1.8 bar.....	43
Figure 47. Location 50% Mass Burned Crank Angle vs. Fraction End Gas Auto Ignition. Top: piston B 13.3:1 CR. Engine operating conditions: 1200 RPM, $\phi = 1$, IMAP 2.2 bar. Bottom: piston C 15:1 CR Engine operating conditions: 1200 RPM, $\phi = 1$, IMAP 1.8 bar	44
Figure 48. Fraction End Gas Auto Ignition vs. Brake Thermal Efficiency. Top: piston B 13.3:1 CR. Engine operating conditions: 1200 RPM, $\phi = 1$, IMAP 2.2 bar. Bottom: piston C 15:1 CR Engine operating conditions: 1200 RPM, $\phi = 1$, IMAP 1.8 bar	45
Figure 49. Cylinder Pressure vs. Crank Angle (Top), Apparent Heat Release Rate vs. Crank Angle (Middle), and Normalized Apparent Heat Release Rate vs. Crank Angle (bottom) is the best brake thermal efficiency condition achieved. Engine operating conditions: 1200 RPM, $\phi = 1$, EGR rate 30%, IMP 2.3 bar, CA50 6 deg aTDC.....	46
Figure 50. Cycle recorded number vs. Fraction End Gas Auto Ignition. Engine operating conditions: 1200 RPM, $\phi = 1$, EGR rate 30%, IMP 2.3 bar, CA50 6 deg aTDC.	47
Figure 51. Cycle recorded number vs. location for 50% mass burned (up), Combustion duration (down). Engine operating conditions: 1200 RPM, $\phi = 1$, EGR rate 30%, IMP 2.3 bar, CA50 6 deg aTDC.....	47
Figure 52. Cylinder Pressure vs. Crank Angle (Top), Apparent Heat Release Rate vs. Crank Angle (Middle), and Normalized Apparent Heat Release Rate vs Crank Angle (bottom) best brake thermal efficiency conditions achieved. Piston C 15:1 CR. Engine operating conditions: 1200 RPM, $\phi = 1$, EGR rate 30%, IMAP 1.8 bar, CA50 9 deg ATDC.....	48
Figure 53. Location 50% Mass Burned Crank Angle vs. Brake power with error bars for all EGR piston C 15:1 CR substitution rates. Engine operating conditions: 1200 RPM, $\phi = 1$, IMAP 1.8 bar	51
Figure 54 Location 50% Mass Burned Crank Angle vs. Brake Thermal efficiency with error bars for all EGR piston C 15:1 CR substitution rates. Engine operating conditions: 1200 RPM, $\phi = 1$, IMAP 1.8 bar	51

Figure 55. Location 50% Mass Burned Crank Angle vs Brake-specific NOx Emission mission for all EGR rates. Engine operating conditions: 1200 RPM, $\phi = 1$, IMP 2.2 bar, CR 13.3:1.....	52
Figure 56. Location 50% Mass Burned Crank Angle vs Brake-specific NOx Emission mission for all EGR rates. Engine operating conditions: 1200 RPM, $\phi = 1$, IMP 1.8 bar, CR 15:1.....	53
Figure 57. Location 50% Mass Burned Crank Angle vs Brake-specific THC Emission for all EGR rates. Engine operating conditions: 1200 RPM, $\phi = 1$, IMP 2.2 bar, CR 13.3:1.....	53
Figure 58. Location 50% Mass Burned Crank Angle vs Brake-specific THC Emission for all EGR rates. Engine operating conditions: 1200 RPM, $\phi = 1$, IMP 1.8 bar, CR 15:1.....	54
Figure 59. Location 50% Mass Burned Crank Angle vs. Brake-specific Emission of THC, NMHC, and NMNEHC for piston B. Engine operating conditions: EGR 30% 1200 RPM, $\phi = 1$, IMP 2.2 bar, CR 13.3:1.....	54
Figure 60. Location 50% Mass Burned Crank Angle vs. Brake-specific Emission of THC, NMHC and NMNEHC for piston C. Engine operating conditions: EGR 30% 1200 RPM, $\phi = 1$, IMP 1.8 bar, CR 15:1.....	55
Figure 61. Location 50% Mass Burned Crank Angle vs. Brake-specific CO Emission for all EGR rates for piston B. Engine operating conditions: 1200 RPM, $\phi = 1$, IMP 2.2 bar, CR 13.3:1.....	55
Figure 62. Location 50% Mass Burned Crank Angle vs. Brake-specific CO Emission for all EGR rates for piston C. Engine operating conditions: 1200 RPM, $\phi = 1$, IMP 1.8 bar, CR 15:1.....	56
Figure 63. Location 50% Mass Burned Crank Angle vs Brake-specific VOC Emission for all EGR rates. Engine operating conditions: 1200 RPM, $\phi = 1$, IMP 2.2 bar, CR 13.3:1.....	56
Figure 64. Location 50% Mass Burned Crank Angle vs Brake-specific VOC Emission for all EGR rates. Engine operating conditions: 1200 RPM, $\phi = 1$, IMP 1.8 bar, CR 15:1.....	57
Figure 65. Location 50% Mass Burned Crank Angle vs. Exhaust Gas Temperature for all EGR rates. Engine operating conditions: 1200 RPM, $\phi = 1$, IMP 2.2 bar, CR 13.3:1.....	57
Figure 66. Location 50% Mass Burned Crank Angle vs. Exhaust Gas Temperature for all EGR rates. Engine operating conditions: 1200 RPM, $\phi = 1$, IMP 1.8 bar, CR 15:1.....	58
Figure 67 AVL QC34C sensor.	60
Figure 68 IMES CPS-03 sensor.	60
Figure 69 CAT GP-4435682 sensor.	60

Figure 70. Sensors tested and adapters. From left to right: adapter for IMES sensor in original in-cylinder pressure location, adapter IMES sensor in DI location, Adapter CAT sensor on DI location, CAT sensor, IMES sensor amplifier, and sensor body.....	61
Figure 71 Location of AVL in-cylinder pressure sensor and direct injector. Head view from the combustion chamber side. The circle denotes the piston diameter.....	62
Figure 72. X15 SCE head. AVL and direct injector location.....	62
Figure 73. Location 50% Mass Burned Crank Angle [degATDC] vs. IMEP for AVL, CAT, and IMES sensor.....	64
Figure 74 Crank angle vs. Pressure for AVL(top), CAT(middle), and IMES(bottom)sensor.	65
Figure 75. Knock index LECM vs. location 50% mass burned crank angle.	66
Figure 76. Location 50% Mass Burned Crank Angle [degATDC] vs. BTE for AVL, CAT, and IMES sensor.....	67
Figure 77. Location 50% Mass Burned Crank Angle [degATDC] vs COV IMEP for AVL, CAT and IMES sensor.....	68
Figure 78. Location 50% Mass Burned Crank Angle [degATDC] vs. COV peak pressure for AVL, CAT, and IMES sensor.....	68
Figure 79. CIM and Spark timing behavior for the addition of 20% C3H8.	70
Figure 80 GT-Power model for six-cylinder X15 NG engine.	72
Figure 81 Upper: Pressure [bar] vs. Crank angle [deg]. Bottom: Pressure [bar] vs. volume [deg](log scale) for SCE simulation from GT-Power.....	75
Figure 82. Upper: Pressure [bar] vs. Crank angle [deg]; Bottom: Pressure [bar] vs. volume [deg](log scale) for 6-cylinder engine simulation from GT-Power	78
Figure 83. Volumetric efficiency from the 6-cylinder X15 engine simulation with respect to SC simulation and experimental data.	79

Chapter 1 - Introduction.

The continuous energy demand increase in modern society leads to a general concern about the impact of combustion emissions on the environment. Human health has been proven to be affected by these emissions, and this motivates the necessity for diversification of the energy sources seeking less pollutant and sustainable alternatives. By 2050, global energy usage is projected to increase by nearly 50% compared with 2020 figures [1].

Energy usage and carbon dioxide production are strongly related. Carbon dioxide is the dominant greenhouse gas, increasing atmospheric concentration greater than 50% over preindustrial levels. These emissions are part of the drivers of the global warming experienced on the planet, which seems to increase over the following decades. The climate change derive from this global warming has transformed from a theme of discussion in scientific and diplomatic debates to a daily basis explanation of the different behavior of the weather and ecosystems interaction of every human on the earth. Some decades ago, global warming predictions were far more optimistic than the reality that is evident now. A temperature increase of just 1.5 to 2.0 °C can have a profound and irreversible impact on Earth's land, atmosphere, and oceans. This reality underscores the urgency of addressing global warming, emphasizing the invaluable significance of every contribution in the fight against climate change. The Paris Agreement of 2015 [2] showed great success in climate diplomacy as each country involved must contribute to preparing, communicating, and updating their plans to limit and reduce greenhouse emissions (GHG). Politic measures will only work if the technology evolves to levels where the efficiency and pollutants emitted will not be a commercial limitation (the price of the technology), user habits (the people need to be confident and happy to use the technology), and country development relationship. [3].

Here is where the internal combustion engine and its strong relationship with the mobility of almost any human on the planet plays a significant role in the climate change study. The transportation sector is one of the main contributors of greenhouse emissions to the atmosphere due to internal combustion engines fueled with petroleum-based fuels. Diesel fuel is the primary energy source in the heavy-duty transportation sector, increasing to 80% of freight use and 28% of all domestic fuel consumed yearly [4] [1]. These projections make clear that the study and development of current and innovative technologies around ICEs, alternative and cleaner fuels, improved overall

thermal efficiency, ultra-low emissions ICE, non-conventional combustion modes, and improved hybrid powertrains are required to achieve the mitigation of climate change and the health effect associated with pollutants by 2050 [5]. Figure 1 shows the predicted contribution of the transportation sector as a greenhouse gas source, with an expected increase of the share for low-carbon fuels (such as high-efficiency natural gas ICEs) and a remaining 20% contribution from the current high-carbon energy sources.

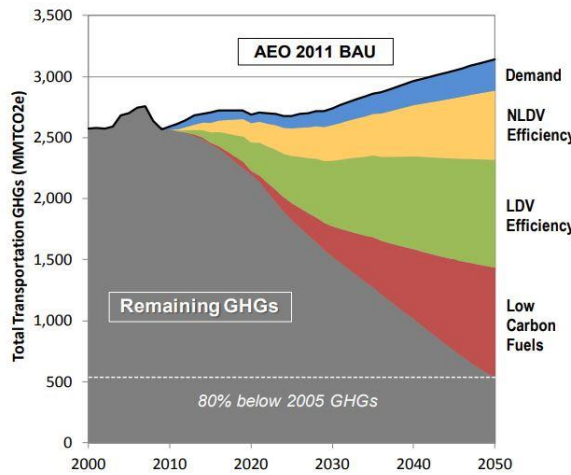


Figure 1. Scenarios for GHG reductions involving demand reductions, efficiency improvements, and the introduction of low-carbon fuel [6]

Electrification faces a more considerable challenge in heavy-duty transportation due to the high energy density, ease of transport, storage, and handling of conventional fuels for ICEs. Meanwhile, petroleum-based fuels are affected by decreasing crude oil reserves and the uncertain political scenarios that affect the final price of the fuel. Given the availability of Natural Gas (NG) within the US with the implementation of hydraulic fracking techniques, natural gas appears as a natural alternative for short-term substitution in traditional CI diesel engines (Figure 2). NG is lower in cost, produces no particulate matter, and lowers CO₂ emissions due to a lower carbon-to-hydrogen ratio inherent to fuel composition, mainly methane (CH₄), the cleanest burning of all hydrocarbons (HC). These conditions also represent a lower cost in after-treatment systems to meet emission regulations that define lower operative costs for the end user [7] [8]. [9].

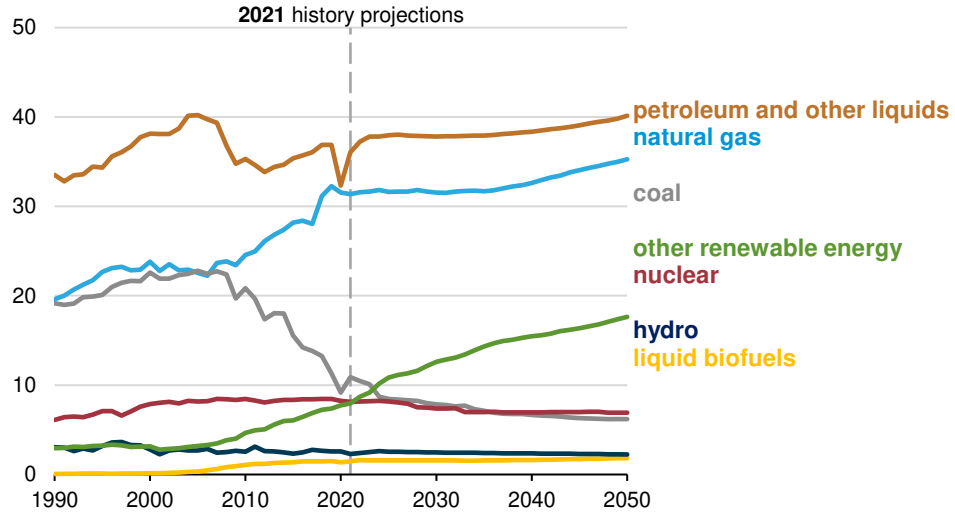


Figure 2. Energy consumption by fuel AEO2022 Reference case. quadrillion British thermal units. Source:
<https://www.eia.gov/outlooks/aoe/> [4]

The use of diesel fuel and compression ignition engines is motivated mainly by the lower operating cost, higher fuel efficiency, and higher durability than equivalent spark-ignited engines [10]. To increase their share in the medium and heavy-duty transportation sector, NG ICEs must increase Brake Thermal Efficiency (BTE). To achieve this level of BTE, the combustion control of Spark Ignited (SI) homogeneous NG-Air mixtures must be improved to allow high compression ratios (CR), boost pressures, and high Exhaust Gas Recirculation (EGR) levels. Knock is one of the main limitations of spark ignition engines during high-power operating conditions or misfires during diluted operating conditions [11] [12]. Figure 3 shows the proposed steps to achieve “diesel-like” efficiencies with spark-ignited NG-fuelled engines. EGR dilution, enhanced burn rate, and advanced control are among some of the required developments to be explored. Another requirement is to improve the capability to operate on variable reactivity fuel. Wide regional variances of fuel reactivity make high-performance engines challenging to optimize for the US market [13]. Methane Number (MN), the metric used to quantify the reactivity of NG, is not standardized, as is the Octane Number of gasoline fuels. Natural gas MN varies from 68 to 96 on the US market [14].

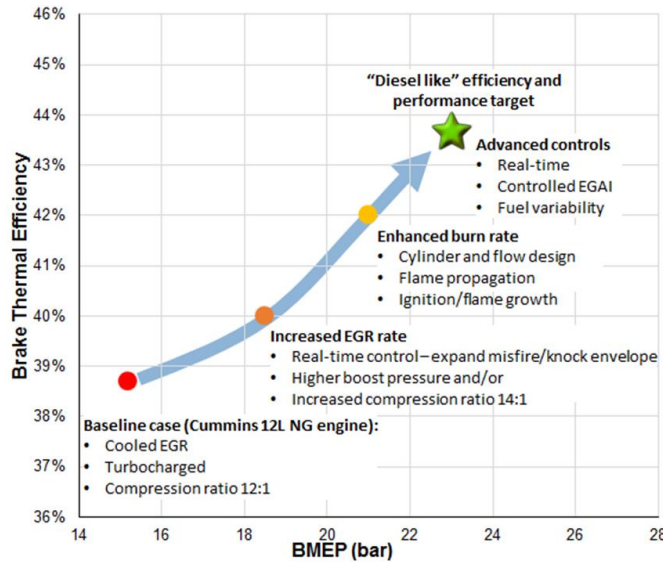


Figure 3. Pathway to “Diesel-like” Efficiency and Performance [15].

Another essential aspect is transitioning from laboratory testing to real-world implementation of innovative techniques. In-cylinder pressure measurement system for cycle-to-cycle feedback combustion control has proven to be the way to improve efficiency and reduce the pollutants of internal combustion engines. The development of more robust engine management modules allows for analysis and control of the combustion process cycle-to-cycle with the capability to sustain ultra-high efficiency levels with variable external conditions such as fuel quality, environmental conditions, or load demand.

One of the problems of this combustion control technique is the necessity to use piezoelectric dynamic pressure sensors, which are accurate but expensive, require additional signal conditioners, and have limited durability under harsh conditions [16]. Low-cost pressure sensors should be the way to go for combustion control, and commercial alternatives have proven to reach a high accuracy level with good applicability in actual conditions operations. Manufacturers such as Caterpillar Inc. use this type of sensor. New products have been tested [15], showing that with the correct signal processing, the desired cycle-to-cycle feedback can achieve optimal combustion phasing [17]. The research objective is to find the percentage of efficiency that can be lowered by using low-cost sensors against the reference laboratory-grade pressure sensors. Acceptable margins will guarantee the applicability of techniques such as C-EGAI on commercial ICE engines.

ICE Concepts.

Performance Metrics

Brake power is calculated from the IMEP obtained from the in-cylinder pressure readings. Then is adjusted with the friction mean indicated pressure (FMEIP) to get BMEP, which then is used the estimate the Brake Power (BP) (Eq. 1). Then the BTE is estimated with the Coriolis flow measurement of the fuel (Eq. 2.).

$$BP = \frac{(IMEP - FMEP)V_dN}{n_R} \quad (1)$$

$$BTE = \frac{BP}{\dot{m}_f LHV} \quad (2)$$

Where:

- \dot{m}_f = Fuel mass flow rate
- LHV = Fuel lower heating value
- V_d = Displacement volume
- N = Engine rotational speed

Knock Quantification

Knock is quantified by the LECM using the knock ripple sum technique in the CIM. A LabVIEW-based algorithm also quantifies knock separately. This system uses the sampling frequency and the natural frequency of the engine to apply a bandpass filter to the pressure data to calculate the high frequencies of pressure oscillations caused by EGAI. A fast Fourier transform (FFT) is used to this band-pass filtered data to obtain the power of the spectrum of the signal.

A time-averaged approach is then used to establish a knock index and to provide an objective and repeatable metric for comparison of the overall intensity of knock experienced with operating conditions. Knock integral refers to the area under the curve bounded by FFT power spectrum magnitude over a set number of combustion cycles. It is recognized that the angle formed by the FFT amplitude is not a continuous function; nevertheless, since a discreet value for amplitude is known for every cycle, Eq. 3 gives the area under the curve.

The knock integral is derived by summing the FFT power spectrum amplitudes (in kPa²) [18] [19].

$$KI = \text{Area}_{\text{Bounded}} = \sum_{i=0}^n \frac{\{KL(i+1) + KL(i)\}}{2} \quad (3)$$

Where:

n = number of combustion cycles in a data set

$KL(x)$ = knock level magnitude for a given combustion cycle, x .

EGAI

The normalized Apparent Heat Release Rate (AHRR) curve of the pressure trace data from the engine is used to define the presence of EGAI. The fractional EGAI (f-EGAI) metric is used considering the fraction of the total energy released that participated in the EGAI event. This metric was developed by Zdanowicz et al. [12, 13] and is calculated according to Equation 4 [20]. The onset location (or crank angle) of the EGAI is determined by searching for the presence and location of inflection points over the AHRR trace (Figure 4). Knowing the EGAI onset is crucial as it defines where normal combustion ends and where EGAI combustion initiates. With this, it is possible to calculate f-EGAI.

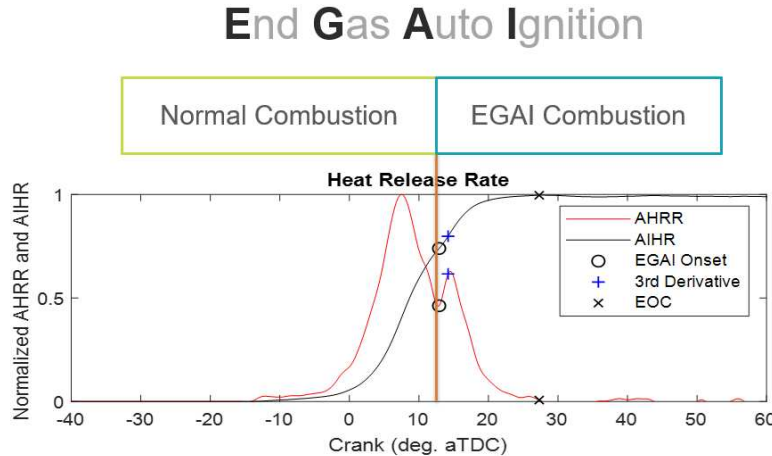


Figure 4. End gas autoignition on a normalized apparent heat release rate trace.

A detailed explanation of the algorithm to estimate the EGAI, Onset EGAI, and f-EGAI can be found in Bestel et al. [20].

$$f_{EGAI} = \frac{\left[\int \frac{dQ}{dt} \right]_{EGAI}}{\left[\int \frac{dQ}{dt} \right]_{Total}} \quad (4)$$

The AHRR is calculated from the pressure data for each cycle recorded, based on the first law single zone model using Equation (5)

$$\frac{dQ}{d\theta} = \frac{\gamma}{\gamma-1} P \frac{dV}{d\theta} + \frac{1}{\gamma-1} V \frac{dP}{d\theta} \quad (5)$$

Where:

P = in-cylinder pressure

Q = heat release

V = cylinder volume

γ = ratio of specific heats

Combustion Intensity Metric

The LECM controlled the ignition timing with a target CA50 (Location of 50% mass burned in °ATDC). CA50 is modified from late to early values until the knock threshold is found. Then the EGR rate is adjusted, and a new CA50 sweep is performed. Once the knock limits are found, the engine can be operated with Combustion Intensity Metric (CIM) as a variable for the ignition control.

CIM is defined as [18] in Equation 6:

$$CIM = A_1 \left(\frac{P_{max}}{P_{max_{ref}}} \right) + A_2 \left(\frac{BD}{BD_{ref}} \right) + A_3 \left(\frac{PRR}{PRR_{ref}} \right) + A_4 \left(\frac{HRRS}{HRRS_{ref}} \right) + A_5 \left(\frac{KI}{KI_{ref}} \right) \quad (6)$$

where A_1 through A_5 are calibration constants.

CIM is a Woodward-developed metric that integrates several combustion parameters to characterize combustion. Engine control using CIM permits engine operation with some level of

EGAI, achieving higher BTE without compromising engine reliability [21]. The parameters used to compute CIM are:

- P_max = Magnitude of Peak Pressure (bar)
- BD = Burn duration (CA)
- PRR = Pressure Rise Rate (bar/deg)
- HRRs = Slope of Heat Release Rise Rate (J/deg/deg)
- KI = Knock Intensity (Knock Ripple Sum)

The CIM is also used to define a Knock Threshold for the engine. This allows the continuous operation of the engine under safe conditions while allowing a safe amount of knock. This metric relates the engine limit parameters for each term involved in CIM calculation. Then a percentage of this maximum CIM value would be considered the limit acceptable range of the knock threshold. For this engine, the knock threshold selected is 40% of the max CIM, with calibration values for this metric P_max 200 bar, BD 7 deg CA, PRR 16 bar/deg, and HRRs -0.5 J/deg/deg.

Research Objectives

Main Goal

This research addresses fundamental limitations to achieving diesel-like efficiencies in heavy-duty on-road NG engines. The benchmark is the Cummins 15-liter Diesel heavy-duty engine platform, which has a baseline BTE of 44% at peak torque.

Research Objectives

The following key project objectives are identified:

1. Evaluate whether a natural gas engine can operate at the same or higher efficiency than the same size diesel engine.
2. Determine whether a spark-ignited natural gas engine can be operated with consistent, significant end gas autoignition.
3. Assess the ability of advanced controls with real-time combustion pressure feedback to maintain efficient, safe operation as fuel composition is varied.

4. Compare various low-cost combustion pressure sensors and determine whether they can be used for real-time combustion feedback for advanced control.
5. Evaluate whether the operating conditions required for the natural gas engine to meet diesel engine efficiency are practical and can be implemented in a commercial engine.

Major Tasks

The primary tasks for accomplishing research objectives are:

- Develop a Single Cylinder Research engine using a 15-liter ISX15 Cummins diesel engine converted into a 2.5-liter single-cylinder.
- Characterize end-gas autoignition (EGAI) phenomena for NG/air/EGR mixtures of varying reactivity using an SCE research test cell.
- Provide baseline data to Validate/refine tools for cylinder three-dimensional computational fluid dynamics (CONVERGE) modeling and cycle simulation (GT-Power).
- Develop advanced real-time control algorithms to facilitate the expansion of EGR, knock, and misfire limits, tolerance and adaptation to variable fuel reactivity (methane index from 65 to 90), and controlled end-gas autoignition (C-EGAI).
- Test improved hardware design over a wide range of load and EGR substitution rates to identify the most efficient conditions and achieve C-EGAI.
- Evaluate the effectiveness of low-cost pressure transducers on real-time control algorithms to operate the SCE under the most efficient previously identified conditions.
- Analyze the effect of fuel composition variability on the engine performance while operating under high-efficiency conditions.
- Develop the existing GT-Power SCE model to a full-scale 6-cylinder engine, evaluating the operating conditions found on the SCE test to achieve high BTE.
- Use the GT-Power 6-cylinder engine model to evaluate the requirements of crucial engine components like turbochargers and EGR valves concerning the SCE test results.

Chapter 2 - Single Cylinder Research Engine Installation, Commissioning, and Baseline Testing.

SCE Test Cell

Engine

A solid model of the current production ISX15 (15-liter) diesel engine converted into a 2.5-liter single-cylinder engine is shown in Figure 5. The inline, 6-cylinder X15 engine has bore and stroke dimensions of 137 x 169 mm and a total displacement of 15 liters. Hence, the displacement of the firing cylinder is 2.5 liters. The engine was designed to allow operation up to 25 bar indicated mean effective pressure (IMEP).

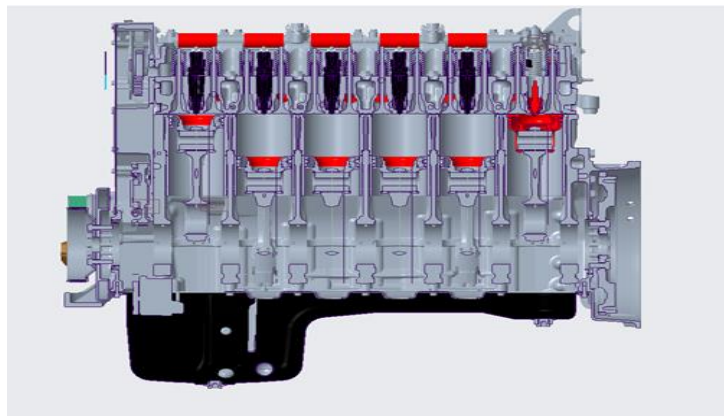


Figure 5. X15 SCE Cummins engine. Deactivated cylinders are #1 to #5; the firing cylinder is #6.

While the crankshaft and connecting rods are standard X15 parts, cylinders one to five are deactivated by replacing the pistons with “dummy pistons” machined with a hole in the middle to reduce/eliminate compression but to match the mass of the #6 piston to maintain the balance of the crankshaft (see Figure 6). Cylinder #6 (firing cylinder) has new components developed for this application: piston, ring set, cylinder liner, connecting rod, and bearings. This #6 piston has a specific Cummins proprietary design for the intended spark ignition operation with a compression ratio of 11.5:1 (Figure 6). This piston was used for the commissioning and baseline testing in conjunction with a Bosch MR3DII360 spark plug.



Figure 6. Piston comparison X15 SCE. Right, Single Cylinder Engine Spark Ignition baseline piston installed in cylinder #6. Center, Dummy hollow pistons in cylinders #1-5. Right, original diesel X15 piston.

Spacers were added in place of the original rocker arms to deactivate cylinders #1-#5 to maintain oil pressure and ideal lubrication conditions. (Figure 7). The head was machined for the #6 cylinder to accept a sparkplug adaptor in place of the original diesel injector. The cylinder head was also machined to install a cylinder pressure transducer (AVL QC34C), shown in Figure 8. This transducer uses a machined adapter, so alternative transducer models may be tested in the future, as installation dimensions are consistent across transducer suppliers.

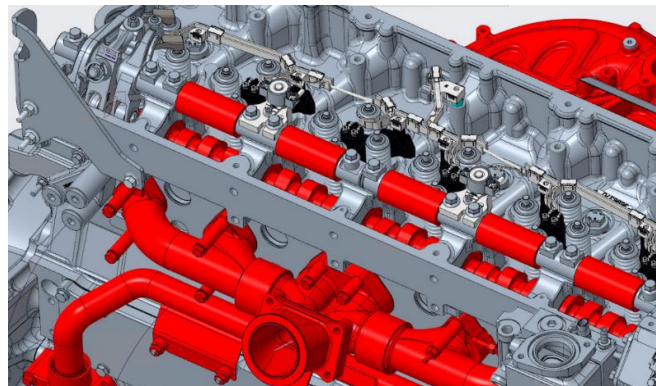


Figure 7. SCE camshaft configuration with rocker arm spacers for cylinders #1-#5.

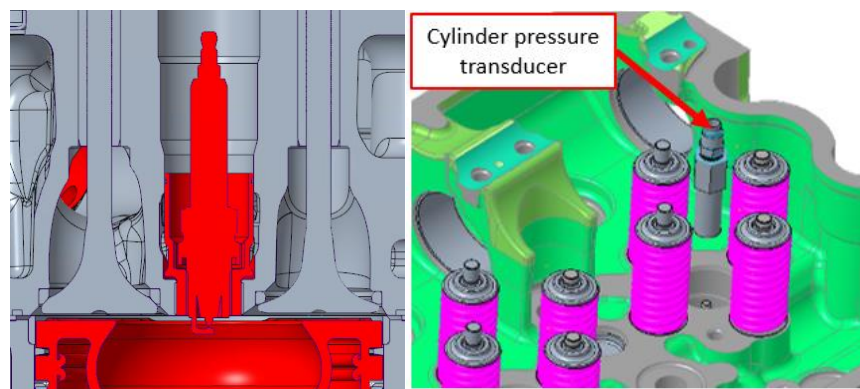


Figure 8. Left: spark plug with spark plug adapter in place of original diesel injector in cylinder #6. Right: the pressure sensor was installed in cylinder #6 using a machined adapter.

The intake and exhaust manifolds were machined to accommodate high-speed Kistler piezo resistive intake (Type 4007D) and water-cooled exhaust (Type 4049B) pressure transducers (Figure 9). These sensors allow for more accurate model validation and tuning of the engine's 3-D Converge CFD and 1-D GT-Power models.

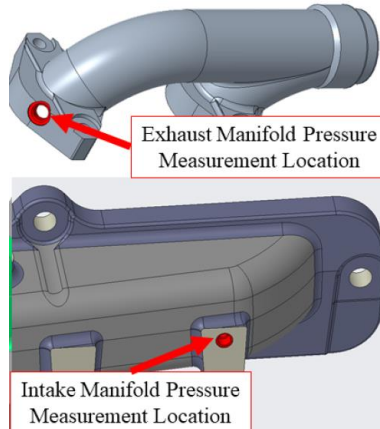


Figure 9. Location of high-speed pressure transducers on exhaust and intake manifolds.

In addition to the internal engine modifications previously noted, the following parts were also removed from the original X15 diesel engine:

- Diesel fuel pump, filter, supply lines, high-pressure rail system
- ECU (Engine Control Unit)
- EGR (Exhaust Gas Recirculation) valve and cooler
- EGR crossover
- Turbocharger and related parts
- Engine starter.

Test cell

The Cummins X15 SCE test cell is shown in Figure 10. The test cell uses an AC electric motor/generator with a regenerative variable frequency drive (VFD) to spin the engine for motored-mode operation and startup and to apply the load. The VFD allows a desired speed to be

set and controls the engine's load to keep the targeted speed constant or drive the engine if there is no combustion.

The engine is mounted in a specially modified test cell. A steel chassis supports the engine with custom-made engine mounts aligning the engine and the motor. Two control panels are located at the sides of the engine, and water and air lines run from the facility coolant and compressed air supply systems, respectively.

The engine has its OEM flywheel and uses an adapter plate to connect to the driveshaft. A custom-designed torque tube connects to the electric motor on the other side of the driveshaft. The torque tube is a machined hollow aluminum tube with a specific internal and external diameter to deform in a pre-calculated amount while the load is applied. This deformation is measured with strain gauges that feed the signal to the data acquisition system to know the actual torque from the engine.

Cylinder pressure, intake manifold pressure (IMP), and exhaust manifold pressure (EMP) are crank angles synchronized with high-resolution, high-fidelity boundary conditions for combustion analysis. An encoder is connected to the crankshaft, trigger for the data sampling, with 3600 pulses per encoder revolution (7200 per cycle). This encoder is supported in place with a special plate that uses the engine mount as a support and an upper brace to prevent vibrations or deformations that could affect the encoder signal.



Figure 10. Cummins X15 SCE Test Cell.

The cooling system for the engine is connected to an external water cooling/heating system that allows control of the coolant temperature. This heat exchanger uses water from the facility to extract heat from the engine. A control valve increases or decreases the cooling water flow as a function of the engine load to maintain optimal engine temperature (85°C)

The engine's air intake uses compressed dry air from the facility's air supply. The intake pressure could be varied up to 60 psi. A Woodward Venturi effect fuel mixer allows the addition of gaseous fuel to the air supply. The air-fuel mixture passes through an intake heater system to simulate the heating from compression from the turbocharging process in a real engine. Next, exhaust gases are introduced from the EGR cart. Finally, a Woodward throttle valve, controlled through the LabVIEW system, regulates the air-fuel mixture in the engine.

The custom-made exhaust system allows for emissions, temperature, and pressure sampling. This system also includes an exhaust backpressure valve (Woodward GloTech) to simulate the effects of the turbocharger exhaust turbine in a real engine. A port feeds the EGR cart with exhaust gases to be conditioned and recirculated to the intake system. A BOSCH UEGO 4.9 sensor was installed in the exhaust after the back-pressure valve. This sensor provides feedback for the LECM combustion control through the air/fuel ratio.

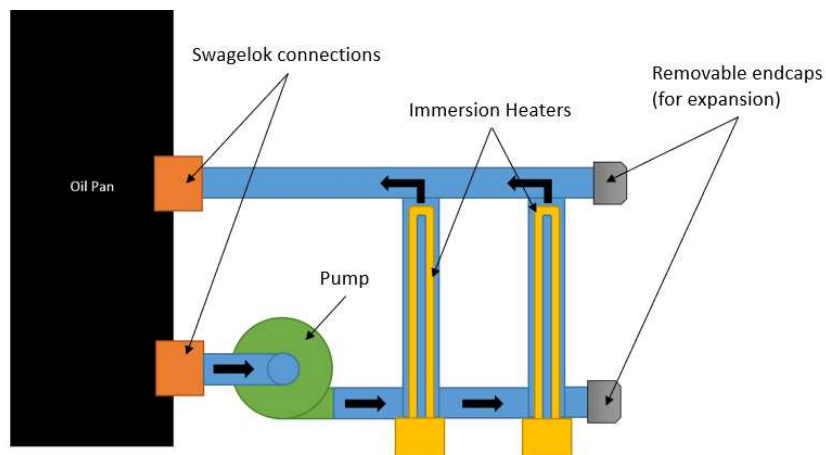


Figure 11. Oil heating system.

A special oil heating system was developed to allow the engine to operate within the design limits for oil temperature while the engine is running with just one cylinder firing (Figure 11). This system

takes oil from the oil pan with a 1kW pump and feeds a 6kW heater array before returning the oil to the engine sump. The nominal oil temperature for this engine is 105°C. The engine kept the original oil thermostat to keep a constant temperature as different loads were applied. The oil heater system will shut off if the load conditions on the engine provide enough heat to maintain the oil temperature at the set point.



Figure 12. Oil heater system installed on the SEC X15 engine.

Fuel system

A Fuel blender system that allows the mixture of up to 3 different gases was designed and installed on the test cell (Figure 13). This system can measure and control each gas's mass flow in real time and provide the total fuel flow headed to the intake, obtaining the desired air/fuel ratio. This blender uses two Alicat flow meters (MCR-500SLPM-D) to control the supplementary gases (mainly methane and propane for this research), and an orifice flow meter is used to measure the natural gas flow. A dedicated valve controls the natural gas flow going to the blender. After the gases are mixed in the blender, the main fuel line feeds the intake. A LECM-controlled safety Woodward MPLO medium pressure lock-off valve and an Omega PV14-B proportional valve control the total fuel mass flow.



Figure 13. Fuel blender on SCE

As used in the fuel line, a Flow meter based on The American Gas Association (AGR) Report #3 standard [22] for orifice flow meters is used to measure the air mass flow. Each application was calculated in this case, and custom orifice plates were fabricated according to the expected flow, temperature, and gas type. Ashcroft GC52 differential pressure sensors and A2SA absolute pressure sensors are used with K thermocouples to estimate the respective gas flow. For detailed fuel flow measurement, a Bronkhorst M15 Coriolis flowmeter gives assurance that the fuel flow measurement is correct [23].

EGR Cart.

An exhaust gas recirculation test cart was developed to be able to provide variable and conditioned EGR flows to be able to simulate different EGR configurations. Built initially to conduct tests on the CFR engine [9], the cart was modified with increased flow and heat management capacity to suit the requirements of the X15 SCE. Exhaust gases from a port on the manifold's high-pressure side enter the EGR cart through a hose. Air and water heat exchangers reduce the gas temperature from 100-150°C, the user defines the desired temperature, and the coolant flow is adjusted by a LabView-controlled valve (Honeywell / ML7425A3013).

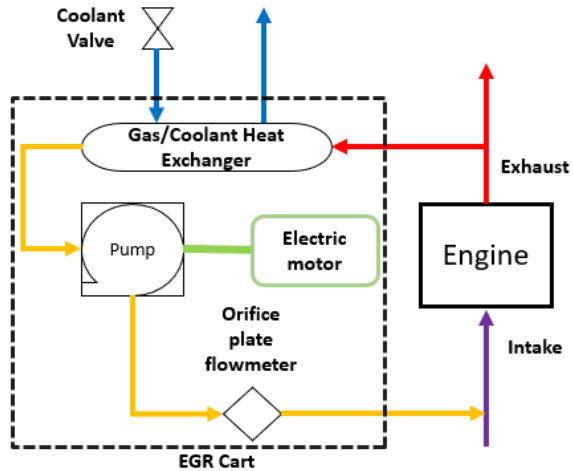


Figure 14. EGR cart schematic.



Figure 15. EGR cart modified for SCE.

Controls

The engine and test cell are controlled through two main modules, Woodward's Large Engine Control Module (LECM) and a National Instruments (NI PXI 1050 chassis with 6224 and 6704 modules) data acquisition and control module. The LECM is a control unit designed to operate reciprocating engines (gas, diesel, or dual fuel) used in power generation, marine propulsion, locomotive and industrial engines, and process markets. This system uses a single-box approach

that can be built up with interlocking modules into a single engine-mountable assembly. This control scheme uses a modular approach for electronic control modules and software. Each module has its microprocessor and runs its software routines, written in Woodward's MotoHawk software, using proven core functions and algorithms. The modules share their information in real-time, making the system act as one fully integrated controller. The test cell was configured for this application with an electronic ignition driver module (EID), an auxiliary module for in-cylinder pressure analysis and knock detection, and a central module for fuel management. Figure 16 presents the general schematic for LECM control tasks. Fuel flow (equivalence ratio) and ignition timing (combustion phasing) are this application's two LECM control duties.

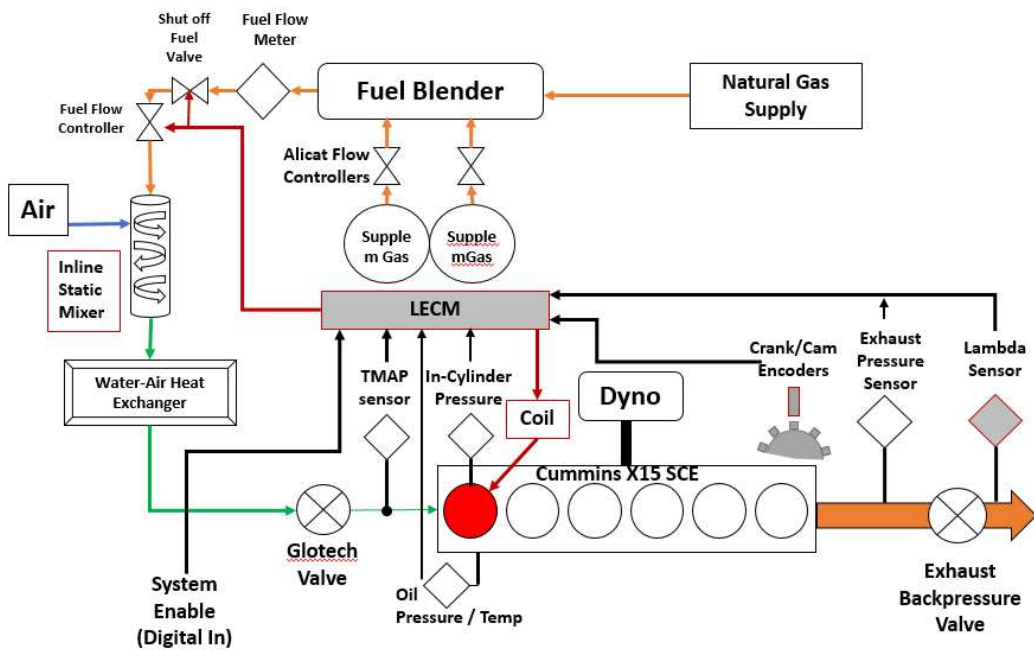


Figure 16. X15 SCE LECM schematic.

The LECM was selected because Woodward has developed efficient and comprehensive cycle-resolved combustion diagnostics using high-efficiency intelligent algorithms. Each cycle, including heat release and mass fraction burn calculations, is analyzed in real-time. This technology, called Real-Time Combustion Diagnostics and Control (RT-CDC), can be viewed as a Smart Sensor, where key combustion metrics such as IMEP, peak pressure location and magnitude, burn duration (10-90%), location of 50% burn duration (CA50), and misfire can be calculated in the time of one engine cycle and put onto the data bus for use by the LECM.

The LECM (Figure 17) is configured with an electronic ignition driver module (EID) and auxiliary module for real-time in-cylinder pressure analysis of combustion metrics, including heat release, mass fraction burn, IMEP, combustion duration, knock intensity quantified by the knock ripple sum method [18]. The sampling resolution of the LECM is 0.5 °CA in the combustion section of the cycle (-60 to 60 °ATDC). This capability allows the system to monitor the pressure trace and heat release and estimate the Combustion Intensity Metric (CIM), which correlates to the end-gas autoignition (f-EGAI) fraction. Achieving stable engine operation under EGAI conditions is known as C-EGAI, where the constant f-EGAI for each cycle is modulated by primary parameters such as spark timing, fuel, and EGR rate [24].

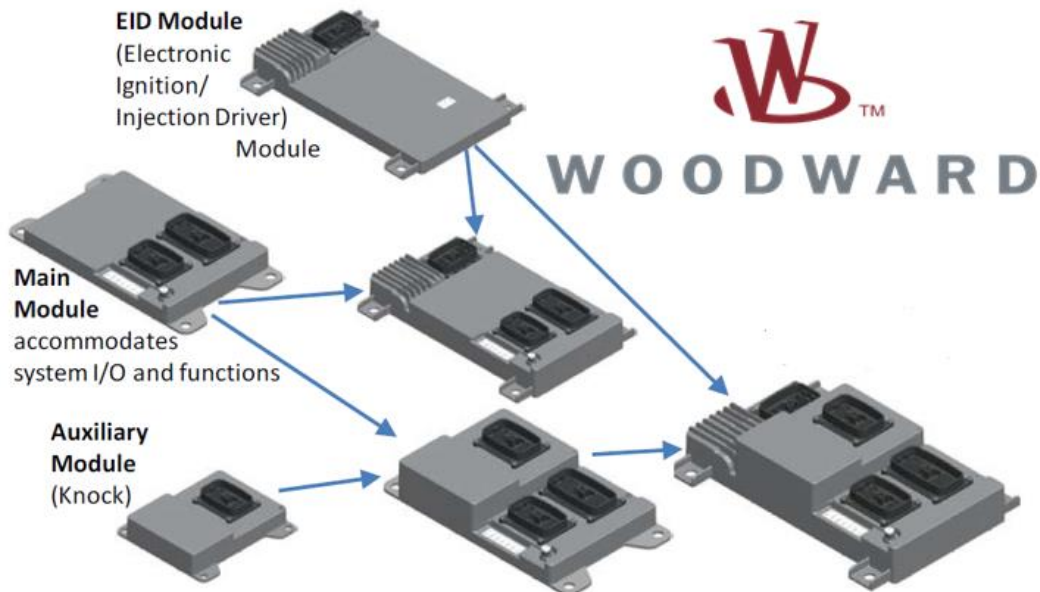


Figure 17. Woodward's large engine control module LECM overview. Adapted from [25]

The RT-CDC system can monitor the pressure trace and heat release, generate the crank angle at which EGAI occurs, and calculate the fraction of end-gas autoignition (f-EGAI, defined earlier). Then C-EGAI is employed to maintain constant f-EGAI for each cycle by modulation of primary parameters such as spark timing, fueling, and EGR rate. As engine operation, fuel quality, and ambient conditions change, the LECM can adapt at least one parameter, such as spark timing to maintain a target f-EGAI overall engine operating conditions.

A summary of the LECM technical specifications is presented in Table 1

Table 1. LECM technical specifications.

Module	Inputs	Outputs
Main	<ul style="list-style-type: none"> • 16 digital • 29 single-ended analog • 8 differential analog • 8 T/C or RTD • 2 wide-band oxygen sensor • 4 VR/HE/PWM speed sensors 	<ul style="list-style-type: none"> • 8 HS digital • 12 LS/PWM digital • 2 analog • 4 HS/LS/TP/PWM digital <p>Communications:</p> <ul style="list-style-type: none"> • 3 CAN / 1 Ethernet
EID	<ul style="list-style-type: none"> • 2 VR/HE/PWM speed sensors • 1 additional Hall Effect/PWM speed sensor • 2 digital jumpers 	<ul style="list-style-type: none"> 1 HS digital • 20 electronic ignition/injection drivers <p>Communications:</p> <ul style="list-style-type: none"> • 2 CAN
Aux	<ul style="list-style-type: none"> • 24 knock, pressure, or T/C • 2 VR/HE/PWM speed sensors • 2 digital jumpers 	<ul style="list-style-type: none"> • 2 HS digital • 2 analog <p>Communications:</p> <ul style="list-style-type: none"> • 1 CAN

The National Instruments-based system uses a LabVIEW custom-made virtual instrument to control the throttle, air intake pressure, and temperature, exhaust back pressure, EGR rate, and dynamometer. In Figure 18, the black lines show which sensors feed the control modules, which control the actuators (red lines). This system utilizes low-speed sampling and controls and monitors overall test cell parameters, including temperatures, pressures, and flows, with a sample rate of 2 Hz.

The additional high-speed sampling for the in-cylinder pressure and dynamic intake and exhaust sensors uses National Instruments based high-speed system (NI PXIe 1071 chassis with NI PIXe 6363 module) running an in-house developed combustion logger virtual instrument in LabVIEW. This system allows for a 0.1 deg sampling rate (3600 samples per revolution). Performance metrics based on combustion pressure data include IMEP, Peak Pressure coefficient of variation (COV), IMEP COV, CA50, Start of Combustion, Heat Release, and Knock Index.

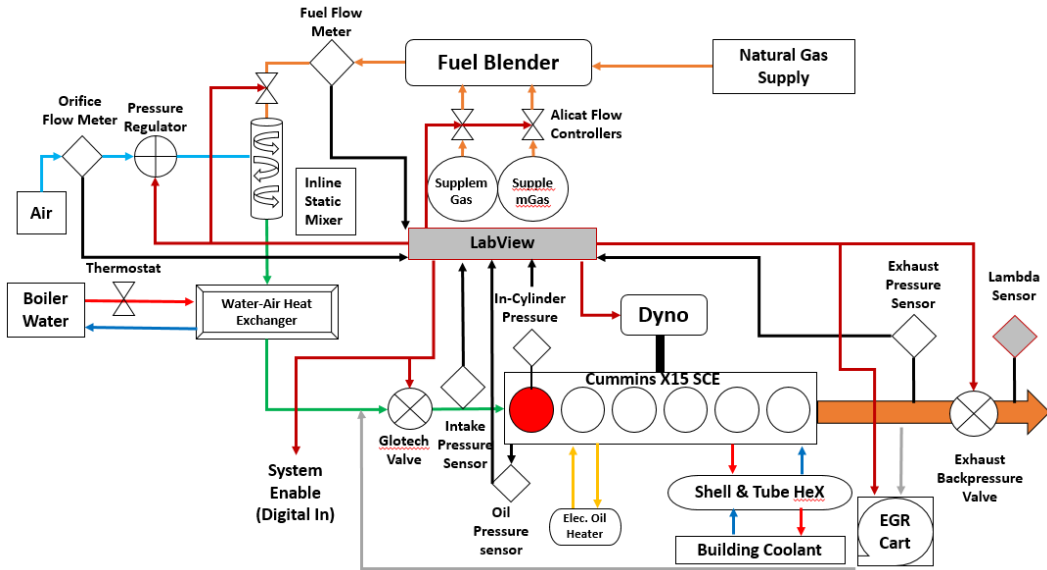


Figure 18. X15 SCE LabVIEW schematic.

Emissions Measurement

The exhaust manifold has an emission sampling port and a heated sample line. Exhaust gas concentration measurements for CO, CO₂, NO_x, O₂, and THC are measured with a Siemens 600 series 5-gas Analyzer system (Ultramat, Noxmat, Oxymat, and Fidamat, respectively) and formaldehyde, speciated hydrocarbons up to C₃, NO, and NO₂ are quantified with an MKS Multigas 2030 FTIR spectrometer. Fuel composition (CH₄, C₂H₆, C₃H₈, i-C₄H₁₀, n-C₄H₁₀, i-C₅H₁₂, n-C₅H₁₂, n-C₆H₁₄, N₂, CO₂) is analyzed during engine operation with a Varian CP-4900 MicroGC.

Exhaust Gas Recirculated Rate

The exhaust gas recirculation rate was a critical aspect of this research, as it is part of the strategies to increase the BTE due to running at higher IMEP. Recirculated exhaust gas flow measurement must be accurate to be a helpful tool. To achieve the required accuracy, a CO₂ concentration analysis was performed, using the concentration of CO₂ in the intake air, fuel, and recirculated exhaust gases, to find the mass flow of EGR and then the equivalent EGR rate. Air mass flow is quantified from the Coriolis fuel flow measurement, and the Air/Fuel ratio is measured with a lambda sensor. The molar concentrations of CO₂ in each flow were measured with the 5-gas

analyzer. This EGR flow quantification allowed calibration of the orifice plate measurement device on the EGR cart to simplify the measurement process during testing. The calibration data is presented in Figure 19. EGR rate quantification requires gas composition measurement of the exhaust gases and the intake mixture of gases on the intake (Air + Fuel + EGR). Fuel composition is obtained from the GC fuel analyzer. Composition measurement for each mix determines the molar mass, knowing the pressure and temperature conditions of the fuel line at the GC sampling port, intake, and exhaust manifolds, respectively [26].

The rate of EGR is

$$EGR = \frac{\dot{m}_{EGR}}{\dot{m}_{mix}} = \frac{\dot{m}_{EGR}}{\dot{m}_{EGR} + \dot{m}_{air} + \dot{m}_{fuel}} = \frac{1}{1 + \frac{\dot{m}_{fuel}}{\dot{m}_{EGR}} + \frac{\dot{m}_{air}}{\dot{m}_{EGR}}} = \frac{1}{1 + \frac{1}{\dot{m}_{EGR}} * (\dot{m}_{air} + \dot{m}_{fuel})} \quad (7)$$

Where \dot{m}_{mix} Represents the mass balance of the intake mixture of gases. A mass balance determines the mass flow of CO₂ for each intake mixture component:

$$\dot{m}_{CO2_{mix}} = \dot{m}_{CO2_{EGR}} + \dot{m}_{CO2_{air}} + \dot{m}_{CO2_{fuel}} \quad (8)$$

As there is no reaction for the CO₂:

$$\dot{N}_{CO2_{mix}} = \dot{N}_{CO2_{EGR}} + \dot{N}_{CO2_{air}} + \dot{N}_{CO2_{fuel}} \quad (9)$$

The CO₂ molar fraction on the mix is:

$$Y_{CO2,mix} = \frac{\dot{N}_{CO2_{EGR}} + \dot{N}_{CO2_{air}} + \dot{N}_{CO2_{fuel}}}{\dot{N}_{CO2_{mix}}} = \frac{\dot{N}_{CO2_{EGR}} + \dot{N}_{CO2_{air}} + \dot{N}_{CO2_{fuel}}}{\dot{N}_{air} + \dot{N}_{fuel} + \dot{N}_{EGR}} \quad (10)$$

Knowing that $Y_{CO2} = \frac{\dot{N}_{CO2}}{\dot{N}}$ and $\dot{m} = \dot{N} * M$,

$$Y_{CO2,mix} = \frac{Y_{CO2,EGR} * \dot{N}_{EGR} + Y_{CO2,air} * \dot{N}_{air} + Y_{CO2,fuel} * \dot{N}_{fuel}}{\dot{N}_{CO2,mix}}$$

$$\frac{\frac{Y_{CO2,EGR} * \dot{m}_{EGR}}{M_{EGR}} + \frac{Y_{CO2,air} * \dot{m}_{air}}{M_{air}} + \frac{Y_{CO2,fuel} * \dot{m}_{fuel}}{M_{fuel}}}{\frac{\dot{m}_{mix}}{M_{mix}}}$$

$$\frac{\frac{Y_{CO_2fuel} * \dot{m}_{EGR}}{M_{EGR}} + \frac{Y_{CO_2air} * \dot{m}_{air}}{M_{air}} + \frac{Y_{CO_2fuel} * \dot{m}_{fuel}}{M_{fuel}}}{\frac{\dot{m}_{CO_2EGR} + \dot{m}_{CO_2air} + \dot{m}_{CO_2fuel}}{M_{mix}}} \quad (11)$$

Equations 7 and 11 contain two unknowns, EGR and \dot{m}_{EGR} . Solving for \dot{m}_{EGR} In equation 7 and substituting on equation 1:

$$\dot{m}_{egr} = \frac{\frac{Y_{CO_2fuel} * \dot{m}_{fuel}}{M_{fuel}} + \frac{Y_{CO_2air} * \dot{m}_{air}}{M_{air}} - \frac{Y_{CO_2mix} * (\dot{m}_{fuel} + \dot{m}_{air})}{M_{mix}}}{\frac{Y_{CO_2mix}}{M_{mix}} - \frac{Y_{CO_2egr}}{M_{egr}}} \quad (12)$$

Knowing the mass flow of EGR gases, the EGR rate is calculated from equation 7.

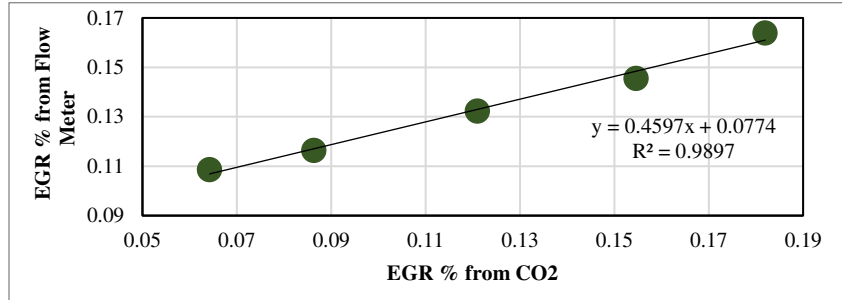


Figure 19. EGR flow calibration, CO2 mass balance vs orifice flow meter measurement.

Baseline Testing

The baseline testing defines the initial performance condition of the SCE and helps to compare it with the available commercial natural gas engine offered by Cummins (6-cylinder 12-liter NG engine). The baseline consisted of two sections: preliminary engine development and baseline efficiency.

The EGR effect on efficiency and the best thermal efficiency with baseline hardware configuration was evaluated for the SCE. A CA50 timing sweep was carried out using fixed EGR rate values to find the best efficiency ignition timing. EGR rates from 5% to 20% were tested using fixed CA50, 16 bar IMEP, 50°C intake temperature, and 1200 RPM. The results obtained are presented in Figure 20-Figure 23. For the cases of less EGR rate, lower values of CA50 cases were not evaluated due to evident engine knock.

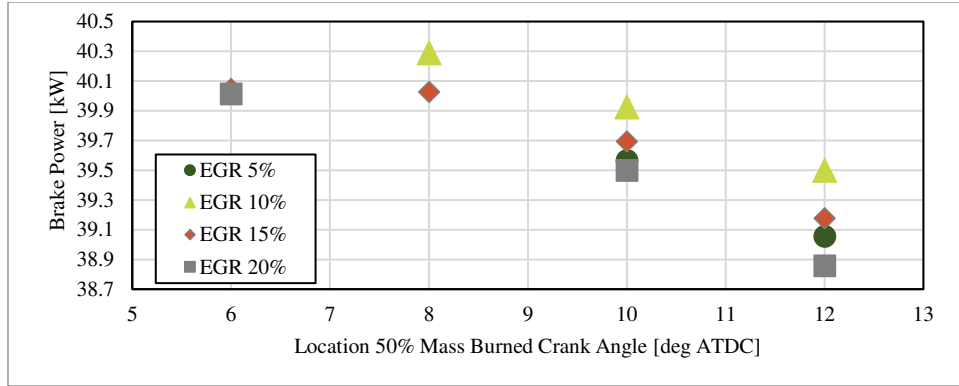


Figure 20. 50% Mass burned crank angle vs. brake power for different EGR rates. Operation conditions: 1200RPM, target IMEP 16 bar.

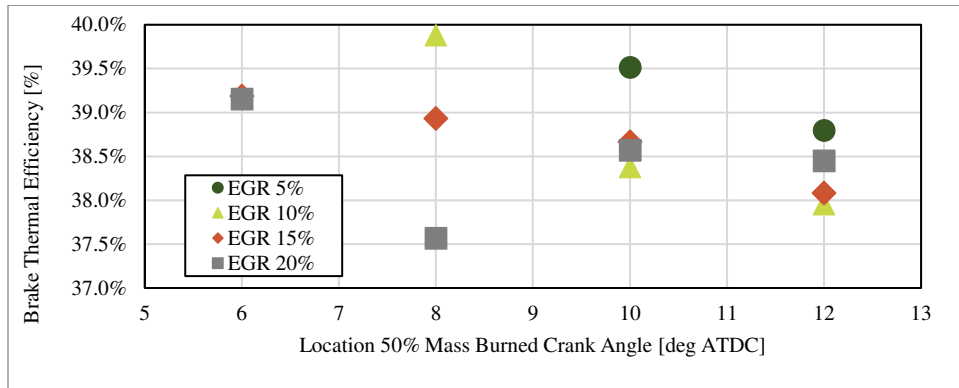


Figure 21. 50% Mass burned crank angle vs. brake thermal efficiency for different EGR rates. Operation conditions: 1200RPM, IMEP 16 bar.

Maximum values of brake power occur as CA50 is varied. The highest value is observed at 10% EGR. Larger timing values related to later CA50 show a pronounced decrease in power for every EGR rate because heat release timing is suboptimal, occurring too late. The best thermal efficiency (39.9%) is at the 10% EGR and earliest knock-free CA50 value (8 deg ATDC). Additionally, all the cases evaluated achieved values above 39% BTE. Two instances of mid-EGR rate and 8 deg CA50 show lower values that disrupt the trend. The peak pressure coefficient of variance (COV) is minimized at 8 deg CA50 for every condition tested (Figure 23). IMEP COV is below 1% for every condition tested and overall follows an inverse trend of the BTE and brake power (Figure 22). The lowest values are presented at the higher BTE conditions for COV metrics.

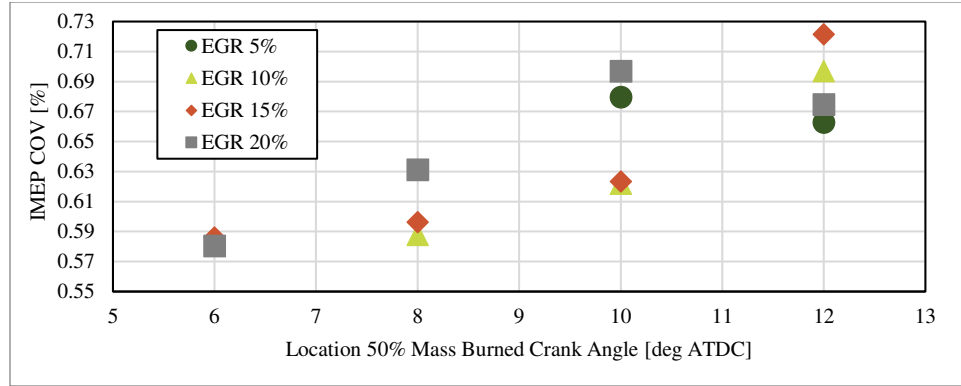


Figure 22. 50% Mass burned crank angle vs. peak pressure COV and IMEP COV for different EGR rates. Operation conditions 1200RPM, IMEP 16 bar.

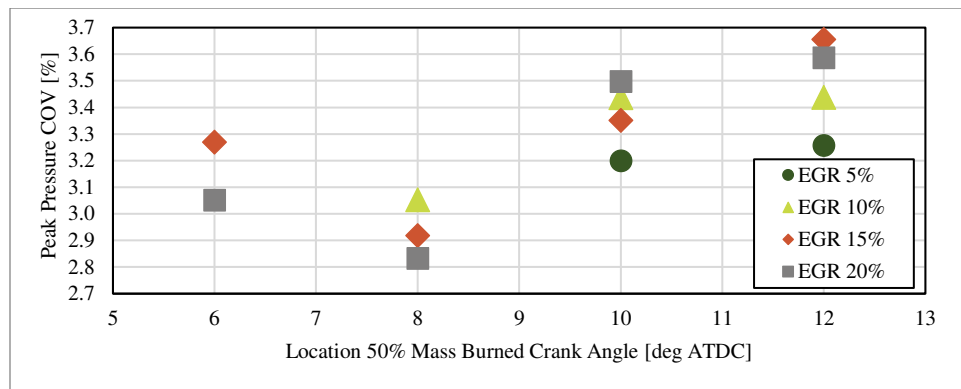


Figure 23. 50% Mass burned crank angle vs. COV and IMEP COV for different EGR rates. Operation conditions 1200RPM, IMEP 16 bar.

Combustion duration is characterized by the 0% to 10% and the 10% to 90% mass fraction burned duration in crank angle degrees shown in Figure 24 and Figure 25. The first indicates the ignition delay or the time it takes to initiate the combustion process. In this case, it takes a short period from 1 to 7 deg to reach 10% of the mass burned. The ignition delay decreases as the value of CA50 decreases (advanced). Combustion duration or 10-90% mass fraction burned, follows the same trend varying from 10 to 17 deg. Heat release and cylinder pressure trends are directly related to the ignition timing. As spark timing advances, combustion occurs earlier with higher peak pressure. Faster combustion events show higher BTE and brake power.

Combustion intensity (CI) metric was used to prevent the engine from entering the knocking phase while allowing for higher BTE. In this case, specific testing was performed using CI as a control variable for the ignition instead of the mass burned percentage location. The lowest value of CI tested is 10% showing the lowest BTE decreases, and combustion instability and misfire are

present for lower values. The highest value of CI required to operate the engine without approaching the medium and high knocking range is 40%. The BTE and Brake torque follow the same pattern; higher CI gives both metrics the best values (Figure 26).

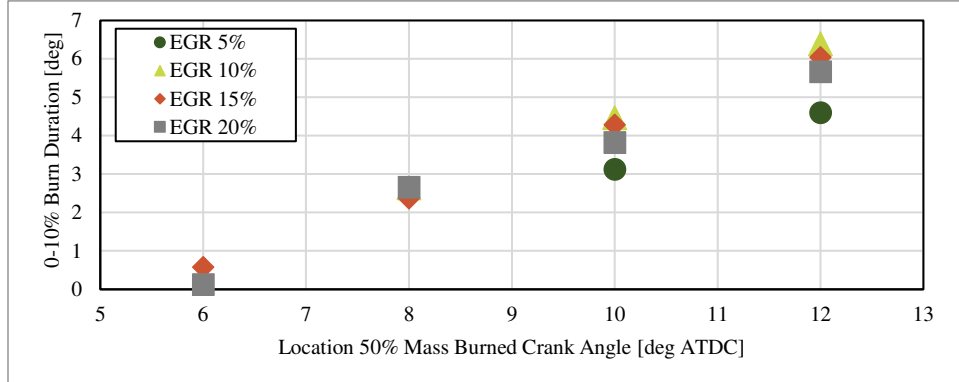


Figure 24. 50% Mass burned crank angle vs. 0-10% Burn Duration. Operation conditions 1200RPM, IMEP 16 bar.

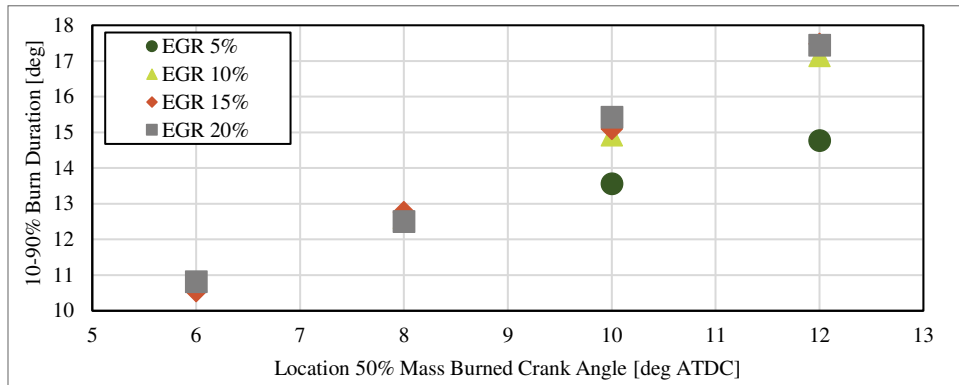


Figure 25. 50% Mass burned crank angle vs. 10-90% Mass Burned. Operation conditions 1200RPM, IMEP 16 bar.

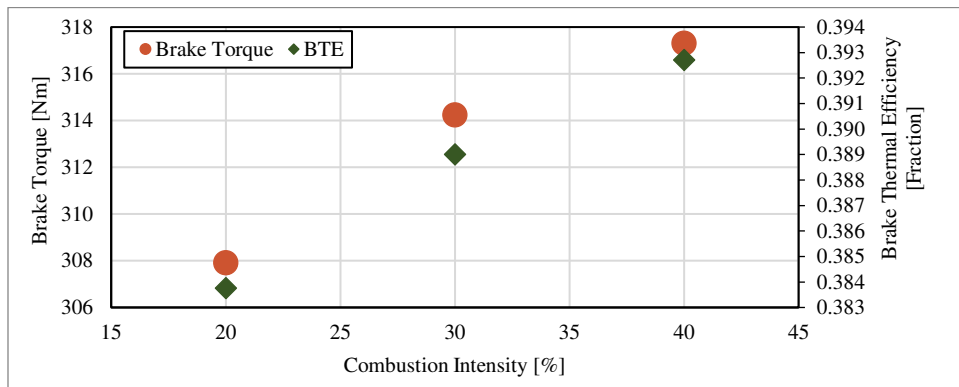


Figure 26. Combustion Intensity vs Brake Torque and Brake Thermal Efficiency. Operation conditions IMEP 16 bar, EGR 20%.

Figure 27 presents the efficiency map contour with respect to BMEP and the rate of EGR. The best BTE is on the upper line at a higher BMEP and 8% EGR rate. Subsequent lines show bell-shaped decreasing behavior of the BTE, pointing to a higher BTE area around 12% rate EGR. A similar contour for ignition timing variation where the best efficiency region is located at 8 deg ATDC for the location of 50% mass burned, with a range of BMEP from 15.7 to 16.3 bar. The baseline testing intended to identify the knock limits of the engine with the hardware configuration selected.

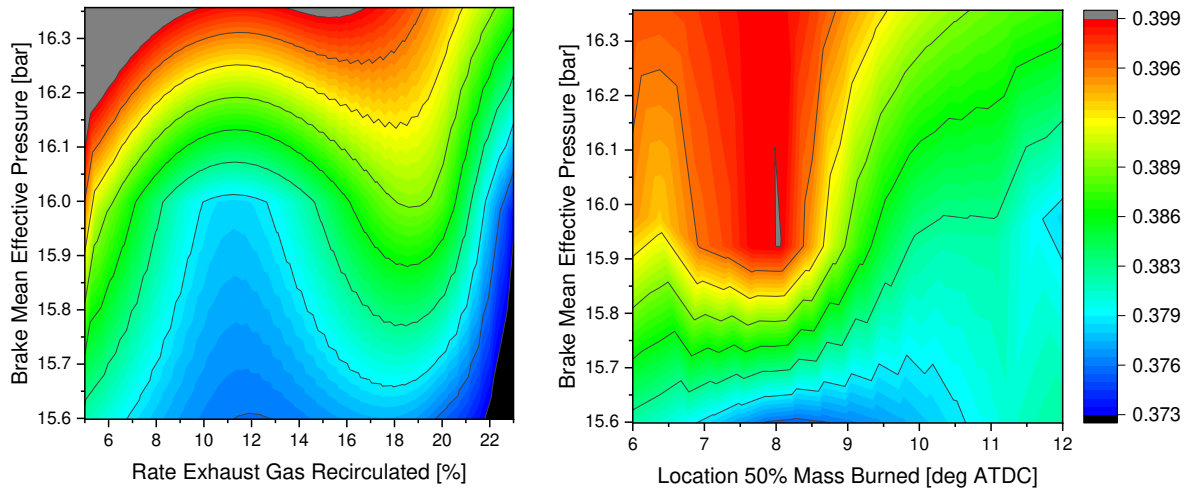


Figure 27. Efficiency map showing contours of constant BTE with respect to Left: EGR rate [%] and BMEP [bar]; Right: Location 50% Mass Burned [deg ATDC] and Brake Mean Effective Pressure [bar]

Crank resolute data is used to analyze the combustion characteristics. Figure 28 presents the effect of the EGR rate over cylinder pressure and normalized apparent heat release rate. Keeping constant ignition timing target, CA50 10 deg ATDC and IMEP 16 bar, the highest peak pressure and steepest pressure increase are for the most efficient BTE case, 10% EGR, while the lowest case is for the least 5% EGR rate. No apparent difference is encountered for the highest 15% EGR rate and 20%. Concerning the Normalized Apparent Heat Release Rate (AHRR), the same trend is present with faster and earlier combustion for the most efficient case (EGR 10%). Important to note that the shoulder on the last part of the heat release for this case, which indicates the presence of a second combustion event, is considered End Gas Autoignition (EGAI) [20].

Figure 29 presents the effect of ignition timing in terms of the location of CA50 for the same EGR rate of 15% and IMEP 16 bar. The pressure trace divides into two couples, with the earliest CA50 showing very similar results and a close relationship for the cases of 10 and 12 deg ATDC CA50.

As expected, the highest BTE is present with the earliest ignition timing, explained by the behavior of the AHRR that has the steepest trace heat release and the same combustion duration, with only a minor difference indicating the presence of a second heat release (combustion event under EGAI conditions) for the 6 deg ATDC case. The 10 and 12 deg ATDC cases decrease on the slope and show how the energy from the fuel is released later during the crank rotation.

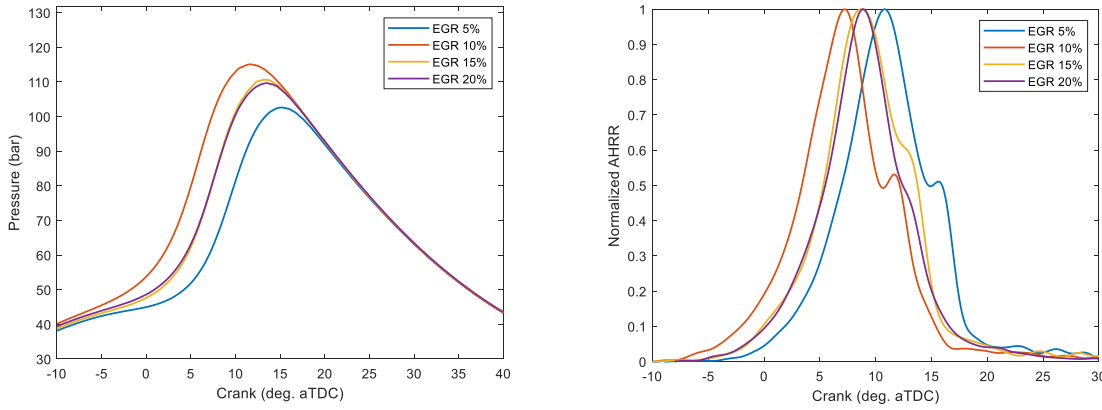


Figure 28. Effect of EGR rate: Left: Crank Angle Degree After TDC vs. Mean In-Cylinder Pressure Trace [bar]; Right: Crank Angle Degree After TDC vs Normalized Accumulated Heat Release

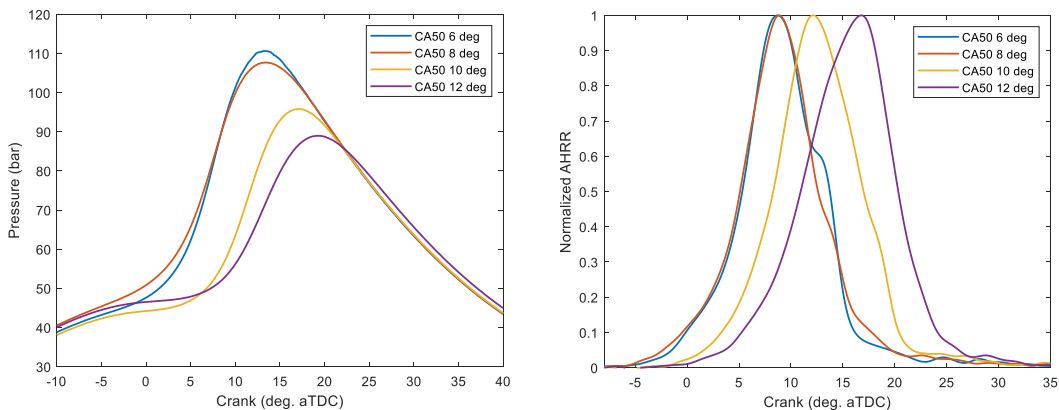


Figure 29. Effect of Ignition Timing, Location 50% Mass Burned (CA50): Left: Crank Angle Degree After TDC vs. Mean In-Cylinder Pressure Trace [bar]; Right: Crank Angle Degree After TDC vs Normalized Accumulated Heat Release.

Chapter 3 - Controlled End Gas Auto Ignition

The research work described in this section corresponds to testing the SCE operated under C-EGAI conditions with a high EGR rate. CDF-improved piston design and a pre-chamber sparkplug are used as part of the tools to achieve diesel-like BTE [27].

Pistons

Three prototype pistons were tested. Pistons were machined from cast iron blanks similar to the ones used on the original diesel version of the Cummins engine used for the test cell (Figure 30). This introduces inherent restrictions on the available geometry for the bowl, piston deck height, and cooling characteristics due to the geometry of the internal cooling galleries. The piston design and optimization were carried out using CONVERGE CFD and GT-Power, as described by Bestel [24]. Optimized CR was selected using the GT-Power model calibrated with experimental baseline data provided [25]. Twenty-two different prototypes were simulated using CONVERGE CFD. Other designs were generated from the optimized CR range, varying the Squish Area Ratio (Squish Area/Bore Area) and adjusting the bowl depth and shape to keep the CR within the desired ranges (Table 2).

The simulation results show that tumble flow benefits thermal efficiency due to the decreased ignition delay, faster flame propagation away from the spark plug, and reduced heat losses [26]. The three prototypes presented in this work combine the best-simulated performance from the original 22 designs. Piston A offers the highest ITE since it has the lowest piston heat loss; having these characteristics, the optimized CR suggests the highest value from all prototypes. However, Piston B also yields a similar BTE with a much longer ignition delay, which can negatively affect ignitability, and a higher propensity to knock, which gives less room for the Controlled End-Gas Autoignition (C-EGAI) operation. Due to this characteristic, a lowered CR is used for this design. Piston C combines the attributes of designs A and B, with limited knock tendency but better ignitability, and a middle-range CR.



Figure 30. Top: Prototype A piston. CR 16; Middle: Prototype B piston. CR 13.3:1; Bottom: Prototype C piston. CR 15:1.

Table 2. Prototype pistons CR and Squish ratio.

Prototype	A	B	C
CR	16.2	13.3	15:1
Squish	57%	80%	75%

Test Cell Modifications.

Woodward Fast Turbulent Igniter (FTI) Pre-chamber sparkplug was installed (centrally located spark plug) for fast and consistent ignition and to enhance reliability at higher loads [28] (Figure 31)



Figure 31: Woodward FTI pre-chamber spark plug.

Engine Test Procedure

The test was conducted using pipeline natural gas with a methane number of 74 and LHV 47099 kJ/kg, using the MWM calculator. Table 3 outlines the operating conditions considered and

Table 4 shows the average NG composition used for the Cummins ISX15 SCE testing [29].

Table 3: Tested Cummins ISX15 engine operating conditions.

Parameter	Piston A	Piston B	Piston C	Unit
CR	16.2	13.3	15:1	Ratio
Eng. Spd	1200	1200	1200	RPM
IMEP	12-15	18 - 20	14-17	bar
BMEP	11-14	17-19	13-16	bar
Spark Timing	5 - 10	10 - 20	5 - 15	deg. bTDC
CA50	14	5.5 - 14	9 - 14	deg. aTDC
EGR	30	13- 30	10 - 30	%
Coolant Temp	85	85	85	°C
Intake Manifold Temp	33-35	33-35	33-35	°C
Intake Manifold Pressure	1.5 – 1.7	2.0 - 2.32	1.5 – 1.9	bar
Exhaust Manifold Pressure	1.6 – 1.8	2.2 - 2.5	1.7 – 2.1	bar

Table 4: NG compositions used during the Cummins ISX15 engine testing.

Species	Percentage
CH4	85.2%
C2H6	10.4%
C3H8	1.9%
C4H10	0.39%
C5H12	0.10%
C6H14	0.02%
N2	0.36%
CO2	1.69%
MN	74.9

Prototype A piston

The research project's goal was to improve BTE under operative conditions. This motivated using the less conventional piston design and higher CR for the prototype iteration. This design included thick walls from the cooling galleries to the top surfaces of the piston due to the use of a diesel-minded blank piston cast. This design indicated the best compromise of reduced knock tendency and improved BTE. Meanwhile, as presented in Figure 5, the engine operated under heavy knock conditions with loads, not above 14 bar IMEP, CA50 10 deg ATCD, and 30% EGR. Reduced EGR rates enhanced the knock tendency, and no earlier CA50 was used without experiencing uncontrollable knock leading to full autoignition mode.

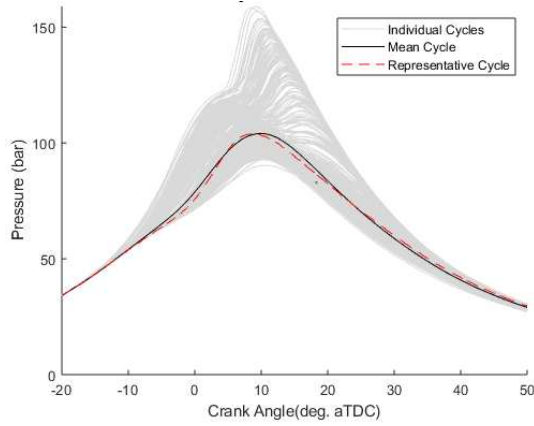


Figure 32. Top: Cylinder pressure vs. crank angle for piston A 16:1 CR. Engine operating conditions: 1200 RPM, $\varphi = 1$, IMAP1.4 bar, EGR rate 30%, IMT 30°C. Bottom: Piston A as removed from the engine.

Upon determining that this prototype could not provide consistent data under varying operating conditions, we removed the piston from the engine. The piston displayed notable surface discoloration, hinting at the presence of uncooled hot spots during engine operation, potentially due to the thickness of the piston walls. Given the constraints in place, and with no further room for design improvements, it was opted to discard this piston without further testing.

Engine Performance

Brake Power and Efficiency

Figure 33 shows Brake Power (BP) over the range of CA50 ignition targets for all the tests conducted under different EGR substitution rates for prototype B. As shown, brake power is significantly improved as the CA50 is advanced; earlier values of CA50 are achieved for the higher EGR substitution rate cases. Figure 34 shows brake thermal efficiency (BTE) for all cases tested for prototype B. The BTE increases with earlier CA50 from an average of ~0.5% for each 2 deg of advance, achieving a peak value of 46% for the case with a 30% EGR rate at 6 deg ATDC CA50. This improvement is expected as early CA50 moves peak pressure closer to TDC, resulting in more efficient conditions to convert cylinder pressure into effective work at the crankshaft. Half of the conditions presented are above 44% BTE. Figure 35 illustrates IMEP results for prototype B, where an inverse linear correlation of CA50 and IMEP is observed for all EGR rate cases. The highest IMEP was found at 20% EGR rate, with the following closest values at 13% and 30%. This case shows up to 2% points of difference on BTE. The increase in BTE comes from the constant or increased power produced while reducing the amount of fuel consumed; thus, the engine was operating more efficiently.

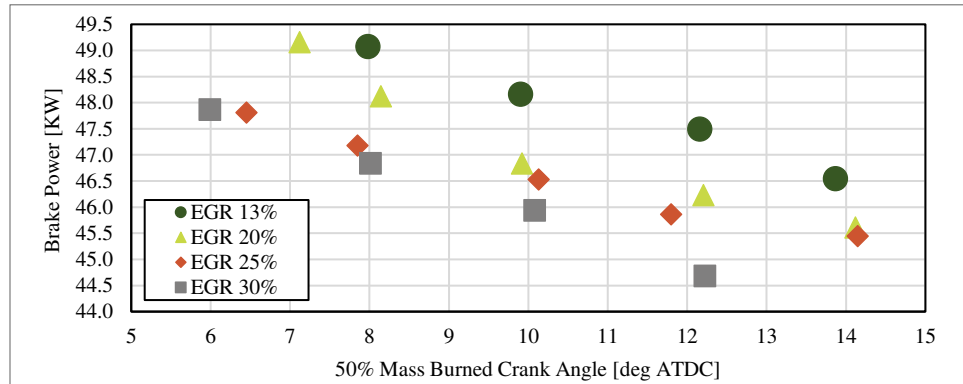


Figure 33. Location 50% Mass Burned Crank Angle vs. Brake Power for all EGR substitution rates piston B 13.3:1 CR. Engine operating conditions: 1200 RPM, $\phi = 1$, IMAP2.2 bar.

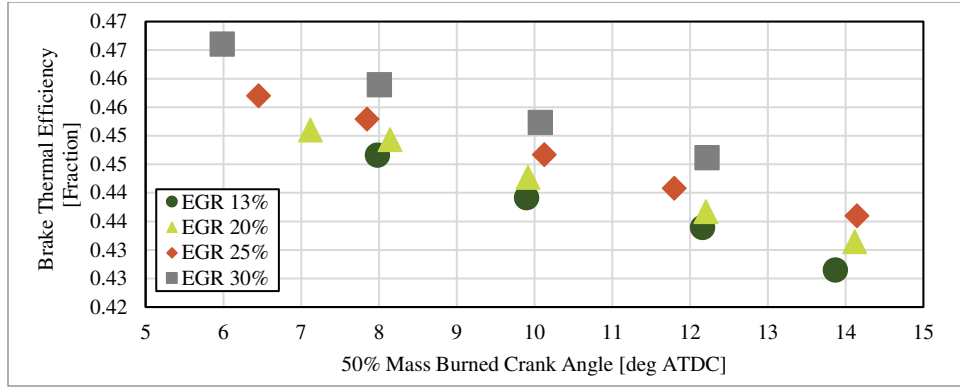


Figure 34. Location 50% Mass Burned Crank Angle vs. Brake Thermal Efficiency for all EGR substitution rates piston B 13.3:1 CR. Engine operating conditions: 1200 RPM, $\varphi = 1$, IMAP2.2 bar.

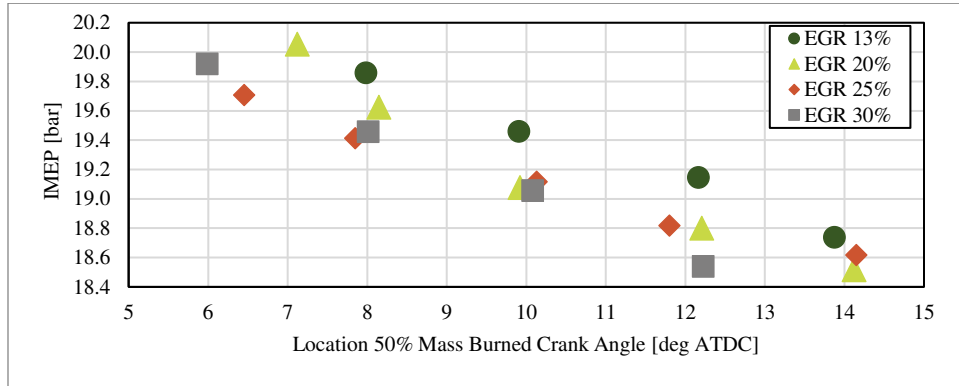


Figure 35. Location 50% Mass Burned Crank Angle vs. Indicated Mean Effective Pressure for all EGR substitution rates piston B 13.3:1 CR. Engine operating conditions: 1200 RPM, $\varphi = 1$, IMAP2.2 bar.

Figure 36 shows Brake Power (BP) over the range of CA50 ignition targets for the tests conducted under different EGR substitution rates for prototype C. As expected, brake power is significantly improved as early CA50 is targeted. The same trends as with piston B were observed, i.e., higher EGR substitution allows early CA50. The Power range for this piston is 10 kW on average less than piston B, as higher loads were impossible to achieve due to a heavy knock tendency. Figure 37 shows brake thermal efficiency (BTE) for prototype C. The BTE increases with earlier CA50 and is higher as more EGR is used. The BTE for this piston ranges from 44 to 48.5% for the conditions tested, presenting an improvement of almost 2% from piston B. The range of target CA50 for piston C is considerably reduced, as no earlier than 9 deg ATDC is achieved even with 30% EGR. All the conditions tested for this piston C are above the benchmark of 44% BTE. Figure 38 presents the IMEP results for prototype C, ranging from 15.5 to 16.8 bar IMEP. An inverse linear correlation of CA50 and IMEP is observed for all EGR rate cases.

There is a particular behavior for the 25% EGR case where the two earliest CA50 target values produce almost equal BP. Advancing the timing did not increase the BP as the knock tendency increased above the range, which benefited the combustion efficiency (the Knock index from the LECM increased by 15% between these two data points). In general, the improvement in BTE from piston C is attributed to the increase of almost 2 points in CR and the improved geometry that allows enhanced swirl with the stepped bowl bottom. The bottom of the bowl is not flat; a steeped section in the middle was included to increase the CR. This step creates a tick cooler cooling wall in the area less prone to overheating, while for all the other wall surfaces on the piston, the minimum thickness was achieved from the piston surface to the cooling galleries.

For both pistons, the increase in efficiency at higher EGR rates suggests that more effective combustion is achieved at higher EGR rates. This is consistent with previous experimental work on the CFR engine [18]. There is also evidence of an indirect relationship between BP and BTE for some conditions tested. More power is achieved for piston C with 20% EGR and earlier CA50; the BTE increases for the latest (12 deg ATDC) and the middle target (10 deg ATDC) but decreases for the earliest CA50. This indicates that the optimal CA50 target for this condition is 10 deg ATDC CA50 where the amount of EGAI induced benefits the overall engine efficiency. Section 2.5 of [28] presents a detailed explanation of the piston design optimization.

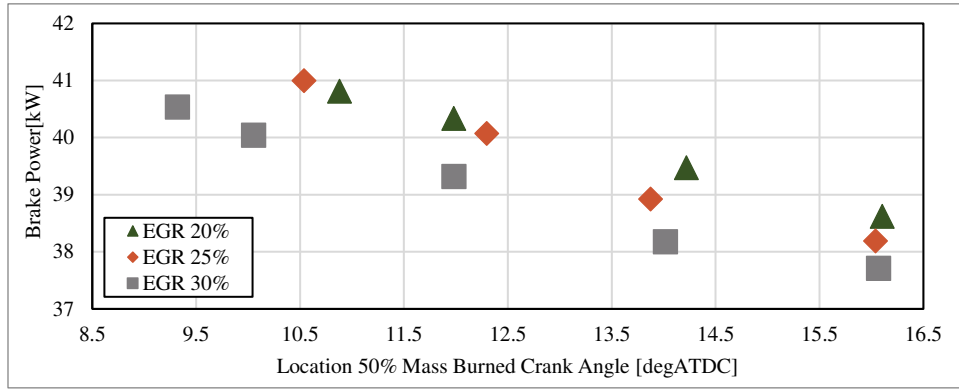


Figure 36. Location 50% Mass Burned Crank Angle vs. brake power for all EGR substitution rates piston C 15:1 CR. Engine operating conditions: 1200 RPM, $\phi = 1$, IMAP 1.8 bar.

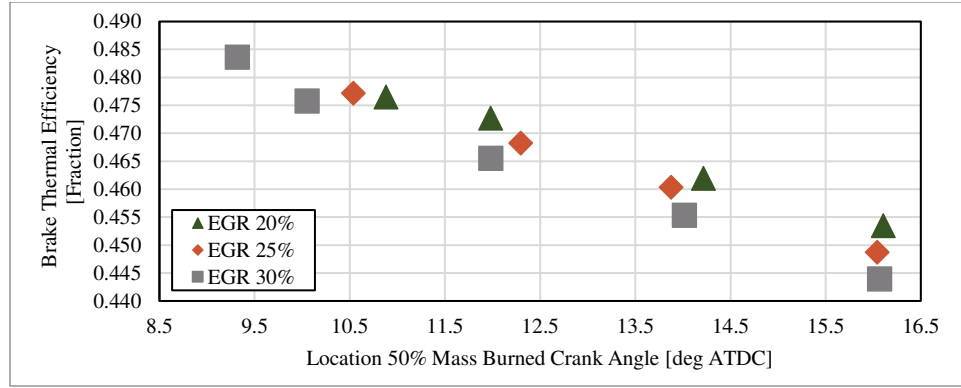


Figure 37. Location 50% Mass Burned Crank Angle vs. Brake Thermal efficiency for all EGR piston C 15:1 CR substitution rates. Engine operating conditions: 1200 RPM, $\varphi = 1$, IMAP 1.8 bar.

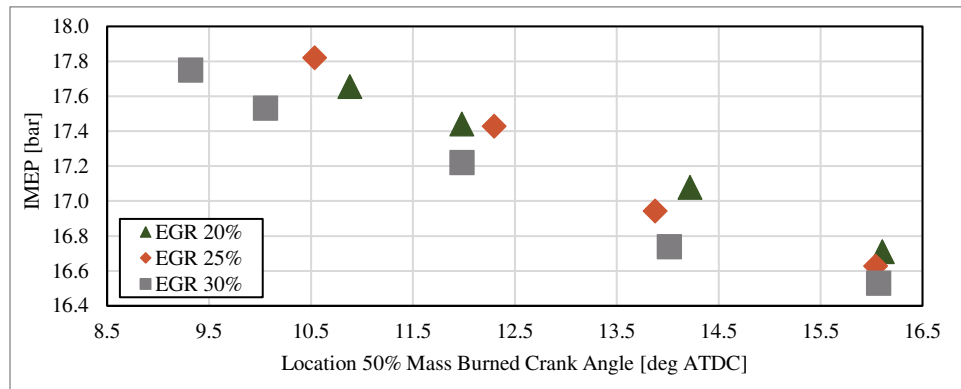


Figure 38. Location 50% Mass Burned Crank Angle vs. Indicated Mean Effective Pressure for all EGR piston C 15:1 CR substitution rates. Engine operating conditions: 1200 RPM, $\varphi = 1$, IMAP 1.8 bar.

Combustion Characteristics

In-Cylinder Pressure, Indicated Mean Effective Pressure, and Heat Release Rate

In-cylinder pressure data are analyzed over the range of conditions tested. Figure 39 shows the in-cylinder pressure for a constant EGR and IMAP for four different CA50s for piston B. The plots show all the 1000 cycles in grey with the mean cycle highlighted. A progressive increase in Peak Pressure (PP) from 115 to 145 bar PP is observed as earlier CA50 is used. The steepest increase in pressure is monitored for early CA50 values, achieving a flat top curve shape for the most efficient case tested, which corresponds to CA50 6 deg ATDC shown at the bottom of the figure.

Representative and mean cycles follow almost identical trends. The overall disparity from all the cycles recorded is low, with the thinnest grey shape in the most efficient case, indicating more stable combustion.

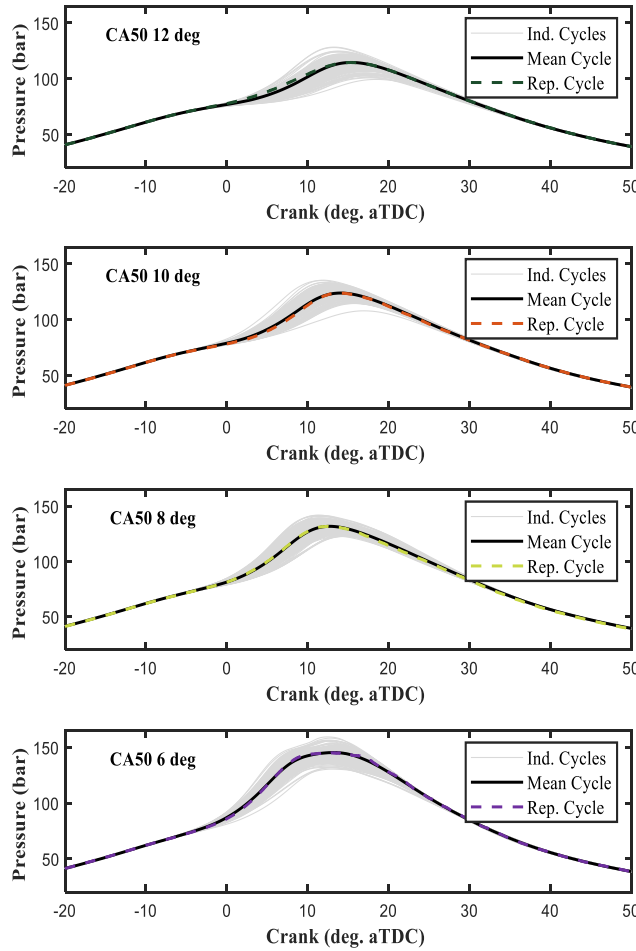


Figure 39. Variation of Cylinder Pressure vs. Crank angle for different locations 50% mass burned for 13.3:1 CR piston. Engine operating conditions: 1200 RPM, $\varphi = 1$, EGR substitution rate 30%, IMAP 2.2 bar.

Similar plots for piston C are presented in Figure 40. The pressure traces indicate the lower peak cylinder pressure for the conditions tested. The max value achieved was 115 bar, while piston B was 145 bar, as the load on both cases differed, with lower IMAP for piston C. The 9 deg ATDC CA50 case for piston C shows the closest profile to the flat top pressure profile mentioned for piston B. For piston C, there is no evident variation in the location of the peak cylinder pressure with respect to CA50, as the shape of the pressure trace is similar for all the four CA50 values targeted, with the difference in magnitude of peak values.

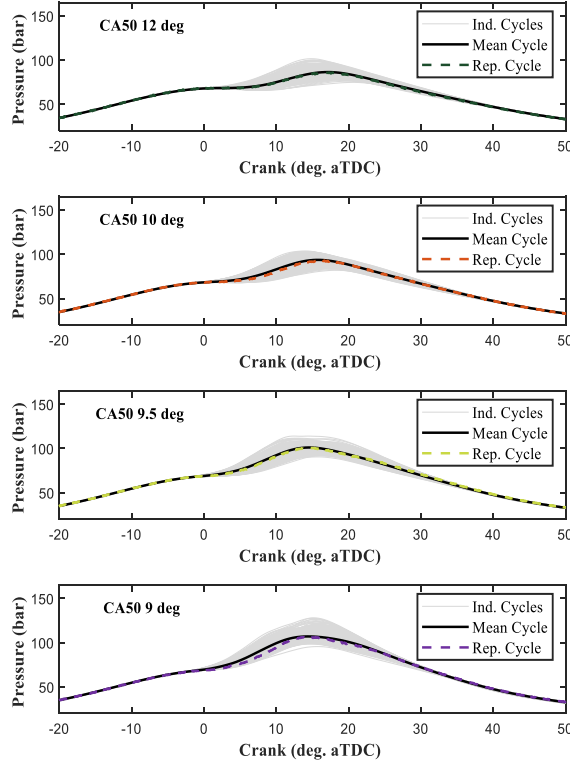


Figure 40. Variation of Cylinder Pressure vs. Crank angle for different locations 50% mass burned for 15:1 CR piston. Engine operating conditions: 1200 RPM, $\varphi = 1$, EGR substitution rate 30%, IMAP 1.8 bar.

The apparent heat release rate (AHRR), Normalized AHRR, and apparent integral heat release (AIHR) at constant EGR and IMAP with a variation of CA50 are presented in Figure 41 for piston B and Figure 42 for piston C. As timing advances to achieve earlier CA50, the heat release trace gives a steeper slope for both pistons. The maximum AHRR stays relatively constant for all four cases in piston B, while in piston C, a clear second peak in heat release means lower peak values. This condition is a clear indication of EGAI. CA50 6 deg ATDC shows the presence of EGAI from 7 to 15 deg ATDC, where the onset of EGAI and the second rise in heat release is evident. In the same way, for this case, the combustion ends sooner, on average, before 25 deg ATDC while for the other cases, there is still a release of energy after this CA.

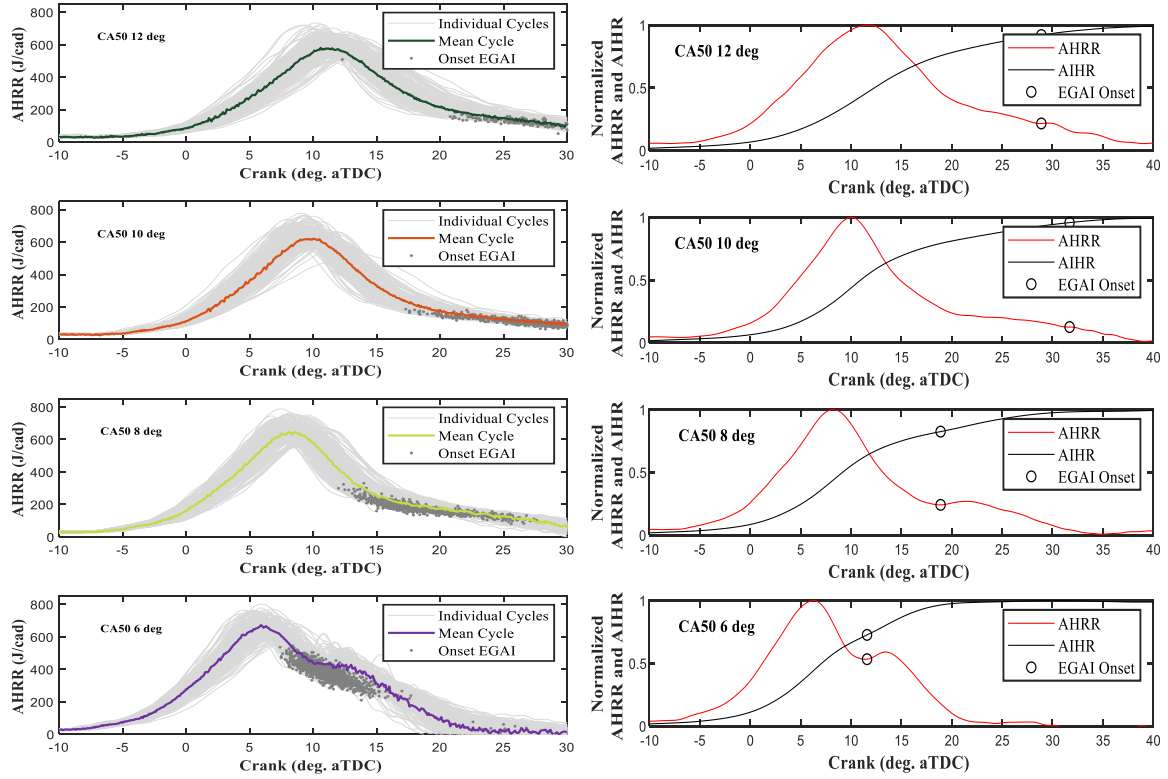


Figure 41. Left: Variation of AHRR vs. Crank angle for different locations 50% mass burned. Right: Normalized AHRR and AIHR vs. Crank angle for multiple locations 50% mass burned. Piston B 13.3:1 CR. Engine operating conditions: 1200 RPM, $\varphi = 1$, EGR rate 30%, IMAP 2.2 bar.

The Normalized AHRR and AIHR are presented for the average cycles of each piston and the CA50 case studied. These normalized plots show more clearly the pattern of the EGAI and how it induces a second combustion event. Cases CA50 6 deg ATDC for piston B and 9.5 and 9 deg ATDC for piston C show a visible slope change detected by the EGAI onset methodology. In cases with minimal slope change, the calculation falls on conditions where the slope change is within the threshold selected for the analysis without being visible on the normalized AHRR trace. The plots also include the onset of EGAI, which is more prevalent with earlier CA50 and occurs earlier in the cycle. The scattered onset of EGAI is seen as later CA50 is used with a tightly clustered pattern for the earliest CA50.

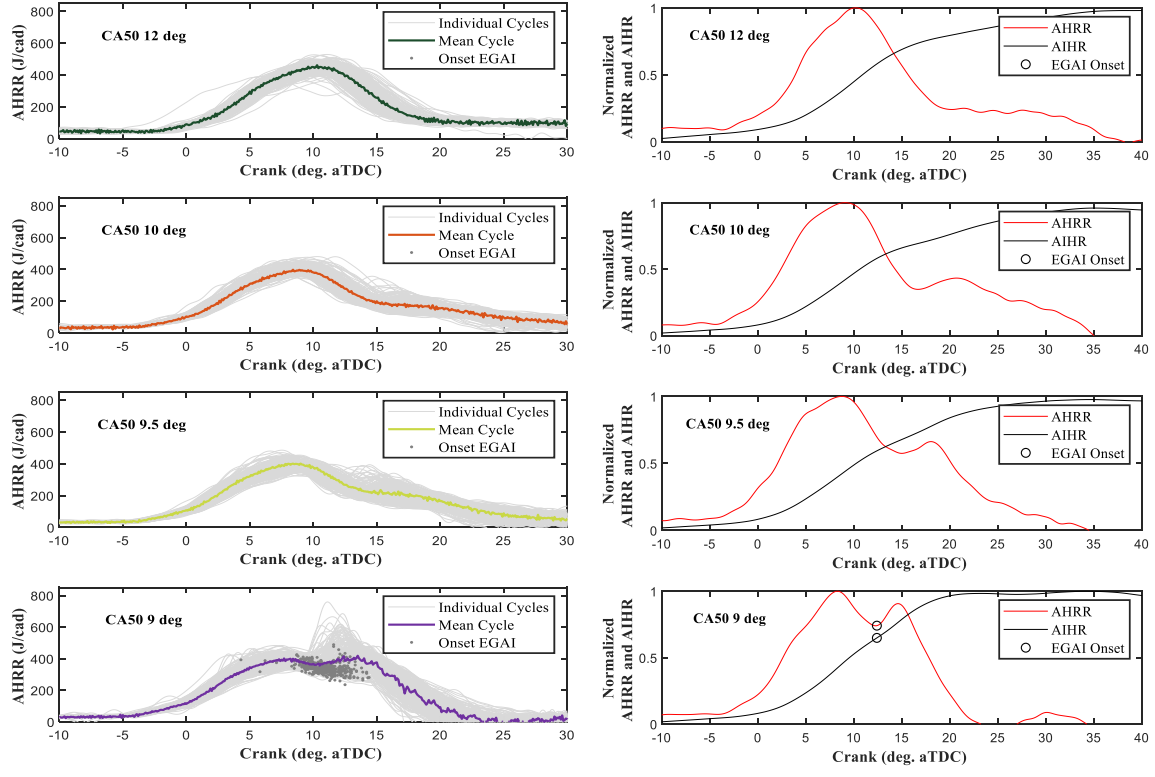


Figure 42. Left: Variation of AHRR vs. Crank angle for different locations 50% mass burned. Right: Normalized AHRR and AIHR vs. Crank angle. Piston C 15:1 CR. Engine operating conditions: 1200 RPM, $\varphi = 1$, EGR rate 30%, IMAP 1.8 bar.

Combustion Duration

Figure 43 shows the combustion duration of 10-90% mass fraction burned (MFB) for piston B. EGR addition significantly affects engine combustion. Rapid burning occurs with less EGR added to the mixture, and as the CA50 is advanced, i.e., higher BTE achieved, the combustion duration also decreases. The most significant change in combustion duration for an EGR case is with a 30% substitution rate when the duration changes 10 CA deg. This indicates how high EGR content mixtures are more susceptible to improvement in BTE with the optimal CA50. Additionally, combustion duration decreases as flame propagation is increased with higher temperatures (lower EGR rate). The occurrence of end gas auto-ignition plays an essential role in the faster burn. The most efficient cases achieved contain EGAI and shorter combustion durations.

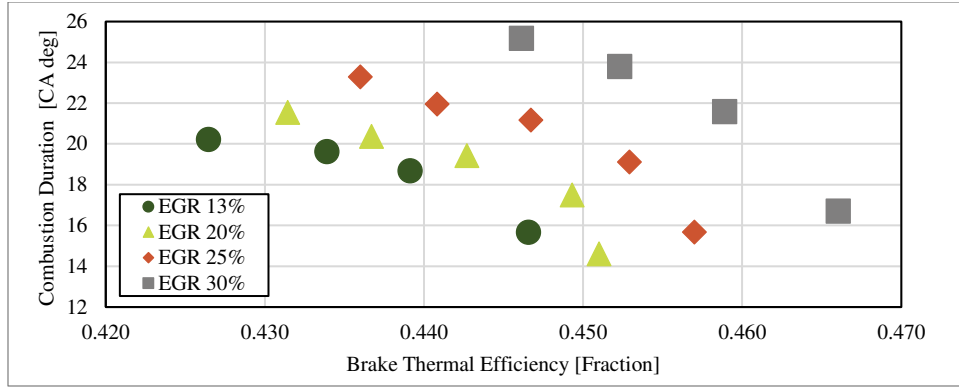


Figure 43. Brake Thermal Efficiency vs Combustion Duration. Engine Piston B 13.3:1 CR. Engine operating conditions: 1200 RPM, $\varphi = 1$, EGR rate 30%, IMAP 2.2 bar.

Figure 44 presents the comparison of BTE and combustion duration for piston C. less influence of EGR rate is evidenced for this case. The higher BTE is directly related to shorter combustion duration.

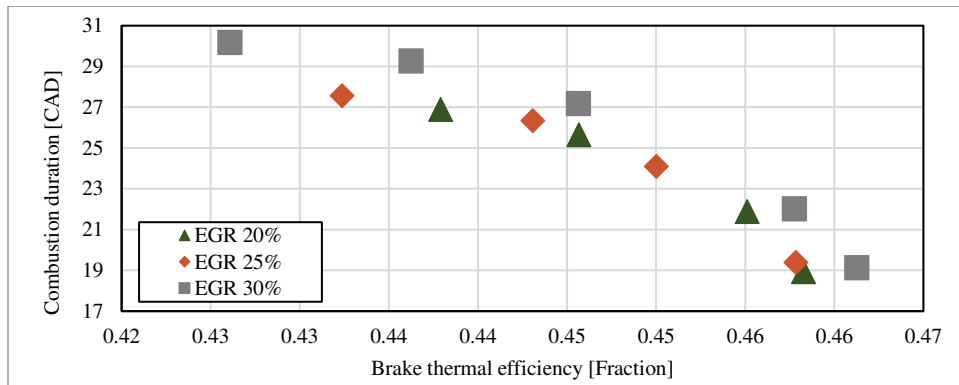


Figure 44. Brake Thermal Efficiency vs Combustion Duration. Engine piston C 15:1 CR Engine operating conditions: 1200 RPM, $\varphi = 1$, IMAP 1.8 bar.

Combustion stability.

Cycle-by-cycle pressure trace plots indicate the level of combustion stability. Two parameters are thresholds for acceptable combustion stability, Peak Pressure Coefficient of Variance (PP COV), and IMEP Coefficient of Variance (IMEP COV). Values below 3% and 10% for IMEP COV and PP COV, respectively, are acceptable. Figure 45 and Figure 46 show these pistons' B and C metrics in all the cases tested. Earlier CA50 always led to the best BTE results, correlating with lower COV values for both plots.

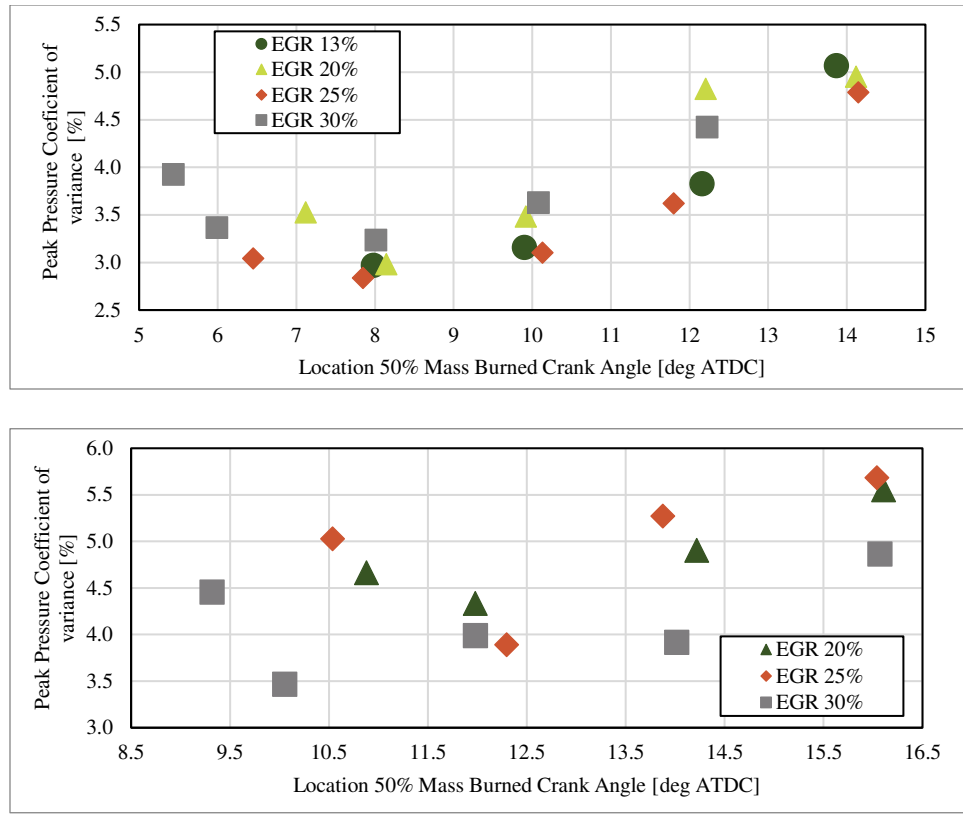


Figure 45. Location 50% Mass Burned Crank Angle vs Peak Pressure Coefficient of Variance. Top: piston B 13.3:1 CR. Engine operating conditions: 1200 RPM, $\varphi = 1$, IMAP 2.2 bar. Bottom: piston C 15:1 CR Engine operating conditions: 1200 RPM, $\varphi = 1$, IMAP 1.8 bar

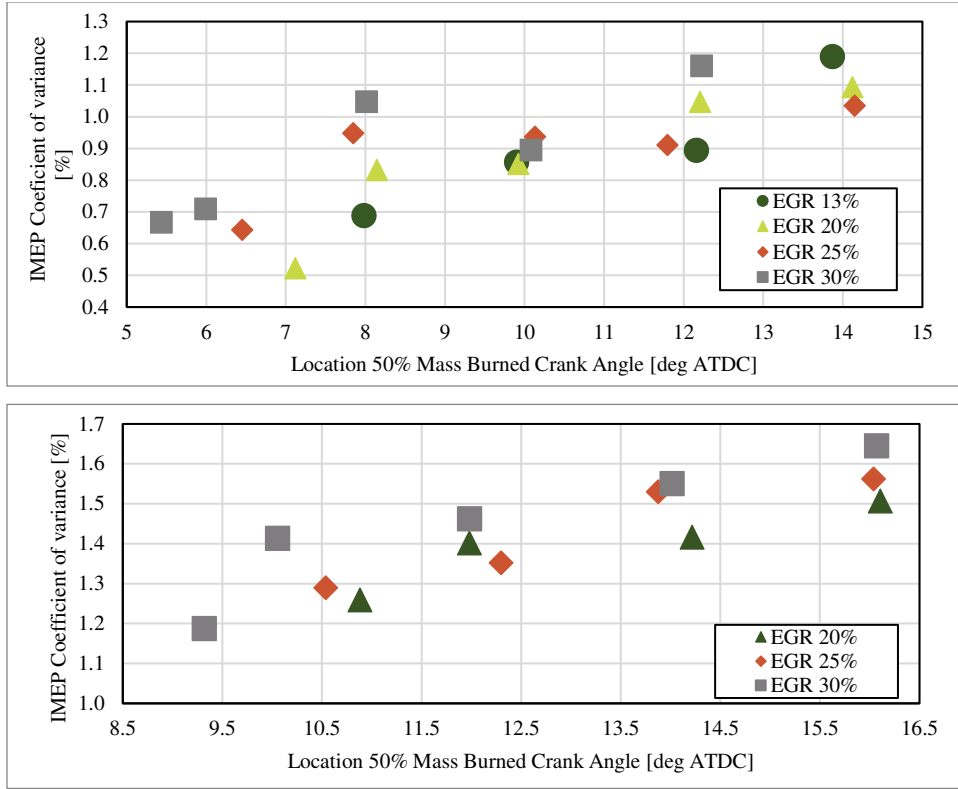


Figure 46. Location 50% Mass Burned Crank Angle vs IMEP Coefficient of Variance. Top: piston B 13.3:1 CR. Engine operating conditions: 1200 RPM, $\varphi = 1$, IMAP 2.2 bar. Bottom: piston C 15:1 CR Engine operating conditions: 1200 RPM, $\varphi = 1$, IMAP 1.8 bar

Fraction End Gas Auto Ignition f-EGAI

EGAI is the key to achieving BTE improvements for the conditions evaluated in this work. Figure 47 and Figure 48 present the f-EGAI calculated with respect to location CA50 and f-EGAI vs BTE, respectively. The addition of EGR into the fresh mixture allows the use of early CA50 while keeping the engine below the knock threshold for the engine for piston B, showing a progressive trend of increase of f-EGAI as earlier CA50 is used. It is possible to induce EGAI in a more significant fraction for the cases with higher content of EGR. Also, for piston B, a CA50 of 10 was the minimum combustion advance necessary to induce measurable EGAI, corresponding to an f-EGAI of 0.05.

Meanwhile, for piston C the f-EGAI trends are less clear. While the cases with more EGR have an exponential tendency, the engine was not operated under constant EGAI mode, except for one case, as only two conditions tested show estimated values of f-EGAI above 15%. Lower values

of f-EGAI are challenging to quantify with the methodology used, so they are not considered EGAI combustion [20].

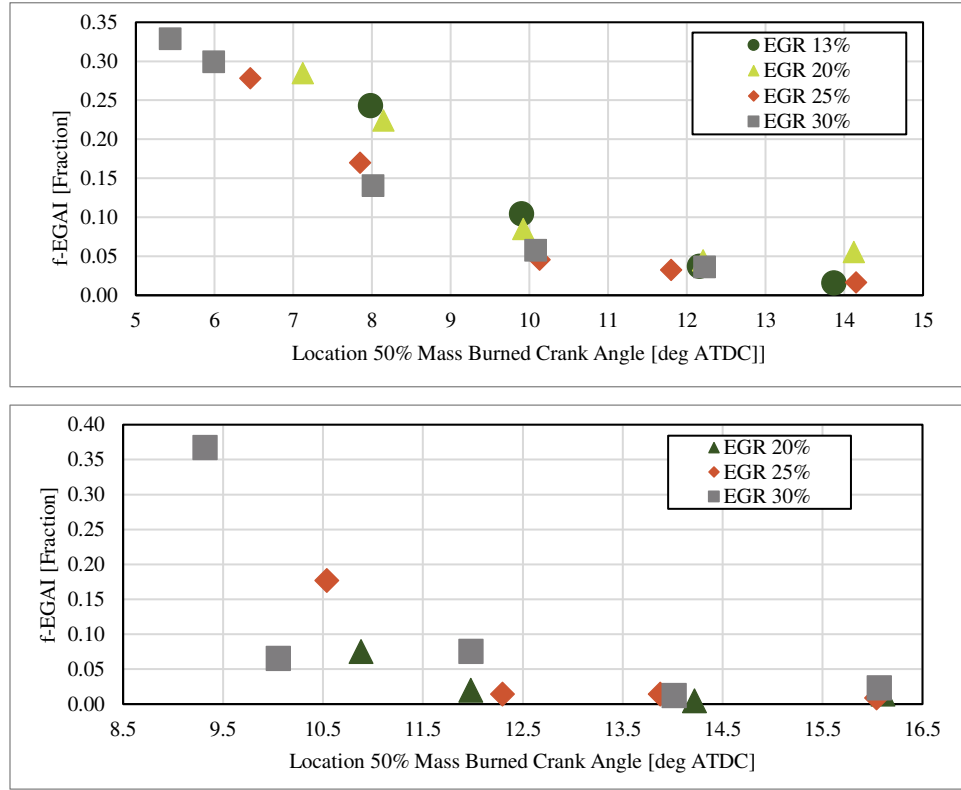


Figure 47. Location 50% Mass Burned Crank Angle vs. Fraction End Gas Auto Ignition. Top: piston B 13.3:1 CR. Engine operating conditions: 1200 RPM, $\phi = 1$, IMAP 2.2 bar. Bottom: piston C 15:1 CR Engine operating conditions: 1200 RPM, $\phi = 1$, IMAP 1.8 bar

The effect of f-EGAI on BTE is presented in Figure 48. The results indicate that enhancing the presence of EGAI is linearly related to the increased BTE for piston B. For piston C, the engine operated on normal combustion (EGAI less than 10%) except for two cases. The highest BTE was achieved with high f-EGAI, as was found for piston B. Piston B presents a linear increasing behavior of BTE as more EAGI is induced for each EGR rate studied. The comparison of these plots indicates that piston B was successfully operated under C-EGAI as the increases of f-EGAI are gradual and consistent for all EGR cases. Piston C was used under conditions with f-EGAI up to 35%, but there was always a steep jump in the presence of f-EGAI, and no correlation is evidenced for the EGR rate or CA50.

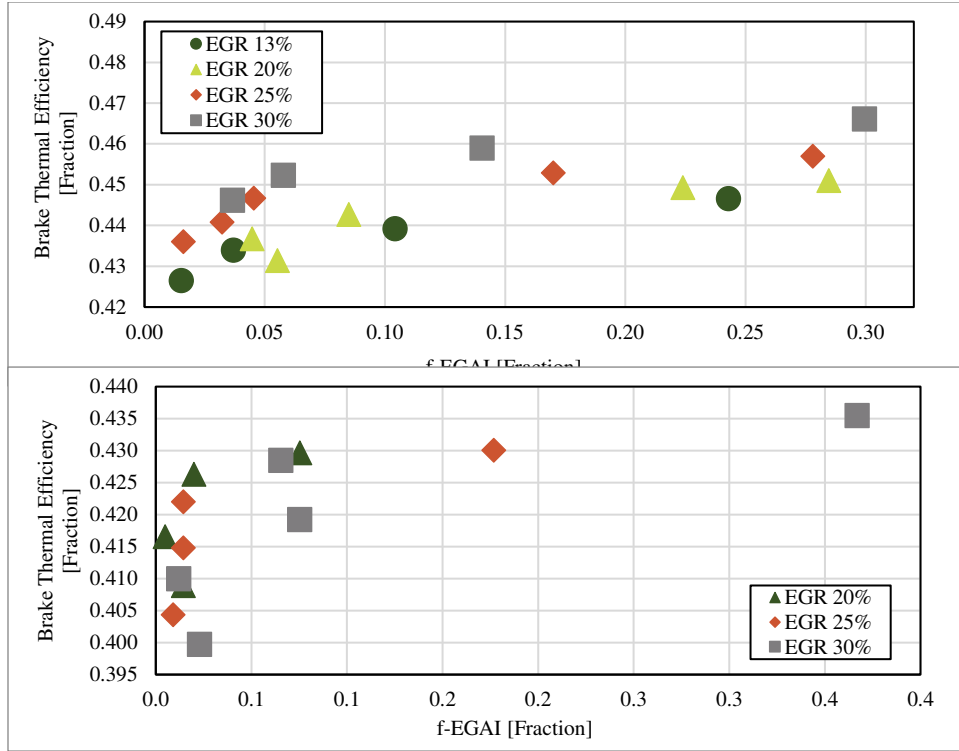


Figure 48. Fraction End Gas Auto Ignition vs. Brake Thermal Efficiency. Top: piston B 13.3:1 CR. Engine operating conditions: 1200 RPM, $\varphi = 1$, IMAP 2.2 bar. Bottom: piston C 15:1 CR Engine operating conditions: 1200 RPM, $\varphi = 1$, IMAP 1.8 bar

Analysis of Best BTE Case

Piston B

The highest BTE case is studied in detail, as the primary goal of this research was improvements in BTE at maximum brake torque speed. The achievement of C-EGAI conditions aided by the utilization of high EGR allowed to reach high PP without inducing undesirable knock. The engine operation under these conditions showed peak brake thermal efficiency of 46% using an EGR ratio of 29.4%.

This condition was achieved with f-EGAI of 28.5% and CIM of 35%. The peak cylinder pressure was 144 bar. IMEP was 19.92 bar, and the estimated BP was 43.36 kW. Figure 49 shows the in-cylinder pressure trace, the apparent heat release, and normalized AHRR for the best efficiency condition.

The heat release profile shows the onset of the EGAI between 6 and 10 deg ATDC, which increases the efficiency as more fuel is burned completely in the combustion chamber. Pressure traces show good combustion stability, validated by the COV of IMEP of 0.52% and the COV of peak pressure of 3.52%. The intake manifold pressure was 2.32 bar, and the engine speed was 1200 RPM. Exhaust gas temperature EGT was 562°C, a relatively low value corresponding to the complete combustion and high efficiency achieved. Engine-out brake-specific emissions were relatively low, with values of 2.05, 1.51, and 3.46 g/bkW-hr for CO, THC, and NOx, respectively.

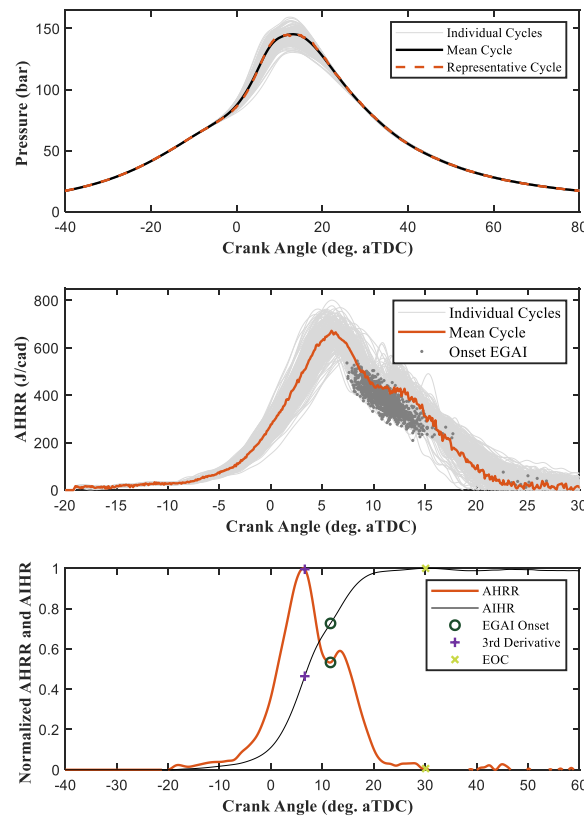


Figure 49. Cylinder Pressure vs. Crank Angle (Top), Apparent Heat Release Rate vs. Crank Angle (Middle), and Normalized Apparent Heat Release Rate vs. Crank Angle (bottom) is the best brake thermal efficiency condition achieved. Engine operating conditions: 1200 RPM, $\phi = 1$, EGR rate 30%, IMP 2.3 bar, CA50 6 deg aTDC.

For the best BTE case, Figure 50 presents the variation cycle by cycle of the estimated f-EGAI. This plot shows how for 1000 cycles recorded, the combustion variability in terms of f-EGAI is within .1 fraction or 30%. Using CIM as a control strategy for the ignition on the LECM unit allows the engine to run under these conditions. Operation with traditional engine ignition

management would lead to uncontrollable knock. The plot shows that f-EGAI varies on a sinusoidal pattern, but the controller can maintain good stability, enabling high BTE.

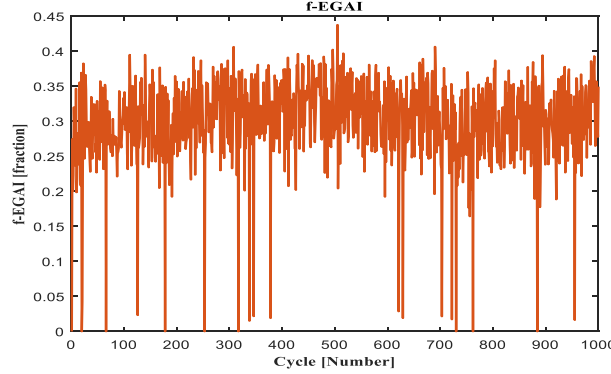


Figure 50. Cycle recorded number vs. Fraction End Gas Auto Ignition. Engine operating conditions: 1200 RPM, $\varphi = 1$, EGR rate 30%, IMP 2.3 bar, CA50 6 deg aTDC.

Figure 51 shows the cycle-by-cycle combustion duration and 50% mass burned CA50 location. These metrics follow a similar pattern to the f-EGAI, having a direct relation among them but with approximately the same stability and variation. The results demonstrate the effective control of the combustion using the CIM as the target metric for the ignition strategy in the LECM. This control technique successfully enhances efficiency, allowing combustion to maintain a high level of EGAI without compromising the variability of the combustion metrics or inducing heavy knock.

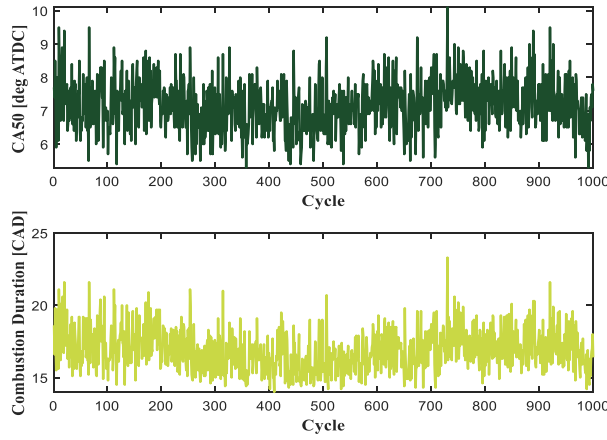


Figure 51. Cycle recorded number vs. location for 50% mass burned (up), Combustion duration (down). Engine operating conditions: 1200 RPM, $\varphi = 1$, EGR rate 30%, IMP 2.3 bar, CA50 6 deg aTDC.

Piston C

The engine operation under conditions of C-EGAI showed peak brake thermal efficiency of 48.5% using an EGR ratio of 30%. This condition was achieved with f-EGAI of 35%. The peak cylinder pressure was 125 bar. IMEP was 17.8 bar, and the estimated BP was 38.5 kW. Figure 52 shows the in-cylinder pressure trace, the apparent heat release, and normalized AHRR for the best efficiency condition.

The heat release profile shows the onset of the EGAI between 8 and 15 deg ATDC, which increases the efficiency as more fuel is burned completely in the combustion chamber faster. Pressure traces indicated good combustion stability, validated by the COV of IMEP of 1.8% and the COV of peak pressure of 5.32%. The intake manifold pressure was 1.8 bar, and the engine speed was 1200 RPM. Exhaust gas temperature EGT was 541°C, a relatively low value corresponding to the complete combustion and high efficiency achieved.

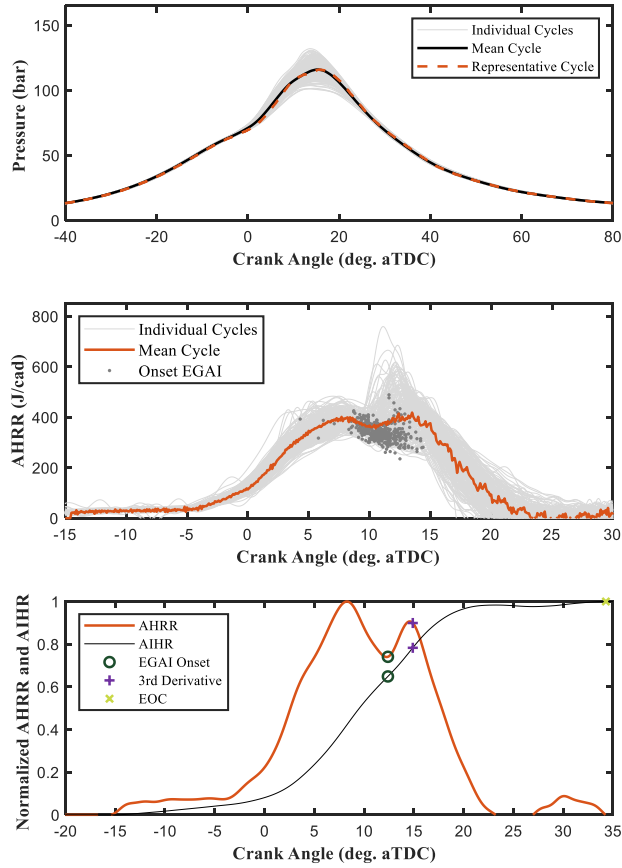


Figure 52. Cylinder Pressure vs. Crank Angle (Top), Apparent Heat Release Rate vs. Crank Angle (Middle), and Normalized Apparent Heat Release Rate vs. Crank Angle (bottom) best brake thermal efficiency conditions achieved. Piston C 15:1 CR.

Engine operating conditions: 1200 RPM, $\varphi = 1$, EGR rate 30%, IMAP 1.8 bar, CA50 9 deg ATDC.

Uncertainty analysis

Uncertainty analysis for measurements, based on the method outlined in [30], was used to estimate the precision of experiments. The following equation was employed for calculation:

$$U = \frac{\sigma}{\sqrt{n}} * 100\% \quad (13)$$

Here, n represents the number of repeated tests, and the standard deviation (σ) is calculated using the following equation:

$$\sigma = \sqrt{\frac{\sum_{i=1}^n (x_i - \bar{x})^2}{n-1}} \quad (14)$$

$$\bar{x} = \sum_{i=1}^n x_i / n \quad (15)$$

When the engine achieved thermal equilibrium, 1000 combustion cycles were recorded, and 5-minute data sets were logged from the main control LabVIEW system at a rate of 2 Hz. This LabVIEW system encompasses various engine parameters, including fuel consumption, speed, pressures, temperatures, and emissions. Highest measurement uncertainties are detailed in Table 5. The overall experimental uncertainty comfortably met the 5% target value [30], affirming the trustworthiness the data. The only parameter out of the range is the EGR flow. The value shown in Table 5 represents the most challenging condition, observed at 13% EGR during the baseline testing. An enhancement in accuracy, reducing uncertainty to less than 5% during high-efficiency testing, was obtained with an upgraded orifice plate on the EGR flow measurement device.

Table 5. Uncertainty estimated for measured variables.

Variable	Uncertainty U [%]
Brake power	0.81
Fuel mass Flow	0.8546
EGR flow	7.563
Air flow	1.84
Air Fuel Ratio	1.559
Ignition timing	1.26

The uncertainty in BTE is determined based on the measurement error associated with each variable used in the BTE equation. BTE depends on variables such as fuel flow, brake power, and lower heating value.

$$BP = \frac{(IMEP - FMEP) V_d N}{n_R} \quad (16)$$

$$BTE = \frac{BP}{\dot{m}_f LHV} \quad (17)$$

The calculation error is derived from the uncertainties associated with the variables used in estimating BTE. Equation 18 represents the error differential equation, and Equation 17 is evaluated within Equation 18 to obtain the final BTE error presented in Equation 19.

$$\Delta f = \sqrt{\left(\frac{\partial f}{\partial x_1} \Delta x_1\right)^2 + \left(\frac{\partial f}{\partial x_2} \Delta x_2\right)^2} \quad (18)$$

$$\Delta BTE = \sqrt{\left(\frac{1}{\dot{m}_f LHV} \Delta BP\right)^2 + \left(-\frac{BP}{LHV} \frac{1}{\dot{m}_f^2} \Delta \dot{m}_f\right)^2} \quad (19)$$

Updated plots illustrating the error in brake power estimations can be found in Figure 53. BP is the primary source of error in BTE since the measurement uncertainty of fuel flow and lower heating value (LHV) is quite low. The error in BP ranges from ± 0.8 kW in extreme cases, equating to an error of $\pm 2\%$.

Figure 54 displays the BTE error as a function of the CA50 location. The BTE error is ± 0.019 fractional units or $\pm 1.9\%$. In practical terms, this means that for the worst efficiency condition tested, where the BTE estimate is 44.6%, the actual BTE could fall within the range of 42.7% to 46.5%.

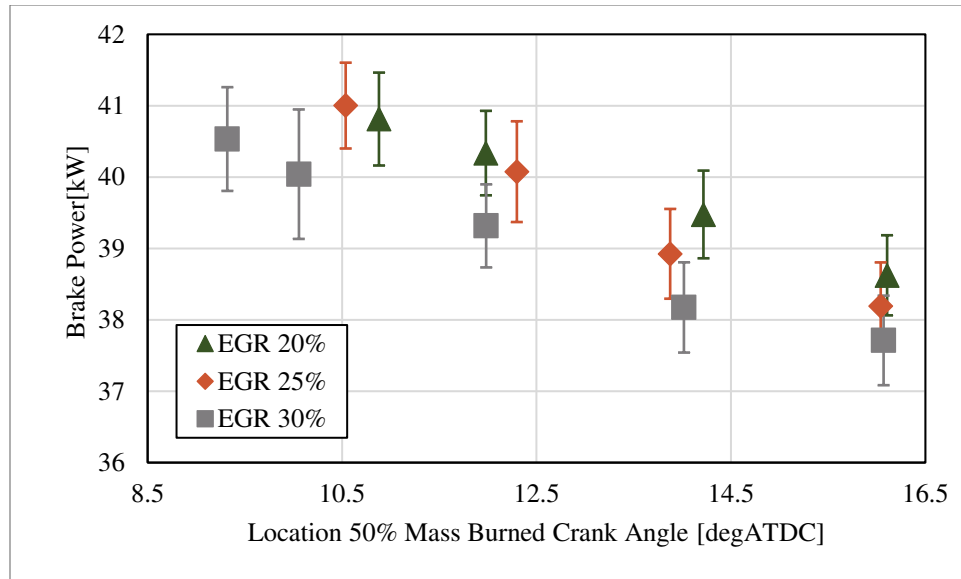


Figure 53. Location 50% Mass Burned Crank Angle vs. Brake power with error bars for all EGR piston C 15:1 CR substitution rates. Engine operating conditions: 1200 RPM, $\varphi = 1$, IMAP 1.8 bar

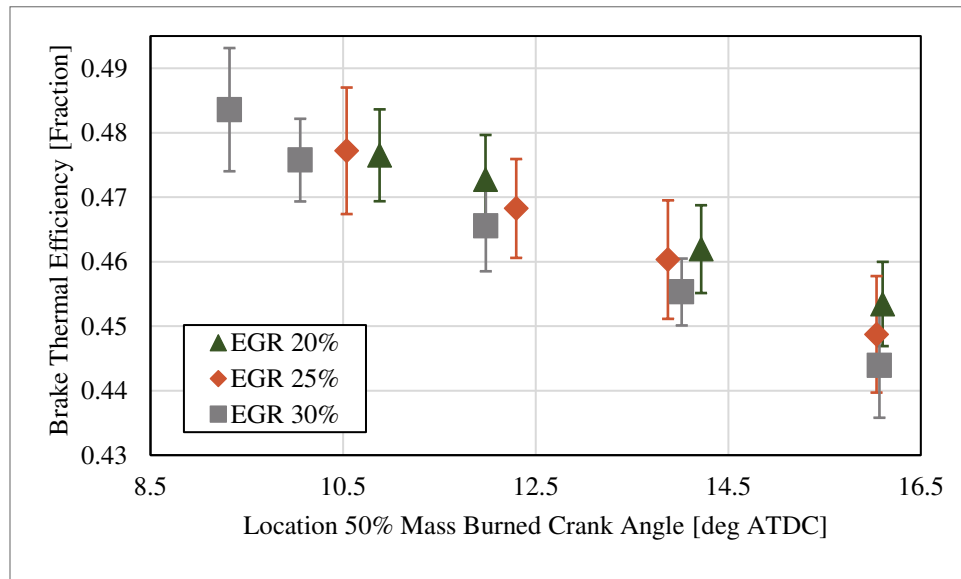


Figure 54 Location 50% Mass Burned Crank Angle vs. Brake Thermal efficiency with error bars for all EGR piston C 15:1 CR substitution rates. Engine operating conditions: 1200 RPM, $\varphi = 1$, IMAP 1.8 bar

The cases presented exclusively involve testing the C prototype piston. This specific piston demonstrated the highest error among all the experiments conducted.

Chapter 4 – Exhaust Emissions from high-efficiency NG engine.

Emissions were measured for the 13.3:1 and 15:1 piston test run. Each set of data is analyzed in the upcoming section.

Nitrogen Oxides

Figure 55 shows brake-specific Nitrogen Oxide (NOx) emissions for different EGR rates used with respect to CA50 for piston B, while Figure 56 is piston C. The NOx chemistry is governed primarily by the post-combustion local in-cylinder temperatures leading to increased NOx emissions as peak temperatures rise. For each EGR rate tested, there is a linear increasing NOx trend as earlier CA50 is used (from the previous section, high BTE was found as earlier CA50 was used). This indicates that the in-cylinder temperatures increased as earlier timing was used but decreased for every increment on EGR added for all the CA50 except the earliest one. In these earliest CA50 cases, there is a decrease in NOx emissions, demonstrating that conditions for low-temperature combustion both increase BTE and decrease NOx.

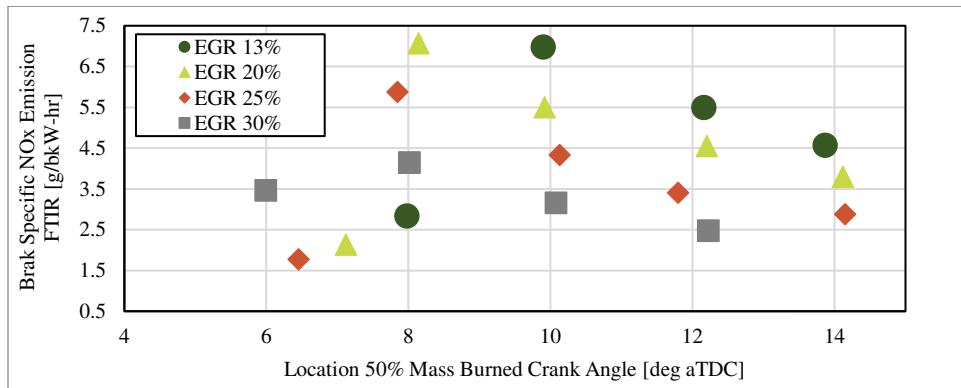


Figure 55. Location 50% Mass Burned Crank Angle vs Brake-specific NOx Emission mission for all EGR rates. Engine operating conditions: 1200 RPM, $\varphi = 1$, IMP 2.2 bar, CR 13.3:1.

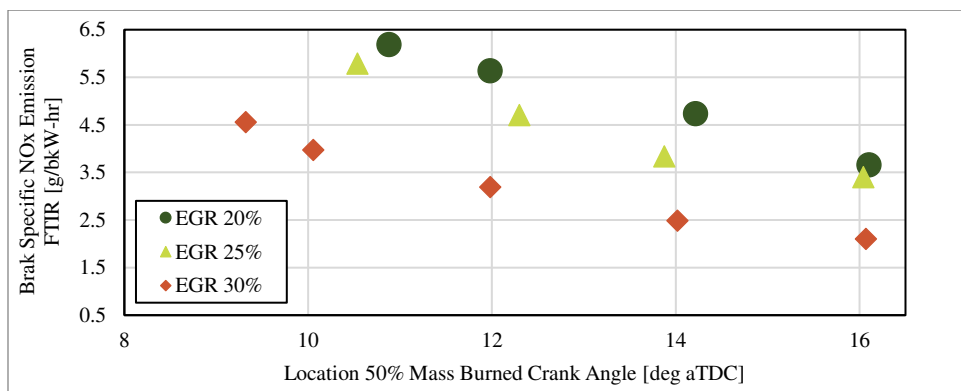


Figure 56. Location 50% Mass Burned Crank Angle vs Brake-specific NOx Emission mission for all EGR rates. Engine operating conditions: 1200 RPM, $\varphi = 1$, IMP 1.8 bar, CR 15:1.

Total Hydrocarbons

Figure 57 shows brake-specific Total Hydrocarbons (THC) over the range of conditions tested. THC measurements include Non-methane (NMHC) and non-ethane (NMNEHC) HCs for piston C and Figure 58 for piston C, which are essential because of their reactivity and potential to promote o-zone. CH₄ emission is vital to be considered as it is a potent greenhouse gas, about 25 times the warming potential of CO₂. The THC emissions were quantified using Siemens 600 series Fidamat analyzer and normalized by brake power. As shown, the THC emissions decreased with earlier CA50, which produces higher BTE and BP, as faster and more complete combustion is, achieved [9]. The addition of EGR shows an essential influence on THC emissions, as 30% of EGR cases had almost 60% higher THC emissions. However, for the higher EGR rate cases, the ignition timing and consequent BTE achieved are more influential on THC emissions; for the 30% EGR cases, the difference between the highest and lowest value represents a 60% reduction.

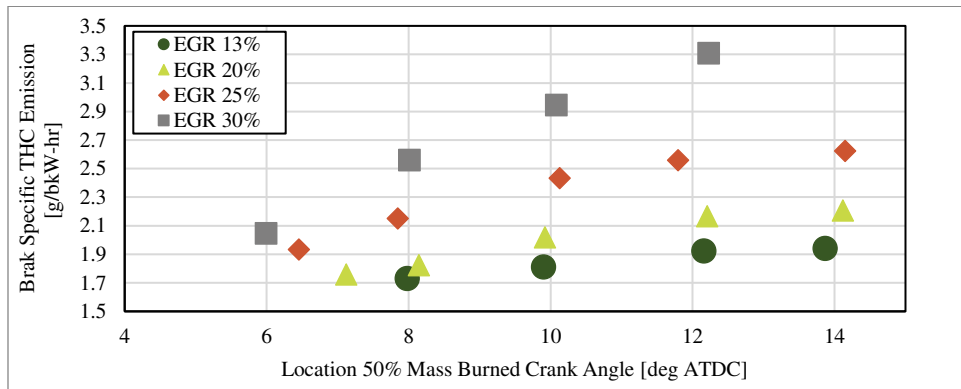


Figure 57. Location 50% Mass Burned Crank Angle vs Brake-specific THC Emission for all EGR rates. Engine operating conditions: 1200 RPM, $\varphi = 1$, IMP 2.2 bar, CR 13.3:1.

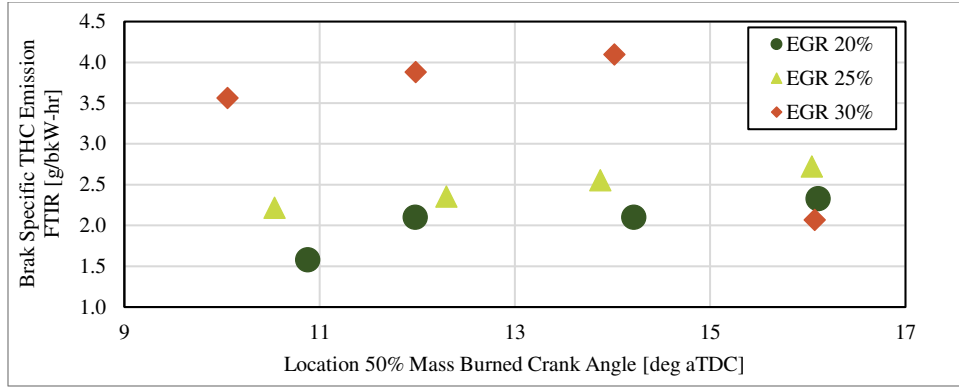


Figure 58. Location 50% Mass Burned Crank Angle vs Brake-specific THC Emission for all EGR rates. Engine operating conditions: 1200 RPM, $\varphi = 1$, IMP 1.8 bar, CR 15:1.

FTIR emission measurement in Figure 59 and Figure 60 for pistons B y C respectively, shows the detailed composition of the THC gases for a constant EGR CA50 swept. NM and NE HCs have a flat behavior for all CA50 cases, while a strong correlation is evident for the CH4 measurement to the THC measured. This is explained as early CA50 induces faster and more complete combustion, then less CH4 remaining on the exhaust gases.

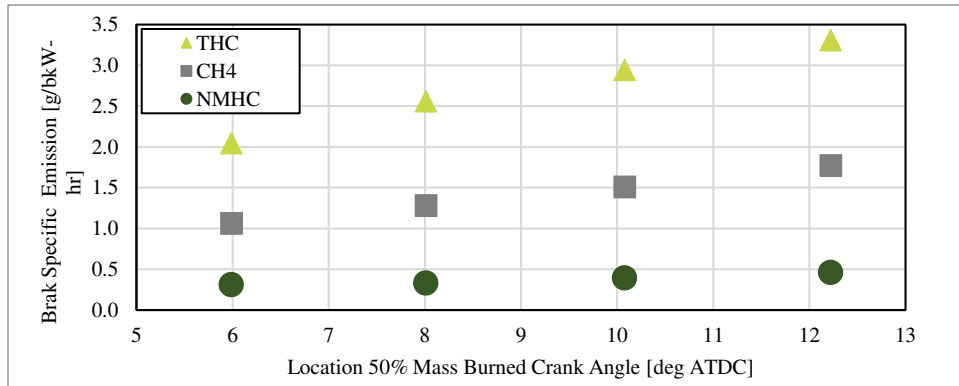


Figure 59. Location 50% Mass Burned Crank Angle vs. Brake-specific Emission of THC, NMHC, and NMNEHC for piston B. Engine operating conditions: EGR 30% 1200 RPM, $\varphi = 1$, IMP 2.2 bar, CR 13.3:1.

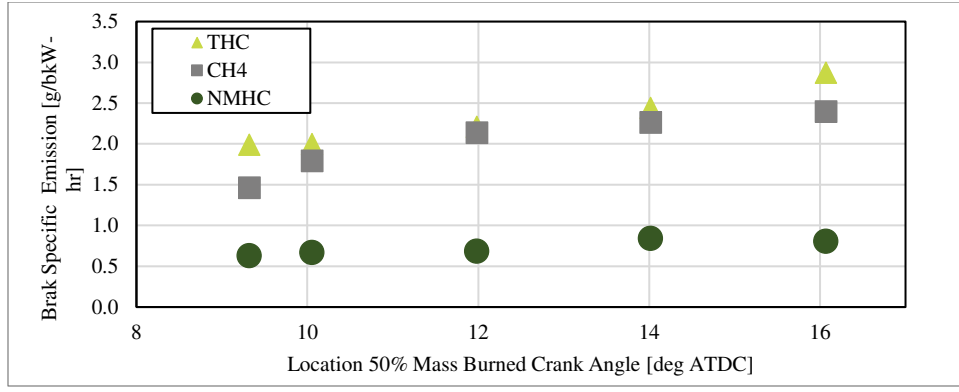


Figure 60. Location 50% Mass Burned Crank Angle vs. Brake-specific Emission of THC, NMHC and NMNEHC for piston C.

Engine operating conditions: EGR 30% 1200 RPM, $\varphi = 1$, IMP 1.8 bar, CR 15:1.

Carbon Monoxide

CO was also measured and normalized, as shown in Figure 61 and Figure 62 for pistons B and C respectively. CO emissions indicate a loss in chemical energy, as CO chemistry is primarily dominated by the equivalence ratio and fuel oxidation extent. In general, CO decreases as early CA50 is used, which is the case for the highest EGR cases tested, 25 and 30%. The 20% EGR case tends to hold the same trend without being linearly related to the efficiency increments associated with advanced timing. Still, the lower EGR case has an almost constant behavior. Slightly higher CO values were measured as more EGR was used, always within a range of 0.8 g/bkW-hr variations.

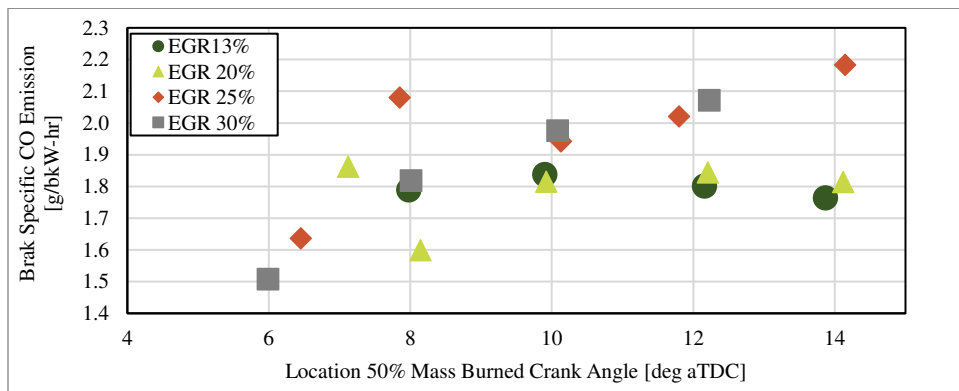


Figure 61. Location 50% Mass Burned Crank Angle vs. Brake-specific CO Emission for all EGR rates for piston B. Engine

operating conditions: 1200 RPM, $\varphi = 1$, IMP 2.2 bar, CR 13.3:1.

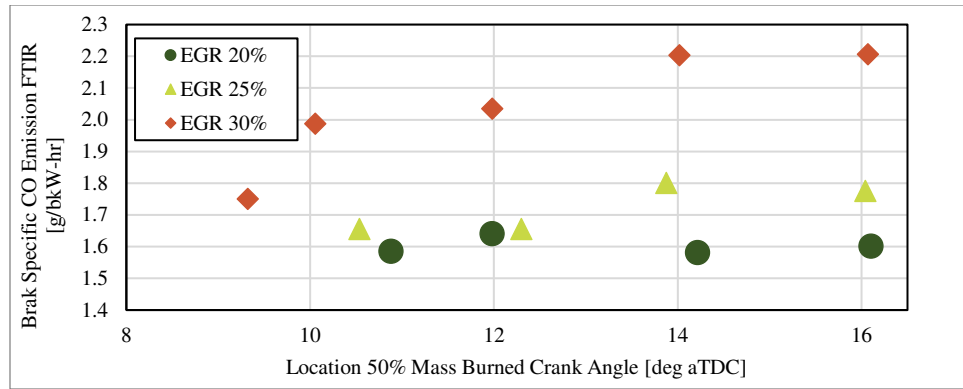


Figure 62. Location 50% Mass Burned Crank Angle vs. Brake-specific CO Emission for all EGR rates for piston C. Engine operating conditions: 1200 RPM, $\phi = 1$, IMP 1.8 bar, CR 15:1.

Volatile Organic Compounds

The FTIR spectrometer also measured non-methane, non-ethane hydrocarbons (NMNEHC), and Volatile Organic Compounds (VOC). Measurements of normalized VOC are shown in Figure 63 and Figure 64 as a function of BTE for piston B and C respectively. The trend indicates that early CA50 (i.e., High BTE) results in lower VOC emissions, indicating complete combustion. In the same way, a higher EGR rate produces higher VOC emissions. This is like the behavior of THC emissions. A minor increase in VOC emissions is observed when more exhaust gases are recirculated. In all cases tested, the measurement is below 1g/bkW-hr,

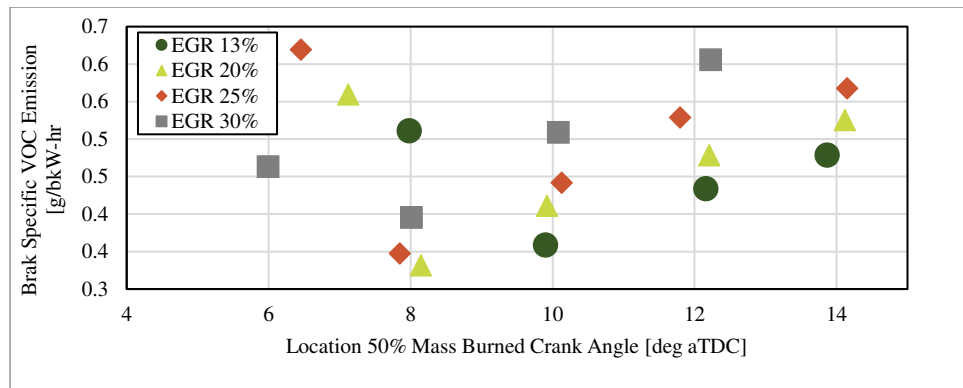


Figure 63. Location 50% Mass Burned Crank Angle vs Brake-specific VOC Emission for all EGR rates. Engine operating conditions: 1200 RPM, $\phi = 1$, IMP 2.2 bar, CR 13.3:1.

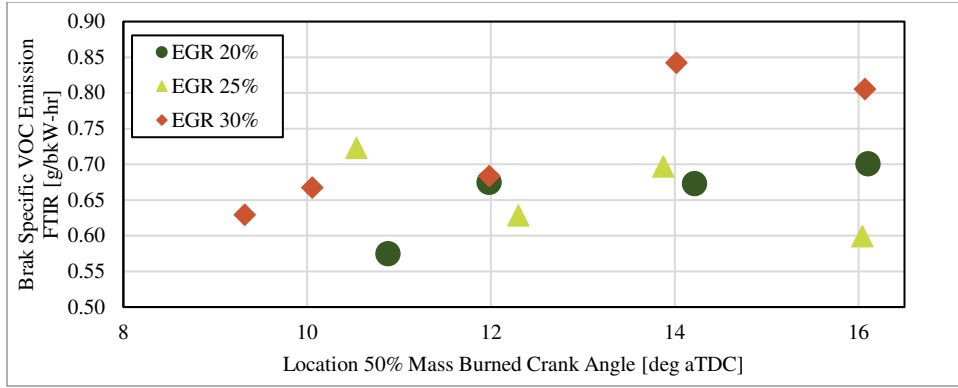


Figure 64. Location 50% Mass Burned Crank Angle vs Brake-specific VOC Emission for all EGR rates. Engine operating conditions: 1200 RPM, $\varphi = 1$, IMP 1.8 bar, CR 15:1.

Exhaust Gas Temperature

A critical aspect of this research is to correlate the test results with real work application scenarios. Concerning this, the Exhaust Gas Temperatures (EGT) were desired to be below 700°C to avoid using expensive materials in the turbocharger and exhaust manifold components. Figure 65 and Figure 66 show the EGT piston B y C respectively, showing linear behavior for constant EGR cases, and with the expected trend of decreased temperature as earlier CA50 is targeted. In the same way, higher EGR rates dilute the mixture coming into the engine, lowering in-cylinder temperatures, then reaching lower EGTs [31]. It is also important to note that for piston C, the temperatures are lower than piston B as higher BTE was achieved. Cases with similar BTE, like EGR 25% CA50 6.5 deg ATDC for piston B and EGR 20% CA50 12 deg ATDC for piston C, have close EGT of 579 and 574 deg C respectively (BTE for these cases are 45.7% piston B and 45.1% piston C).

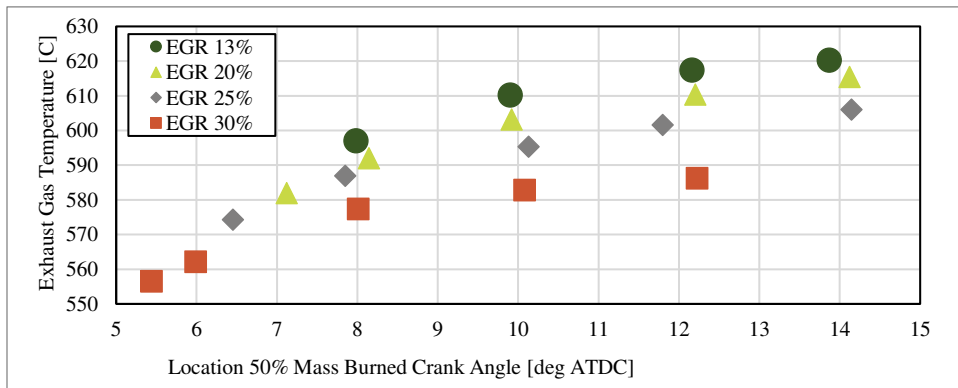


Figure 65. Location 50% Mass Burned Crank Angle vs. Exhaust Gas Temperature for all EGR rates. Engine operating conditions: 1200 RPM, $\varphi = 1$, IMP 2.2 bar, CR 13.3:1.

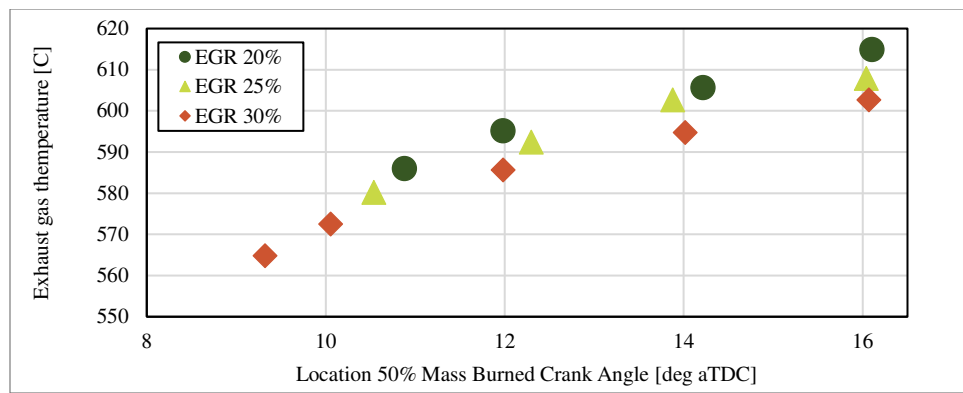


Figure 66. Location 50% Mass Burned Crank Angle vs. Exhaust Gas Temperature for all EGR rates. Engine operating conditions: 1200 RPM, $\varphi = 1$, IMP 1.8 bar, CR 15:1.

Chapter 5 – Practical Application of Controlled End-Gas Autoignition

Low-cost in-cylinder pressure sensors

The work presented in Chapters 2 to 3 of this document was developed using high-resolution in-cylinder pressure transducers. This type of sensor is the industry and academic standard to record and analyze pressure data inside a combustion chamber for internal combustion engines for research purposes. The capabilities of this technique are widely explained and proved [32], allowing an excellent understanding of the behavior of the combustion process inside the combustion chamber and providing data used to estimate metrics like knock index, heat release, and combustion variability, among others. Meanwhile, using high-accuracy pressure transducers involves high economic expense for the sensors, cables, and amplifiers required, and the reliability of the sensors is acceptable for laboratory and experimental use but not feasible for commercial applications [33].

The automotive and industrial engine commercial sector has developed low-cost in-cylinder pressure sensors to allow some of the benefits of real-time pressure monitoring while the accuracy and sampling rate is reduced. These commercially available sensors are used mainly on compression-ignited and high-power density industrial engines to define knock limit conditions. Additionally, some alternative mid-price range sensors are coming to the market to provide the benefits of real-time in-cylinder pressure monitoring while keeping the cost within the range of what is commercially viable.

This chapter compares two alternative sensors tested back-to-back against the high-resolution pressure transducer used for the primary research experiments of this work.

Sensors:

The alternative low-cost sensors tested are presented in Table 6 and Figure 67-Figure 69.

Table 6. Technical specifications of the in-cylinder pressure sensors tested.

Sensor	QC34C	IMES CPS-03	CAT GP-4435682
Make	AVL	IMES	Bosch
Range [bar]	0-250	0-300	0-200
Voltage[v]	Amplifier needed	18-32	12
Output	0-5	4-20 ma	0-5V
Cooling	yes	no	no

Price range [USD]	3000-5000 (sensor only)	1000-1500	80-200
Cut off frequency [kHz]	NA	10	>20
Resonance [kHz]	≈69	10	>20
Linearity	-0.02	0.01	0.01
Sensitivity	19 pC/bar	53.33 mA/bar	4 pC/bar



Figure 67 AVL QC34C sensor¹.



Figure 68 IMES CPS-03 sensor².



Figure 69 CAT GP-4435682 sensor.

The installation of the sensors required the fabrication of special adapters to use the two machined locations for sensors/injectors in the engine head. As each sensor did not share any standard or similarities in the mounting style; one adapter was fabricated to be installed in the location of a direct injector. Sensor and sensor adaptor hardware is shown in Figure 70.

¹ Imagen taken from AVL product brochure document “avl pressure sensor QC34C_Rev04.pdf”

² Image taken from <https://www.imes.de/htt-04.html#&gid=null&pid=4> 7/13/2023.



Figure 70. Sensors tested and adapters. From left to right: adapter for IMES sensor in original in-cylinder pressure location, adapter IMES sensor in DI location, Adapter CAT sensor on DI location, CAT sensor, IMES sensor amplifier, and sensor body.

One location is the original AVL sensor machined port, which uses the AVL AS02 adapter to install the sensor in the engine. The second location is the direct injector port. This secondary location allowed testing of sensors in parallel with the AVL sensor. This provided the capability to record data in parallel for two sensors over the same combustion cycles, making an ideal comparative scenario. The location of these ports in the cylinder head is presented in Figure 71 and Figure 72.

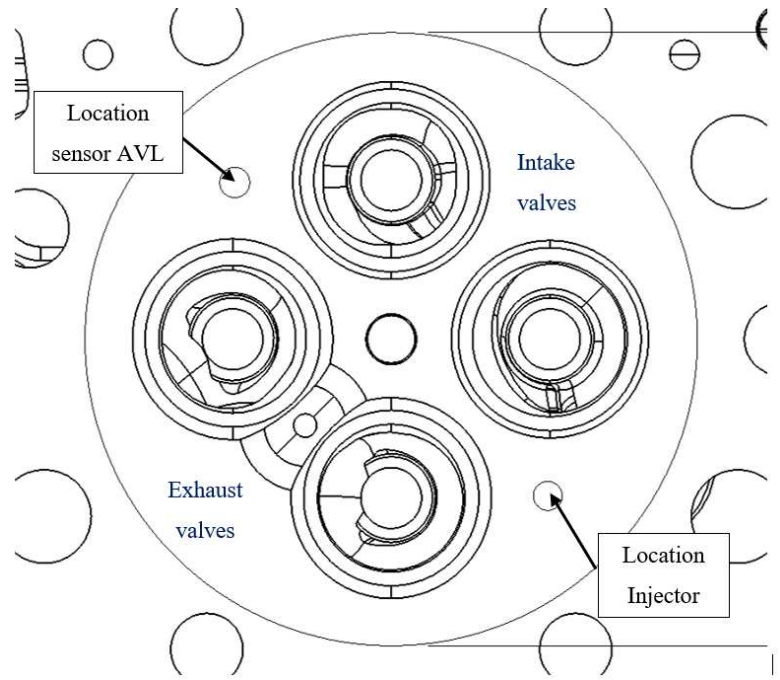


Figure 71 Location of AVL in-cylinder pressure sensor and direct injector. Head view from the combustion chamber side. The circle denotes the piston diameter.

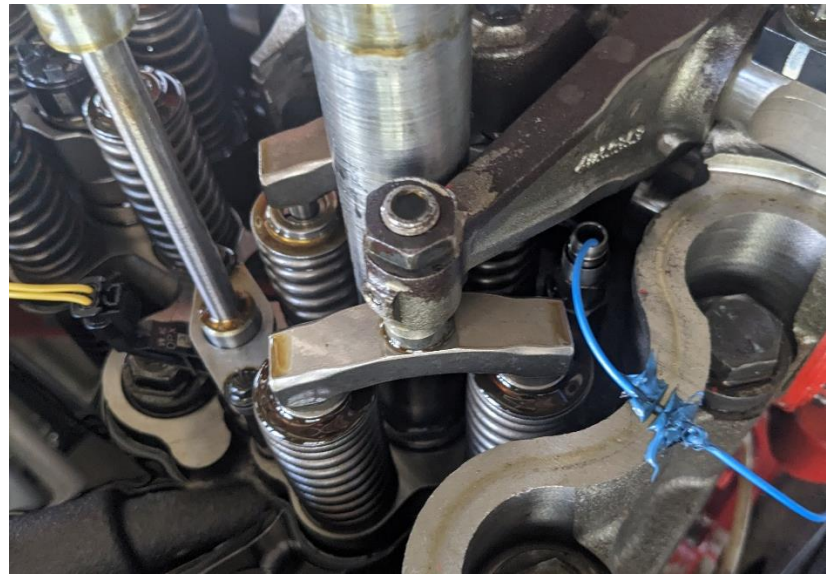


Figure 72. X15 SCE head. AVL and direct injector location.

The test was carried out using a 9.3:1 compression ratio piston. This compression ratio was used due to test cell availability, scheduling with other projects already ongoing on the test cell, and taking advantage of the lower peak pressure, which allows moving the engine into knock without

risking peak pressure values above the maximum rating of the engine (200 bar). No EGR and standard pipeline building supplied NG was used during the test.

The test established a desired load and speed on the engine, then performed timing sweeps to obtain different knock intensity metrics, using CA50 as the targeted variable to control the timing on the LECM. The LECM initially receives the signal from the AVL sensor to define the most accurate transducer baseline for the evaluated conditions. Then the pressure signal for the LECM is switched to the low-cost sensor to be tested. Both AVL and low-cost sensor signals are recorded in parallel on the combustion cart, and then the signals are post-processed.

The data acquisition system remained unmodified for this experiment; the only difference is using the signal amplifier for the AVL sensor (as required by design). The CAT and IMES sensors provide a signal directly connected to the LECM and the NI data acquisition system. The sampling rate is controlled by the 7200 pulses per cycle encoder. The signals getting into the LECM use the same filtration system, a Dataforth SCM7B41 in-line filter [34]. The LECM was updated with the correct voltage vs. pressure calibration value for the corresponding sensor as needed.

The operating conditions for this testing are presented in Table 7.

Table 7. Operative conditions for low-cost sensor test

Parameter	Value
CR	9.3:1
Eng. Spd [rpm]	900
IMEP [bar]	13.4-13.7
CIM [%]	20
EGR [%]	0
Coolant Temp	85
Intake Manifold Temp	45
Intake Manifold Pressure	1.6 – 1.65
Exhaust Manifold Pressure	1.7

Comparison of IMEP values for all three sensors is presented in Figure 73. Overall, the CAT sensor IMEP values are close to the AVL sensor values, within $\pm 3\%$. The CAT sensor IMEP is below the AVL sensor at early CA50 values and above the AVL sensor at late CA50 values. For the IMES sensor, the IMEP values closely align with the AVL reference, with deviations of within $\pm 5\%$ for

late CA50 values, and within $\pm 2\%$ for early CA50 values. During the testing process, an adjustment of the sensor calibration value was necessary to increase the accuracy of the measurements with this IMES sensor adjusting the signal gain within $\pm 5\%$ of the AVL values. The gain of the sensor was increased by 8% and an offset was applied to match the pegging pressure (pressure in the cylinder after the intake valve closes).

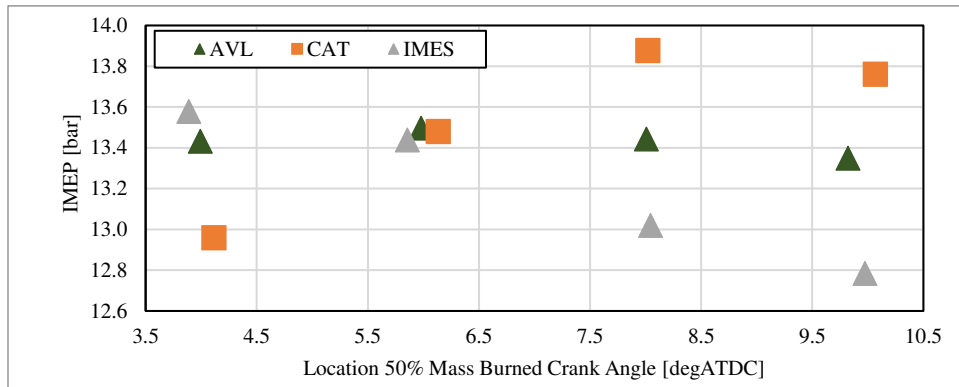


Figure 73. Location 50% Mass Burned Crank Angle [degATDC] vs. IMEP for AVL, CAT, and IMES sensor.

Figure 74 shows combustion pressure data for all three sensors at the same operating conditions. The pressure trace for the AVL shows no noise in the mean cycle, representative cycle, or shaded individual cycles. As explained in the results from the test carried out in Chapters 2 and 3, the data provided the most accurate description of the pressure behavior inside the combustion chamber. The low-cost sensors tested show clear evidence of high noise and some pressure trends that differ from the measurements of the AVL sensor. The CAT sensor shows the most significant disparity between the measured cycles in the compression and expansion zones, hence the higher IMEP discrepancy. A second characteristic is the “hump” or “shoulder” of the pressure trace at the top of the combustion zone between 2 and 8 degATDC. While for the AVL sensor, the transition from pressure increase towards the peak cylinder pressure is smooth, the CAT sensor reacts abruptly. This is explained as the sensor's natural frequency is considerably lower, and the sensor doesn't detect abrupt changes in pressure [35]. The last aspect to note from the CAT sensor is the measured noise and discrepancy in peak cylinder pressure. A high zone is detected from 0 to 10 degATDC. This creates a false reading in peak cylinder pressure and relates to the behavior explained previously for the lack of accuracy following the pressure variation.

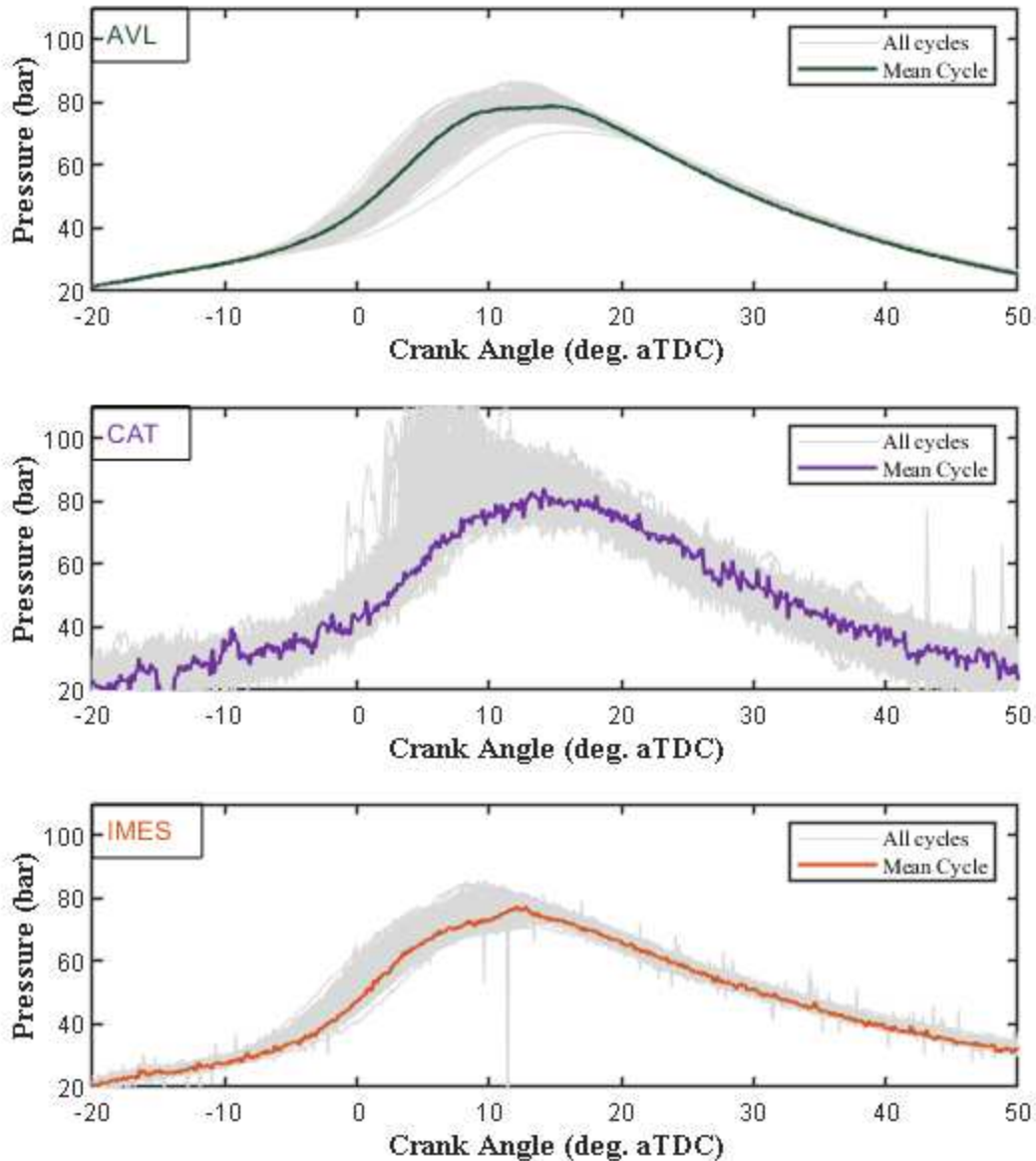


Figure 74 Crank angle vs. Pressure for AVL(top), CAT(middle), and IMES(bottom)sensor.

The performance of the two low-cost sensors tested suggests that a calibration process performed in an engine that includes the operation close or encountering C-EGAI could be incorporated for use in commercial applications, and they could be used to keep the engine within safe operative conditions and enhance BTE and load. The integration of the controller, filtration scheme of the signal, and the sensor will be vital to understanding each sensor's potential applicability.

The knock index (KI) estimated from the LECM was used to evaluate sensor knock prediction under the same operating conditions. These results are presented in Figure 75.

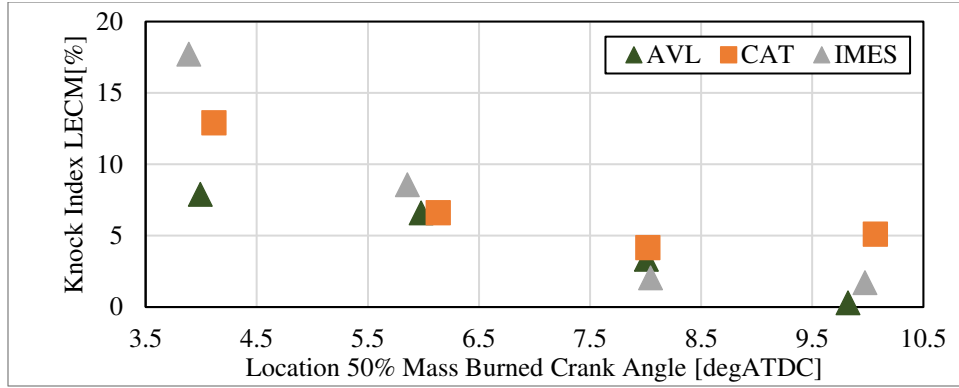


Figure 75. Knock index LECM vs. location 50% mass burned crank angle.

The KI from both low-cost sensors increased as the engine was pushed into the autoignition zone with earlier CA50 ignition targets. The CAT sensor tends to read closer to the AVL reference sensor while incurring errors of up to 50% regarding KI magnitude. The error is more significant for the IMES sensor as larger KI values are measured by the AVL sensor, overestimating the metric. The knock quantification is highly dependent on the technique, parameters defined by the user, and hardware characteristics. No sensor-specific tuning was performed when switching from one sensor to another; hence the software filtering and calibration constants for the KI metric could be improved for each sensor [36]. The key finding is that low-cost sensors exhibit a consistent KI trend, mirroring the high-accuracy AVL sensor. This alignment can be leveraged to improve engine performance. [37].

Figure 76 shows trends in BTE. The BTE is directly coupled with the indicated work produced by the engine, which is proportional to IMEP, and the fuel consumption. As the test was performed under equal conditions, the behavior of the BTE is only affected by the IMEP calculated from the pressure traces. Hence, the trends for the Cat and IMES sensors are like those displayed in the Figure 73. The variation of 0.04 fraction units on the BTE estimation for both sensors correlate with the inaccuracy to estimate the correct value of IMEP from the pressure trace. While the trend matches the AVL readings to estimate KI, it needs to be improved on the signal quality to obtain reliable IMEP estimations.

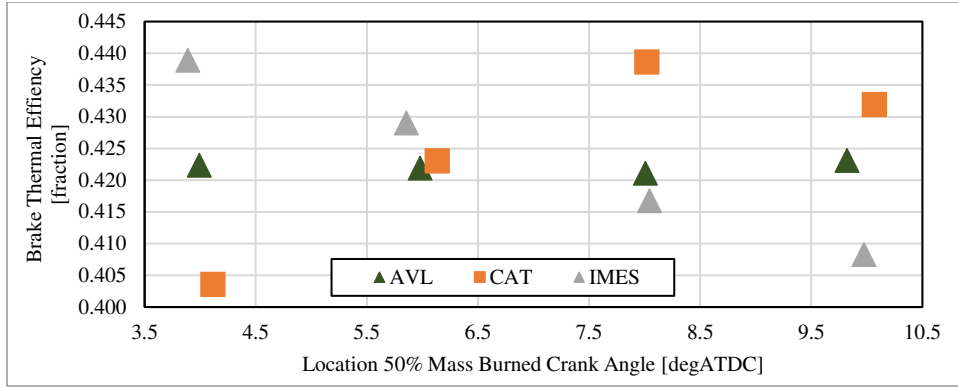


Figure 76. Location 50% Mass Burned Crank Angle [degATDC] vs. BTE for AVL, CAT, and IMES sensor.

Figure 77 and Figure 78 display results for COV of IMEP and COV of PP, respectively. The behavior of the IMES sensor in the pressure trace closely resembles that of the CAT sensor. Overall, the IMES sensor contains more noise on the signal than the CAT sensor, but the COV IMEP values are much closer to the AVL values. The pressure reading in the expansion zone is more accurate and shows less variability than the CAT sensor. A significant discrepancy in the IMES sensor data near the end of compression and the first stage of combustion. This corresponds to the location where the spark-plug fires (12 degBTDC), which appears to induce noise in the measured pressure signal. It is believed that this noise is the consequence of the narrow pathway for spark plug wire routing and resulting wire contact with engine head. The author did not have the opportunity to test other configurations to isolate the sensor wire and amplifier unit. It is expected that isolating the amplifier from some of the electrical noise of the engine would improve this behavior.

The CAT sensor produced COV values above the defined experimental limits (6 and 14 % for COV IMEP and COV PP, respectively) while offering good IMEP and BTE quantification compared to the AVL standard sensor. The increased noise in the signal explains this tendency and is likely due to the simplicity of the design. The IMES sensor had COV values within the range of what is considered acceptable (2 and 4% for COV IMEP and COV PP, respectively) due to a lower amplitude in signal noise and less cycle-by-cycle variation of the pressure trace during compression and expansion.

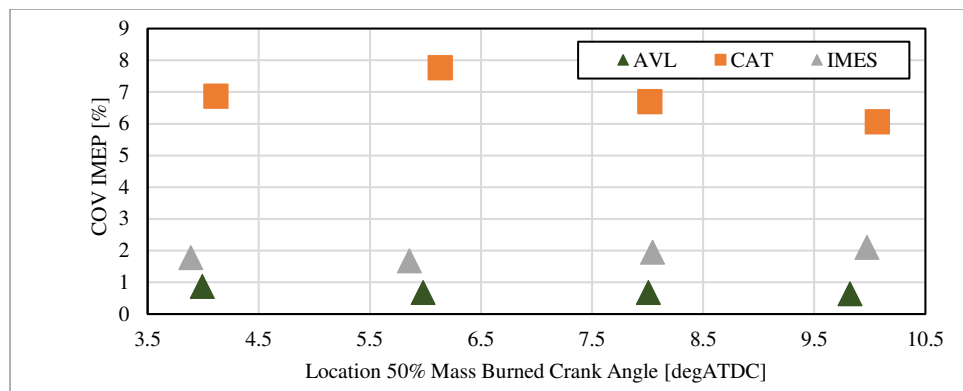


Figure 77. Location 50% Mass Burned Crank Angle [degATDC] vs COV IMEP for AVL, CAT and IMES sensor.

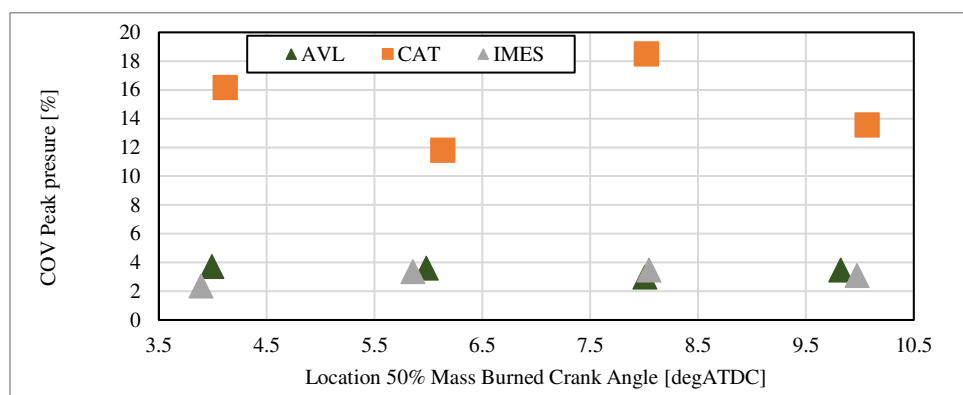


Figure 78. Location 50% Mass Burned Crank Angle [degATDC] vs. COV peak pressure for AVL, CAT, and IMES sensor.

Effect of fuel composition on engine combustion control

To analyze the stability of the combustion control provided by the LECM using high-accuracy in-cylinder pressure sensors, a series of tests were performed on the engine blending C3H8 into the stream of NG to the engine. The test performed analyzes the variation of the ignition variable defined on the LECM when the composition of the fuel is changed. At the same time, the engine is operated under conditions of EGAI. The general parameters of the test are presented in Table 8. Engine operative conditions for the effect of fuel composition test. Table 8.

Table 8. Engine operative conditions for the effect of fuel composition test.

Parameter	Value
CR	9.3:1
Eng. Spd [rpm]	1200
IMEP [bar]	14
CIM [%]	21
EGR [%]	30
Coolant Temp	85
Intake Manifold Temp	45
Intake Manifold Pressure	1.5 – 1.7
Exhaust Manifold Pressure	1.6 – 1.8

While operating the engine under constant load and speed with 100% NG, a flow of C3H8 was introduced in the fuel blending system (Figure 13, presented earlier). The substitution decreased the methane number from 74.9 to 52 [29] in the first test. Fuel compositions from the GC gas analyzer are presented in Table 9.

Table 9. Fuel composition of NG and NG+C3H8 mix.

Species	NG	NG + C3H8
CH4 [%]	85.2	75
C2H6 [%]	0.104	0.91
C3H8 [%]	0.019	22.64
C4H10 [%]	0.0039	0.34
C5H12 [%]	0.001	0.1
C6H14 [%]	0.0002	0.01
N2 [%]	0.0036	0.2
CO2 [%]	0.0169	0.8
MN	74.9	52

The test results were summarized in terms of the variation of the ignition control variable. Each condition was repeated six times, with variations of load on the engine between each fuel blending exercise to ensure no remaining C3H8 added was in the fuel lines, and the same operating conditions were kept for the next test. For this test, the CIM metric was used as the variable to control the ignition timing on the engine, described in Chapter 1.

The variation in the CIM is presented for the addition of approximately 22% C3H8 and a decrease in the methane number to 52. The LECM combustion controller adjusts the spark timing to compensate for the changing characteristics of the pressure trace behavior. The calculated CIM target is 21. Figure 79 shows at an increase in average CIM of about 5% at about 200 cycles, corresponding to C3H3 addition. The controller takes about 100 cycles to return to the pre-injection average of 21. The spark timing data shows how the controller retards ignition timing by 2 deg to compensate for the increase in mixture reactivity associated with the addition of C3H8.,

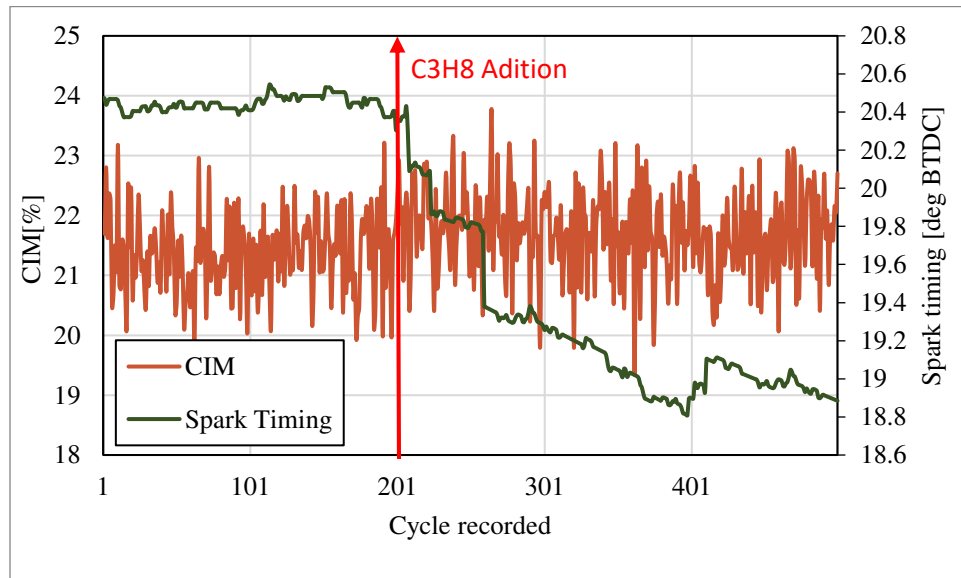


Figure 79. CIM and Spark timing behavior for the addition of 20% C3H8.

Defining the effectiveness of the control strategies for combustion stability requires more than one test. To better compare, the results from six fuel blending tests (78% NG 22% C3H8) are presented in Table 10.

Table 10. Fuel blending control trends summary.

Test	CIM variation	Stabilization [cycles]	ST change [degBTDC]
1	6.1	125	2.38
2	5.8	135	2.10
3	5.7	120	2.48
4	5.75	134	2.44
5	5.8	130	2.59
6	4.3	129	2.03

Stabilization of the CIM was defined as the number of cycles the controller needed to achieve the same average CIM reading on a set of 50 cycles, with a margin of $\pm 3\%$. CIM variation indicates the maximum registered change in the metric while the engine experiences the effect of different fuel quality. ST change is defined as the average number of degrees spark retard required for stabilization. The results indicate a close correlation between the change of ST for all the tests performed. An average of 2.3 deg of ignition delay compensates for the presence of propane in the fuel blend. The stabilization of the CIM metric takes, on average, 128 cycles. This amount of cycles is six times greater than the interpolation window of the ignition controller. This suggests that the controller performed as intended, adjusting the ignition timing within safe interpolation cycles in response to the change in fuel reactivity. A related consideration is that the change in fuel quality should not be expected to be instantaneous, as the response of the blending system is limited to mix and homogenize the NG with the C3H8. The peak-to-peak variation in CIM was below 6%, which is a relatively low number, considering that the engine is recommended (based on the calibration of the LECM control unit and the previous experiments performed with this engine) to be operated under conditions of CIM 40%, hence the CIM metric was always within the desired ranges. These results demonstrate that the controller performed adequately to keep the engine running under the requested CIM and without experiencing uncontrollable knock conditions for an increase in fuel reactivity.

GT-Power Modeling

GT-Power is software developed for engine performance simulation by Gamma Technologies. It is recognized as the industry-leading tool capable of predicting power, torque, airflow, volumetric efficiency, fuel consumption, turbocharger performance, etc., by solving the unsteady 1-D Navier-Stokes equations. It also contains several sub models, such as combustion, friction, heat transfer, etc.

The Three Pressure Analysis (TPA) and the Spark-Ignition Turbulent Flame models are the sub-models used in this work to develop a model of the 6-cylinder X15 engine based on the experimental results and GT-Power SCE model developed by Bestel [38]. The GT-Power model for the engine is shown in Figure 80. [39].

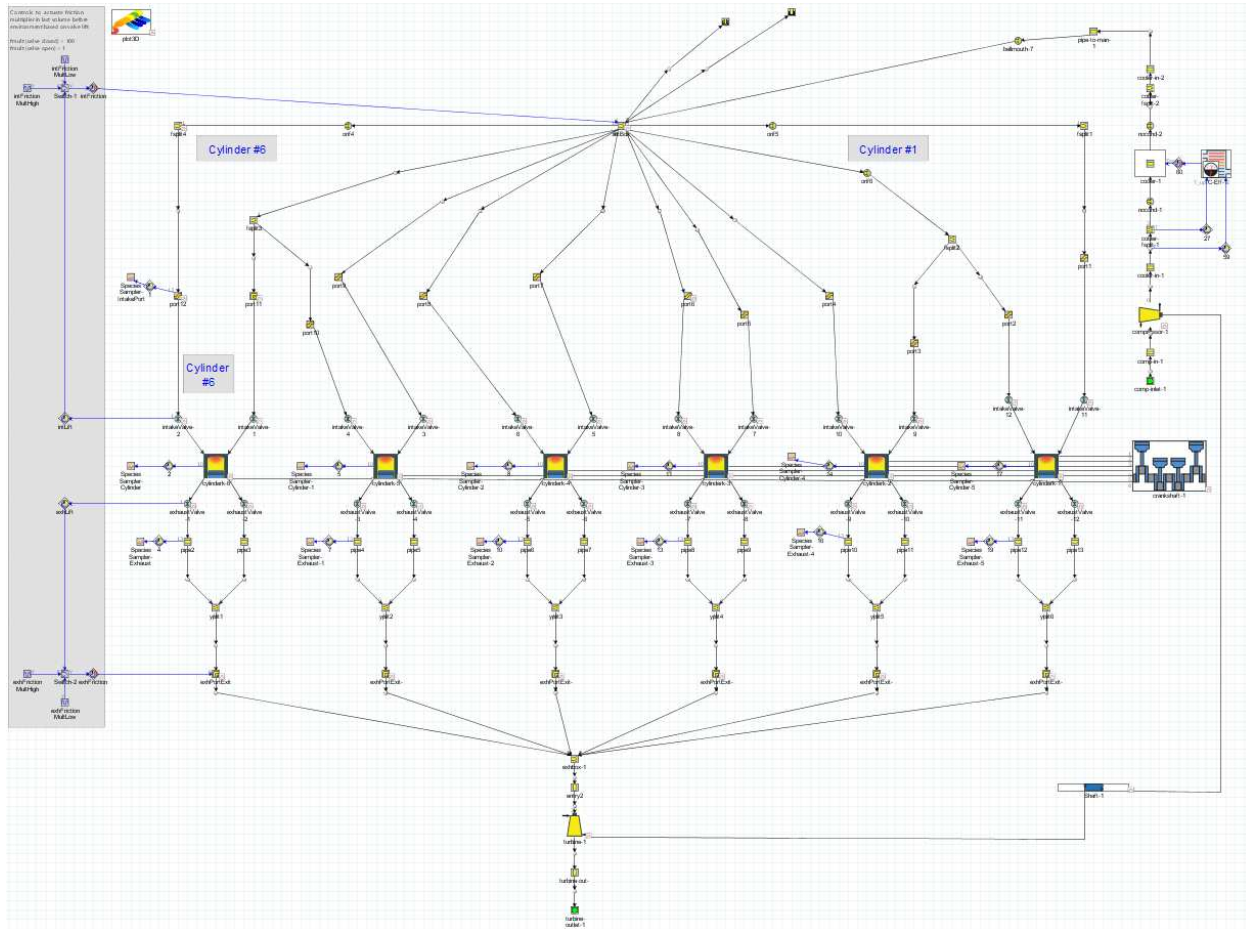


Figure 80 GT-Power model for six-cylinder X15 NG engine.

TPA modeling uses experimental data to calculate a crank-angle resolved burn rate that represents the combustion characteristics of the engine modeled. This modeling technique is used to define initial and boundary conditions for 3-D CFD models and experimental data evaluation, and it is the foundation for the predictive Spark-Ignition Turbulent Flame model.

Combustion phasing, BMEP, brake torque, and brake power are some of the performance parameters to be analyzed using a TPA model. The main required inputs are the three crank-angle resolved pressures, intake, exhaust, and in-cylinder pressures, while other relevant engine parameters such as EGR rate, spark timing, emissions, and fuel composition are also required. SI Turbulent Flame modeling is a predictive model that estimates the burn rate behavior. This modeling technique was developed from the work of Blizzard et al. [40], Hires et al. [41] and Morel et al. [42] and uses a fully calibrated TPA model to estimate volumetric efficiency, burn rate, and residual gas fraction. This type of model uses four main calibration factors:

- Dilution Effect Multiplier (C_{DE}): represents the effect of dilution on combustion performance.
- Turbulent Flame Speed Multiplier (C_{TFS}): estimates the effect of turbulence intensity on flame propagation.
- Taylor Length Scale Multiplier (C_{TLS}): represents the scale effect of laminar flame propagation over the combustion event.
- Flame Kernel Growth Multiplier (C_{FKG}): represents the initial growth rate of the flame kernel.

GT-Power has in its library a laminar flame speeds curve fitted to the equation developed by Metghalchi and Keck [43]. The flame speed correlation for this engine was produced by Bestel [39]. A detailed explanation of the working principles of SI turb modeling can be found in Bestel's work.

X15 6-Cylinder 1-D TPA Model

A 1-D Three-Pressure Analysis (TPA) model was created using GT-Power to simulate the X15 6-cylinder version of an engine based on the SCE experimental data and previous modeling carried out by Bestel [39]. This exercise aims to demonstrate the performance values expected for a full-

size engine in the six-cylinder configuration and define the main characteristics of the turbocharger system, aftercooling, and overall flows. In the same way, the model could indicate the expected overall thermal efficiency if each cylinder's combustion characteristics are kept around the same level as those demonstrated in the SCE experimentation and simulation exercises. The following is a brief overview of model characteristics:

- Intake, exhaust, and cylinder pressures are the primary input to the model, coupled with time-averaged intake and exhaust temperatures.
- The model does not contain a detailed 3-D solid model, while it still uses the geometry characteristics of the piston, cylinder, and valvetrain specifications from the SCE.
- Valve lift profiles and valve lash are kept from the last iteration of the SCE modeling, accounting for the ideal volumetric efficiency with respect to the SCE model.
- Cylinder walls, ports, and valve temperatures were calculated using the Cylinder Wall Temperature Solver. The Finite Element Cylinder Structure Geometry modules use the Woschni to perform these calculations.

Table 4 shows the natural gas fuel composition used in the SCE model calibration and 6-cylinder modeling. The range of engine operating conditions used in the model calibration is presented in Table 11.

Table 11. Experimental operative conditions used for TPA GT-Power model calibration.

Parameter	Min	Max
IMEP [bar]	15	20
CA50 [degATDC]	14	5
EGR rate [%]	13	30

The model was re-calibrated for the last data set obtained from the 13.3:1 CR piston. This piston was chosen as the reference for modeling the full-size engine due to the large amount of data, the enhanced operating range, and the high BTE achieved. Figure 81 presents measured and modeled pressure traces for the reference SCE case.

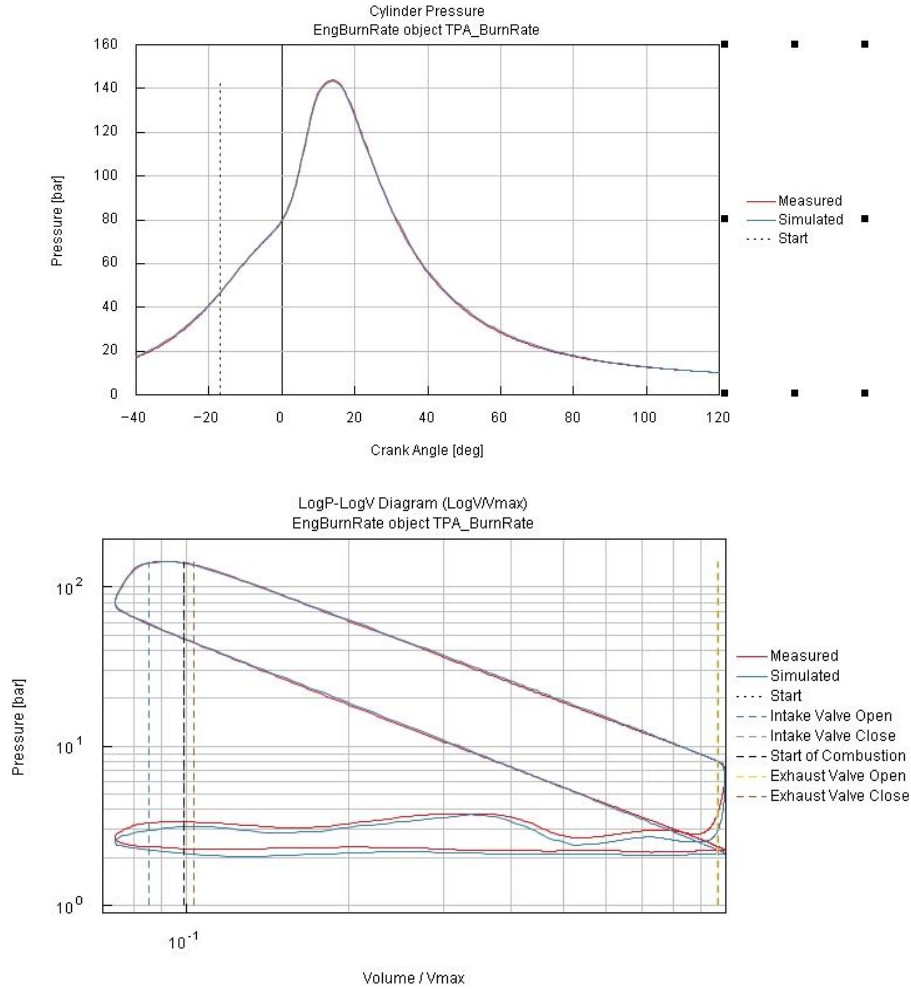


Figure 81 Upper: Pressure [bar] vs. Crank angle [deg]. Bottom: Pressure [bar] vs. volume [deg](log scale) for SCE simulation from GT-Power

The turbine and compressor were the main components intended to be scaled with this model. The initial SCE modeling in GT-Power and the subsequent testing developed on the SCE X15 engine test cell did not have a turbocharger; the intake air pressure was controlled independently from the exhaust pressure, both adjusted within ranges that were expected to be feasible for a real engine operative condition. A compressed air supply provides the intake air, and a butterfly-type valve controls the back pressure. From the GT-Power 6-cylinder model, the characteristic tables for the turbine and compressor are presented in the Table 12 and Table 13 respectively.

Table 12. Turbine characteristics

RPM	Flow [kg/s]	P-ratio	Isentropic Efficiency
1821.9	0.009	1.016667	0.68

1821.9	0.01	1.05	0.76
1821.9	0.010667	1.083333	0.79
1821.9	0.011633	1.121667	0.806
1821.9	0.011733	1.15	0.785
2225.1	0.011667	1.183333	0.74
2225.1	0.012333	1.225	0.76
2225.1	0.012667	1.266667	0.776
2225.1	0.013333	1.308333	0.784
2225.1	0.013667	1.35	0.778
2567.4	0.0135	1.383333	0.74
2567.4	0.013667	1.425	0.76
2567.4	0.014	1.466667	0.774
2567.4	0.014333	1.505833	0.78
2567.4	0.014667	1.541667	0.77
2863.6	0.014167	1.583333	0.74
2863.6	0.014333	1.625	0.76
2863.6	0.0145	1.666667	0.775
2863.6	0.014667	1.714167	0.781
2863.6	0.014833	1.75	0.77
3133.6	0.014833	1.808333	0.745
3133.6	0.015	1.883333	0.76
3133.6	0.015067	1.958333	0.776
3133.6	0.015133	2.035833	0.782
3133.6	0.0152	2.1	0.77

Table 13 Compressor characteristics.

RPM	Flow [kg/s]	P-ratio	Isentropic Efficiency
55984	0.0735	1.225	0.67
55984	0.103537	1.1921	0.737
55984	0.135681	1.1683	0.763
55984	0.163317	1.1256	0.735
55984	0.193452	1.0458	0.639
73974	0.1127	1.694	0.68
73974	0.152831	1.6674	0.74
73974	0.189679	1.6436	0.771
73974	0.224714	1.5575	0.745
73974	0.259014	1.3783	0.639
88485	0.1764	2.247	0.69
88485	0.215012	2.2337	0.746
88485	0.238581	2.2064	0.758
88485	0.267932	2.0741	0.731
88485	0.292775	1.7752	0.635
102000	0.2156	2.8154	0.7
102000	0.2548	2.8126	0.709
102000	0.267295	2.7769	0.712

102000	0.2842	2.6495	0.7
102000	0.309411	2.2561	0.631

The geometry specifics of the turbine compressor were not intended to be determined in this section. The GT-Power model adjusts the conditions in an iterative process to match each component's desired characteristic curve behavior.

The turbine and compressor were included once the model was expanded for 6-cylinders, including detailed intake and exhaust manifolds geometry. Using the base SCE combustion characteristics defined from the TPA analysis, the model simulates the combustion of six cylinders. The measured pressure for the modeled case is included as a reference in the plot to allow a quick indication of the accuracy of the simulation.

This simulation uses as a reference the best BTE case conditions, described as follows:

- Target IMEP 20 bar
- Avg PP 140 bar
- CA50 7.1 deg ATDC
- Lambda 1.0
- MAP 2.3 bar (after turbine)
- EGR rate 30%
- BTE 46%

GT-Power TPA results for the 6-cylinder model results are presented in Figure 82. The P-V diagram shows the different pressure profiles for the intake and exhaust strokes across the cylinders, a characteristic expected as the experimental data used corresponds to cylinder 6. The compression and combustion region of pressure traces show an acceptable agreement with experimental data. In Table 14 the peak variation across the 6 cylinders is presented for the main parameters of the simulation. Fuel flow rates match within 2% of experimental data, IMEP, and IMP within 5%, which results in a Brake Thermal Efficiency (BTE) agreement within 4.5% (0.022 fraction, 0.466 SCE vs 0.433 6-cylinder). The CA50 shows a variation between cylinders of 1.3% and is within two degATDC from the required ignition timing target.

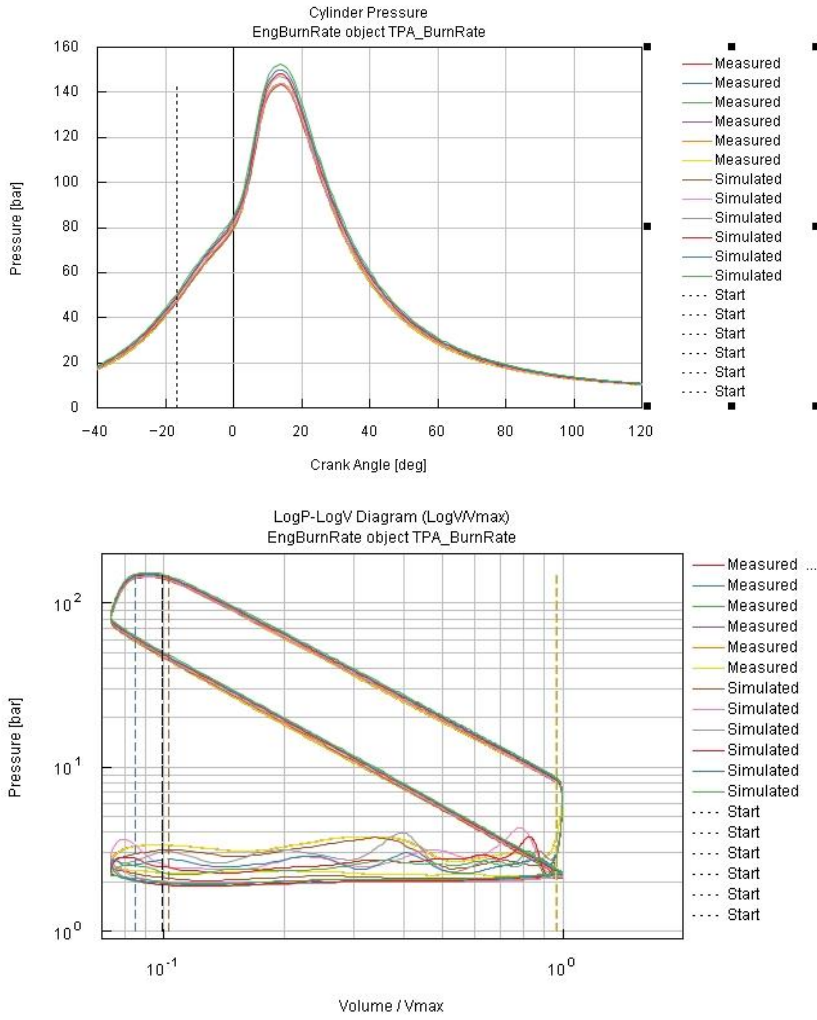


Figure 82. Upper: Pressure [bar] vs. Crank angle [deg]; Bottom: Pressure [bar] vs. volume [deg](log scale) for 6-cylinder engine simulation from GT-Power

Table 14. Cylinder variation of performance metrics

Parameter	Variation [%]
PP	5.0
IMEP	4.8
IMP	2.1
CA50	1.3
Fuel Flow	2.2
Estimated BTE	4.5

Figure 83 presents the variation of the volumetric efficiency for each cylinder on the 6-cylinder simulation with respect to the experimental SCE data and SCE simulation. The average loss on

Vol-Efficiency is 6% (0.09 fraction) can be attributed to the constraint of using only the experimental data of cylinder 6 to reference the simulation on cylinders 1 to 5. This variation within cylinders indicates the effectiveness of the intake and exhaust manifolds design and the adequate exchange of gases for each cylinder. The model uses an approximate geometry of the production diesel version of the Cummins ISX15 engine.

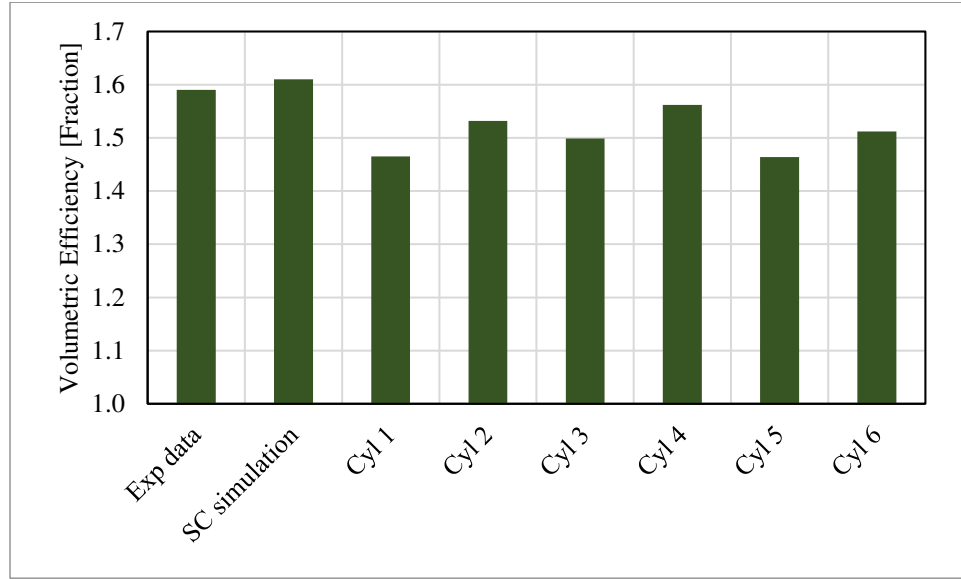


Figure 83. Volumetric efficiency from the 6-cylinder X15 engine simulation with respect to SC simulation and experimental data.

The variation in volumetric efficiency is directly correlated with the loss in brake thermal efficiency (BTE), while parameters such as fuel flow exhibit minimal variation among cylinders, and the location of CA50 is consistently low. Consequently, it can be concluded that the primary deviation between the single-cylinder engine (SCE) and the 6-cylinder simulation in terms of BTE can be attributed to limitations in the accuracy of volumetric efficiency measurement.

Table 15 presents the general performance results for the simulation of the 6-cylinder X15 NG engine. The simulation was performed at 1200 rpm, corresponding to the engine peak torque speed. This indicates that the primary comparison value with respect to the diesel counterpart of this platform should be made exclusively in terms of brake torque and BTE. The peak torque from the model is 6% less than the diesel lower spec (1851 vs. 1966 Nm) published for the “ISX15 SMARTADVANTAG POWERTRAIN - HD TRUCK” [44]. The BTE is 44.3% vs. 44%, with the highest value for the modeled NG engine. The lower IMEP of 19.32 bar indicates that the model

is not operating under the same load conditions with respect to the experimental data, as the reference data targets a 4% higher IMEP. This value corresponds to the decrease in BTE with respect to the SCE results. As one of the common challenges for NG vs. diesel engines is the overall performance, the results presented in this simulation suggest that the available peak torque could be sufficient for the NG engine [45]. This considers the limited scenario simulated where there is room for improvement in identifying the peak torque speed, optimization of the geometry of intake and exhaust manifolds, and increasing manifold pressure with further optimization of the turbocharger to increase the effective load.

Table 15. Performance results 6-cylinder simulation.

Parameter	Value
Brake Power [kW]	231.6
Brake Torque [Nm]	1851.8
IMEP [bar]	19.32
FMEP [bar]	0.75
PMEP [bar]	-3.23
BSFC [g/kWh]	167.9
Volumetric Efficiency [%]	141.9
Trapping Ratio	1
Lambda	0.99
Brake Efficiency [%]	44.3

Chapter 6 Conclusion\

This work developed a single-cylinder 2.5-liter heavy-duty research engine to conduct experiments at steady-state operating conditions, different EGR rates, and ignition timing targets. The test cell developed around this SCE can operate with natural gas and two other blended gases, simulate turbocharged conditions, and operate under advanced combustion control techniques based on in-cylinder pressure measurements.

Once the commissioning and baseline test was concluded, extensive testing was conducted on the innovative combustion control algorithms and CFD-optimized piston designs, allowing ultra-high efficiency and low emissions for NG ICE heavy-duty on-road applications. This experiment found improvements in BTE operating the engine with a higher EGR rate and early ignition control target.

The baseline testing demonstrated effective control of intake manifold pressure, exhaust manifold pressure, engine equivalence ratio, speed, torque, jacket water temperature, and oil temperature. The baseline testing shows reliable and consistent results for engine thermal efficiency, indicated mean effective pressure (IMEP), and coefficient of variance of the IMEP over a wide range of operating conditions. The baseline testing included operating conditions with load ranges from 15.5 to 16.4 bar IMEP at 1200 RPM, a best thermal efficiency of 39.9% at 10% EGR rate, and a CA50 value of 8 deg ATDC. The achieved BTE for this engine was expected for the baseline hardware configuration tested, with peak values 2% lower than similar heavy-duty NG engines while operating with a lower EGR rate. The knock limit for the engine was encountered at 6 deg ATDC CA50 for the cases with 15% and 20 EGR rates and 16.4 bar for 15% and 20% EGR. The capability to achieve over 30% EGR rates was demonstrated. The COV of IMEP was below 1% for all the test cases, while the COV of Peak Pressure was below 3.7% for all the cases tested, showing combustion stability lower than threshold values of 3% and 10%, respectively.

Three prototype pistons were tested, aiming for the extreme and medium scenarios from the CFD simulation, highest BTE and highest knock tendency, low knock tendency, and a medium case that suggested a good balance of BTE gain with relatively low knock tendency. The prototype named “A” had the highest CR (16.3:1), and hence the higher potential BTE gain suffered from uncontrollable knock and surface overheating due to limitations on the casting design used to create the prototype. This motivated the elimination of this prototype as a viable alternative. The

highest load condition achieved with this prototype was 14 bar IMEP with a 30% EGR substitution rate and achieving a BTE of 42.5%.

A second prototype piston “B” had a lower CR of 13.3:1 and a flat bowl with the minimum wall thickness between the cooling galleries and the combustion chamber surface. The CFD simulations suggested a low knock tendency and the requirement to operate the engine at a high load (18-20 bar IMEP) to achieve high efficiency. This prototype combustion stability was maintained using COV IMEP and PP, with values below 1.2% and 5%, respectively, for all conditions tested. C-EGAI was achieved for high-load engine conditions using advanced combustion controls with a high-accuracy in-cylinder sensor. Multiple test conditions achieved BTE values above the pre-defined target of 44%. The best BTE condition of 46% was found using an EGR rate of 29.4%. This condition was achieved with f-EGAI of 28.5% and CIM of 35%. The peak cylinder pressure was 144 bar. IMEP was 19.9 bar, and the estimated BP was 43.4 kW.

The third prototype piston “C” had a compression ratio of 15:1. This piston aimed to keep thin walls between the cooling galleries and the combustion chamber in the zones identified as critical to prevent excessive knock tendency. An open bowl design was used to enhance the propagation of the flame from the center of the combustion chamber to the cylinder walls. This piston was operated at lower loads (19.6-17.9 bar IMEP) as a reduced operating window was encountered due to the higher compression ratio. A high EGR substitution rate from 20 to 30% was necessary to keep the engine away from undesirable knock. The best BTE condition of 48.3% was found using an EGR rate of 30%. This condition was achieved with f-EGAI of 34% and CIM of 30%. The peak cylinder pressure was 138 bar. IMEP was 17.9 bar, and the estimated BP was 41.8 kW.

Exhaust emissions were measured during the engine testing for pistons B and C. The best BTE operating condition emission factors for piston B were 2.05, 1.51, 3.46, and 0.46 g/bkW-hr for CO, THC, NOx, and VOC, respectively. For piston C, the best BTE operating condition emission factors were 1.75, 3.5, 4.6, and 0.63 g/bkW-hr for CO, THC, NOx, and VOC, respectively. The higher emission factor of piston C can be attributed to both the lower load and the nearly identical measured concentrations of CH₄ and NMHC compared to piston B. This indicates similar combustion efficiency for both pistons. The final configuration of a stoichiometric, heavy-duty natural gas engine would likely incorporate a 3-way catalyst to achieve lower emissions and meet required limits. Exhaust gas temperature EGT were 562°C and 564°C for pistons B and C at the

best BTE condition, respectively, indicating the similarity in combustion characteristics for both experiments. The reference value used for the EGT was 700°C as the maximum allowable temperature on the exhaust manifold, a value above all the experiment results.

Two low-cost in-cylinder pressure sensors were tested to define the applicability of advanced combustion control techniques in commercial engines. An IMES sensor showed less accuracy in peak cylinder pressure measurement due to high noise in the signal. The average pressure trace values were acceptable, and the IMEP is comparable to the reference AVL sensor. When used to feed the combustion controller, a reduction in brake thermal efficiency (BTE) was observed at certain points, while improvements in other aspects were noted. On average, the values of BTE, PCP and IMEP for all conditions tested remained within 5% of those achieved with the AVL sensor. However, it's worth noting that the sensor's performance could be enhanced by implementing a dedicated filtration scheme to reduce signal noise before acquisition by the combustion controller on the LECM. The second sensor tested was a CAT GP-4435682, presenting overall COV values above the defined experimental limits (6 and 14 % for COV IMEP and COV PP, respectively) while offering good IMEP and BTE matching with respect to the AVL standard sensor. The increased noise in the signal can be explained based on the simplicity of the design. This sensor showed a less accurate pressure trace than the AVL sensor, especially in the fastest slope changes.

The performance of the two sensors tested suggests that a calibration process performed in an engine that includes the operation close or within C-EGAI could be used for commercial applications with these types of sensors that could keep the engine within safe operative conditions and enhance BTE and load. Matching between the controller, signal filtration scheme, and the sensor will be vital to understanding the sensor's applicability.

A test aimed to identify the combustion controller' reaction limitation to fuel composition variations was carried out on the SCE. This test showed that the engine was safely controlled by the LECM at high loads while changing the fuel composition. The first case, A, studied included a change in fuel composition by adding propane to the fuel blending system, changing the methane number from 71 to 54. A second experiment, case B, was performed where half of the mass flow of NG was replaced by propane. In both experiments, the LECM kept the engine under control while running under the CIM control strategy. A performance loss was evident as the timing was

delayed preventing undesirable knock. BTE decreased by 2.3 % and 4% for cases A and B. This test shows the safety potential of advanced combustion control strategies, which guarantee safe operation at the expense of a performance loss.

A GT-Power model was developed to estimate the overall performance of the practical application of the SCE experimental results. This model uses the SCE model for piston design optimization as a foundation. Using empirical data and the TPA approach, a 6-cylinder model simulated the performance over the expected conditions of best BTE. The model was equipped with a turbocharger model, and an iterative process was used to define the requirements of the turbine and compressor in terms of speed, flow, compression ratio, and efficiency. From this model, a 6-cylinder version of the SCE NG engine is expected to produce 1851 Nm at 1200 rpm, 6% less than a diesel version of an engine for the same application and architecture. The BTE was 44.3% for the 6-cylinder NG model vs. 44% for the diesel engine. Overall performance of the modeled intake, exhaust manifolds, and turbocharger was acceptable, given the constraints expected when using components designed for a diesel engine application.

This study showcases the potential of natural gas (NG) engines as a viable alternative to traditional commercial diesel engines. NG engines offer the dual advantage of relatively low pollutant emissions and comparable, if not superior, thermal efficiency. Coupled with the cost-effectiveness of their components and maintenance, and the ready availability of NG as a domestically sourced fuel in the US, this makes them an excellent choice for addressing the short- and medium-term requirements of heavy-duty transportation powertrain solutions.

References

- [1] R. D. Reitz, "Directions in internal combustion engine research," *Combustion and Flame*, no. 160, pp. 1-8, 2013.
- [2] United Nations Framework Convention on Climate Change, "Paris Agreement," 2015.
- [3] S. R. Cooleya, B. Bellob, D. Bodanskyc, A. Mansellc, A. Merkld, N. Purvisc, S. Ruffoa, G. Taraskac, A. Ziviana and G. Leonarda, "Overlooked ocean strategies to address climate change," *Global Environmental Change*, 2019.
- [4] U. E. I. Administration, "International Energy Outlook 2021 (IEO2021) Reference Case," 6 June 2021. [Online]. Available: https://www.eia.gov/outlooks/ieo/pdf/IEO2021_ReleasePresentation.pdf. [Accessed 6 June 2022].
- [5] R. Mitchell and D. B. Olsen, "Extending Substitution Limits of a Diesel–Natural Gas Dual Fuel Engine," *Journal of Energy Resources Technology* 140, no. 052202, 2018.
- [6] NREL, "TRANSPORTATION ENERGY FUTURES SERIES: Alternative Fuel Infrastructure Expansion: Costs, Resources, Production Capacity, and Retail Availability for Low-Carbon Scenarios," NREL, 2013.
- [7] G. T. Kalghatgi, "Developments in internal combustion engines and implications for combustion science and future transport fuels," in *Proceedings of the Combustion Institute* 35, 2015.
- [8] P. Shukla, J. Skea, E. C. Buendia, V. Masson-Delmotte, H. Pörtner, D. Roberts, P. Zhai, R. Slade, S. Connors and R. V. Diemen, "Climate Change and Land: an IPCC special report on climate change, desertification, land degradation, sustainable land management, food security, and greenhouse gas fluxes in terrestrial ecosystems," International Panel on Climate Change, 2019.
- [9] S. Bayliff, A. Marchese, B. Windom and D. Olsen, "The Effect of EGR on Knock Suppression, Efficiency, and Emissions in a Stoichiometric, Spark Ignited, Natural Gas Engine," in *2019 WSSCI Fall Technical Meeting*, Albuquerque, New Mexico, 2019.
- [10] G. Kalghatgi, "The outlook for fuels for internal combustion engines," *International Journal of Engine Research* 15, no. 383-398, 2014.
- [11] J. Heywood, Internal Combustion Engine Fundamentals, New York: McGraw-Hill,, 1998.
- [12] A. T. Kirkpatrick, Internal Combustion Engines: Applied Thermosciences, Wiley, 2020.
- [13] J. Mohr, A. Zdanowicz, J. Tryner, K. Gustafson, J. Venegas, B. Windom, D. Olsen and A. Marchese, "Ignition, Flame Propagation, and End-Gas Autoignition Studies of Natural

Gas/EGR Blends in a Rapid Compression Machine," in *2019 WSSCI Fall Technical Meeting*, Albuquerque, New Mexico, 2019.

- [14] J. Mohr, "The Effect of Fuel Reactivity and Exhaust Gas Recirculation on Knock Propensity of Natural Gas," Colorado State University, Fort Collins , 2020.
- [15] Colorado State University, "EXPANDING THE KNOCK/EMISSIONS/MISFIRE LIMITS FOR THE REALIZATION OF ULTRA-LOW EMISSIONS, HIGH EFFICIENCY HEAVY DUTY NATURAL GAS ENGINES. Final technical report," Department of Energy, Energy Efficiency and Renewable Energy (DOE, EERE), 2021.
- [16] N. Fiorini, "And indirect in-cylinder pressure measurement technique based on the estimation of the mechanical strength acting on an engine head screw, development and assessment," in *73rd Conference of the Italian Thermal Machines Engineering Association (ATI 2018)*, Pisa, 2018.
- [17] Y. Luo, B. Maldonado, S. Liu, C. Solbrig, D. Adair and A. Stefanopoulou, "Portable In-Cylinder Pressure Measurement and Signal Processing System for Real-Time Combustion Analysis and Engine Control," *SAE*, no. 2641-9637, p. 10, 2020.
- [18] S. Bayliff, "Evaluation of controlled end gas auto ignition with exhaust gas recirculation in a stoichiometric, spark ignited, natural gas engine," Colorado State University, Fort Collins, CO, USA, 2020.
- [19] T. Fosudo, T. Kar, A. Marchese, B. Windom and D. B. Olsen, "The Impact of LPG Composition on Performance, Emissions, and Combustion Characteristics of a Pre-mixed Spark-Ignited CFR Engine," *SAE Technical Paper*, no. 2022-01-0476, 2022.
- [20] D. Bestel, J. Rodriguez, A. Marchese, D. Olsen and B. Windom, "Detection and Onset Determination of End-Gas Autoignition on Spark-Ignited Natural Gas Engines Based on the Apparent Heat Release Rate," *SAE Technical Paper*, no. 2022-01-0474, 2022.
- [21] S. Nair, G. Hampson and J. Carlson, "Controlled Multi-staged Combustion Strategy for Overcoming Load Limitations of Fuel Flexible Gas / Diesel Engines," in *New Engine Developments – Gas & Dual Fuel. CIMAC Congress*, Vancouver, 2019.
- [22] American Gas Association, "Orifice Metering of Natural Gas and Other Hydrocarbons," 1990.
- [23] Bronkhorst, "M15," 6 6 2023. [Online]. Available: <https://www.bronkhorst.com/en-us/products-en/liquid-flow/mini-cori-flow/m15/>.
- [24] S. Bayliff, B. Windom, A. Marchese, G. Hampson, J. Carlson, D. Chiera and D. Olsen, "CONTROLLED END GAS AUTO IGNITION WITH EXHAUST GAS RECIRCULATION ON A STOICHIOMETRIC, SPARK IGNITED, NATURAL GAS ENGINE," in *Proceedings of the ASME 2020 Internal Combustion Fall Technical Conference*, 2020.

- [25] Woodward Inc. , "LECM Large Engine Control Module Product Manual 26757 (Revision NEW, 2/2015)," Woodward, 2015.
- [26] S. R. Turns and S. R. Turns, An Introduction To Combustion Concepts and Applications, McGraw Hill, 2012.
- [27] J. Rodriguez, H. Xu, G. Hampson, D. Bestel, B. Windom and D. Olsen, "Innovative Piston Design Performance for High-Efficiency Stoichiometric Heavy Duty Natural Gas Engine," *SAE technical paper*, no. 2688-3627, 2023.
- [28] Woodward Inc, "FTI-Family FAST TURBULENT IGNITER," [Online]. Available: <https://www.woodward.com/en/shop/woodward44-electronic-controls/fti-family>. [Accessed 6 6 2022].
- [29] MAN Energy Solutions, "Methane Number and Wobbe Index Calculator," MAN, [Online]. Available: <https://www.man-es.com/energy-storage/services/methane-number-calculator>. [Accessed 9 August 2022].
- [30] X. Yin, N. Sun, T. Sun, H. Shen, R. K. Mehra, J. Liu, Y. Wang, B. Yang and K. Zeng, "Experimental investigation the effects of spark discharge characteristics on the heavy-duty spark ignition natural gas engine at low load condition," *Energy*, vol. 239, 2022.
- [31] A. Y. Karnik and M. H. Shelby, "Effect of Exhaust Gas Temperature Limits on the Peak Power Performance of a Turbocharged Gasoline Engine," *Journal of Engineering for Gas Turbines and Power*, vol. 132, p. 11, 2010.
- [32] I. C. Trevas, W. R. N. R. B. S. Montemor, V. T. d. N. Neto and Charles Quirino Pimenta, "Knock Sensor Background Analysis and Their Relation with Combustion Pressure Curve," *SAE TECHNICAL PAPER SERIES*, no. 2016-36-0403, 2016.
- [33] J. Ängeby, A. Johnsson and K. Hellström, "Knock Detection Using Multiple Indicators and a Classification Approach," *IFAC PapersOnLine*, no. 297–302, pp. 31-51, 2018.
- [34] Dataforth.com, "dataforth.com/scm7b41-01d," [Online]. Available: https://www.dataforth.com/media/pdf/scm7b40_41.pdf. [Accessed 28 07 2023].
- [35] C. QUIRINO PIMENTA, I. TREVAS, V. TEIXEIRA, W. NAVEGANTES RODRIGUEZ, R. BEZERRA DE SOUZA MONTEMOR and L. RAMOS PUMPUTIS, "Knock sensor background analysis and their relation with combustion pressure curve," *SAE TECHNICAL*, no. 2016-36-0403, 2016.
- [36] S. Haertl, J. Kainz, H. Schuele, J. Beer and M. Gaderer, "Sensors, KNOCK Detection with Series Cylinder Pressure," *SAE*, no. 0148-7191, p. `11, 2020.
- [37] V. Ravaglioli, F. Ponti, M. De Cesare, F. Stola, F. Carra and E. Corti, "Combustion Indexes for Innovative Combustion Control," *SAE International*, no. 10.4271/2017-24-0079, 2017.

- [38] D. B. Bestel, "Modeling and Control of End-Gas Autoignition for the Realization of Ultra-Low Emissions, High-Efficiency Heavy-Duty Spark-Ignited Natural Gas Engines," Colorado State University, Fort Collins, 2022.
- [39] D. B. Bestel, ""Modeling and Parametric Study of End-Gas Autoignition to Allow the Realization of Ultra-Low Emissions, High-Efficiency Heavy-Duty Spark-Ignited Natural Gas Engines." PhD diss.," Colorado State University, Fort Collins, 2022.
- [40] N. Blizzard and J. Keck, "Experimental and theoretical investigation of turbulent burning model for internal combustion engines," *SAE Transactions*, pp. 846-864, 1974.
- [41] S. Hires, R. Tabaczynski and J. Novak, "The prediction of ignition delay and combustion intervals for a homogeneous charge, spark ignition engine," *SAE transactions*, pp. 1053-1067, 1978.
- [42] T. Morel, C. I. Rackmil, R. Keribar and M. J. Jennings, "Model for heat transfer and combustion in spark ignited engines and its comparison with experiments," *SAE transactions*, pp. 348-362, 1988.
- [43] M. Metghalchi and J. Keck, "Burning velocities of mixtures of air with methanol, iso-octane, and indolene at high pressure and temperature," *Combustion and flame*, pp. 191-210, 1982.
- [44] Cummins Inc, "ISX15 SMARTADVANTAGE™ POWERTRAIN - HD TRUCK," Cummins Inc;, [Online]. Available: <https://www.cummins.com/engines/isx15-smartadvantage-tm-powertrain-hd-truck>. [Accessed 24 7 2023].
- [45] J. Liu and C. E. Dumitrescu, "Limitations of natural gas lean burn spark ignition engines derived from compression ignition engines," *Journal of Energy Resources Technology*, vol. 140, no. 12, pp. 122308-1-9, 2020.
- [46] D. Bestel, B. Windom, D. Olsen, A. Marchese, S. Bayliff and H. Xu, "3-D Modeling of the CFR Engine for the Investigation of Knock on Natural Gas," in *2019 Fall Meeting of the Western States Section of The Combustion Institute*, Albuquerque, New Mexico, 2019.
- [47] J. F. Rodriguez, H. Xu, G. Hampson, B. Windom, A. Marchese and D. B. Olsen, "Heavy Duty Natural Gas Single Cylinder Research Engine Installation, Commissioning, and Baseline Testing," *Energy and Power Engineering*, p. 12, 2022.
- [48] C. Dumitrescu, P. V and J. Liu, "An experimental investigation of early flame development in an optical SI engine fueled with natural gas," *Journal of engineering for gas turbines and power*, p. 140: 082802, 2018.
- [49] A. Zdanowicz, "End-gas autoignition propensity and flame propagation rate measurements in laser-ignited rapid compression machine experiments," Colorado State University, Fort Collins , 2019.
- [50] Gamma Technologies, "Gt-power: User's manual and tutorial," Gamma Technologies;, 2018.

[51] M. S. Norton, "Uncertainty Analysis," [Online]. Available: <https://www.siue.edu/~mnorton/uncertainty.pdf>. [Accessed 17 8 2023].

[52] S. R. Cooleya, B. Bellob, D. Bodanskyc, A. Mansellc, A. Merkld, N. Purvisc, S. Ruffoa, G. Taraskac, A. Ziviana and G. H. Leonarda, "Overlooked ocean strategies to address climate change," *Global Environmental Change*, 2019.

Appendix

Detailed X15 SCE information



Figure Appendix - 1 Cummins X15 SCE intake system.

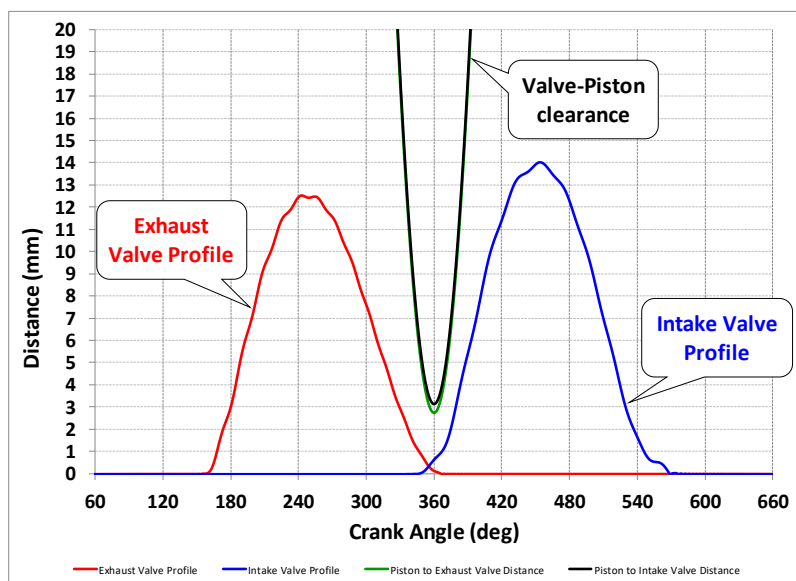


Figure Appendix - 2 Valve lift profile Cummins X15 SCE.

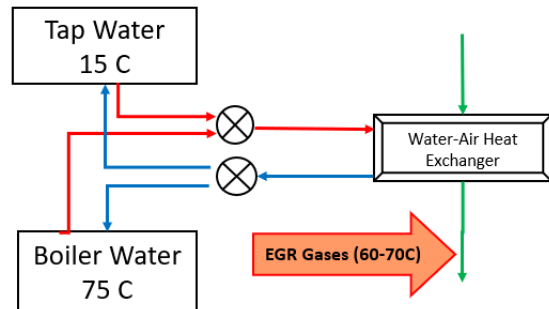


Figure Appendix - 3. Intake heat exchanger and schematic for Intake temperature control.



Figure Appendix - 4 Bosch MR3DII360 spark plug and spark plug insert as used during the baseline testing.

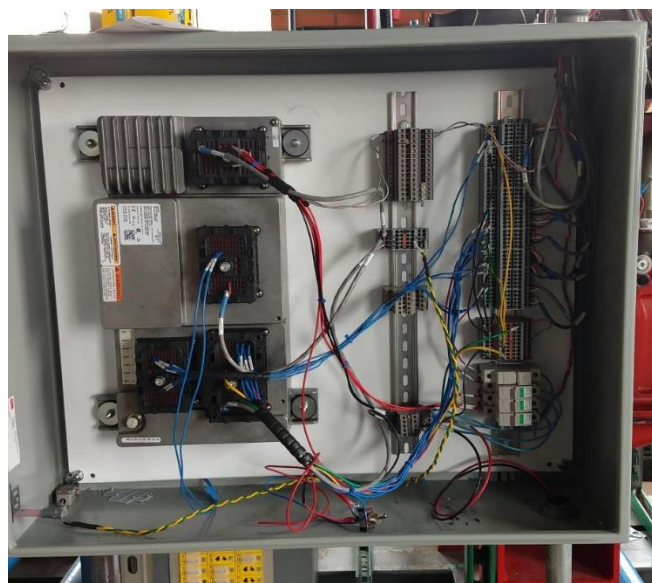
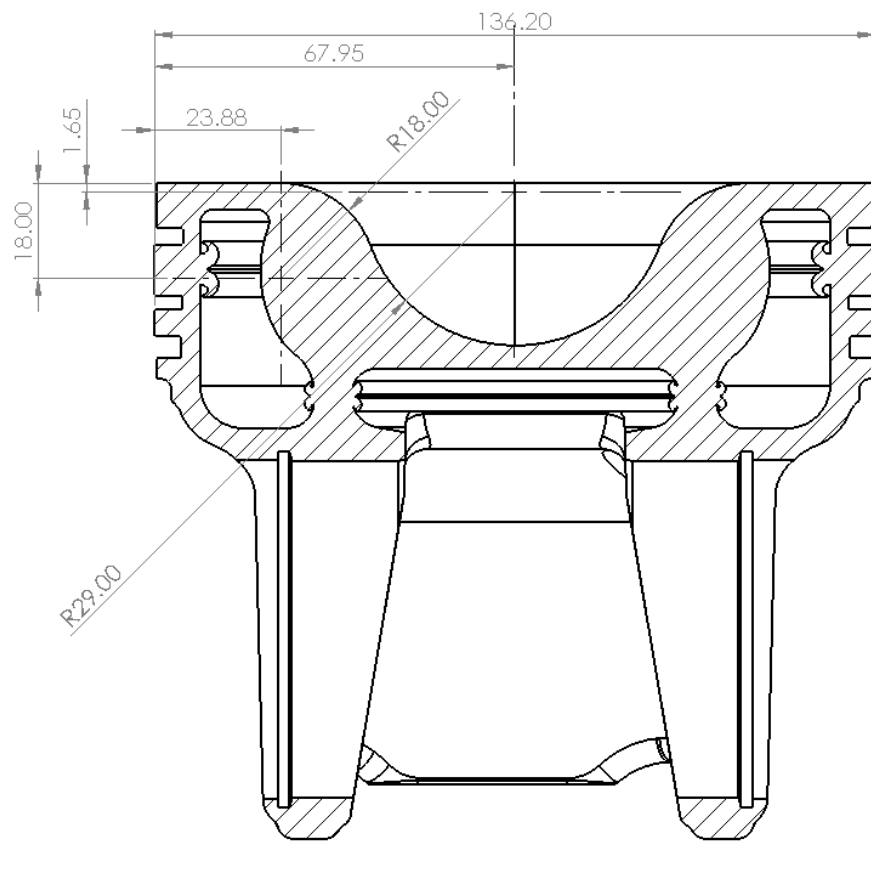


Figure Appendix - 5. LECM mounted and wired on the X15 SCE test cell.



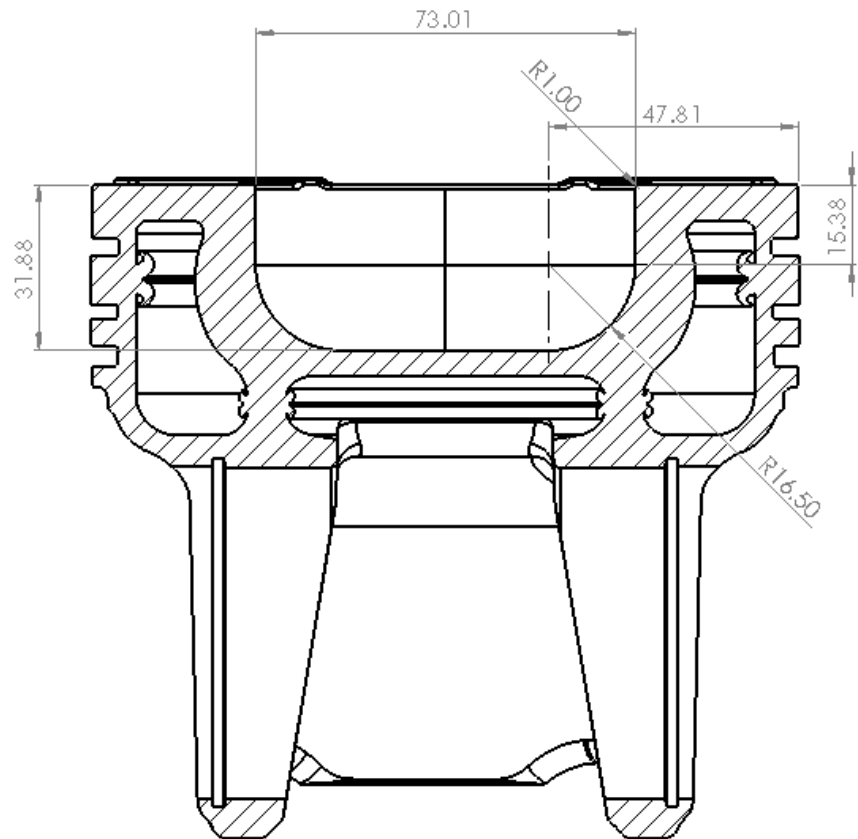
Figure Appendix - 6. Orifice plate flow measurement system. Natural gas mass flow measurement. Identical set up used on EGR cart, and Air flow measurement.

The following figures provide detailed dimensions of the piston bowl designs used on the prototype piston tested in the X15 SCE. No complete drawings for the piston are provided as the original casting is a proprietary Cummins Inc. design.



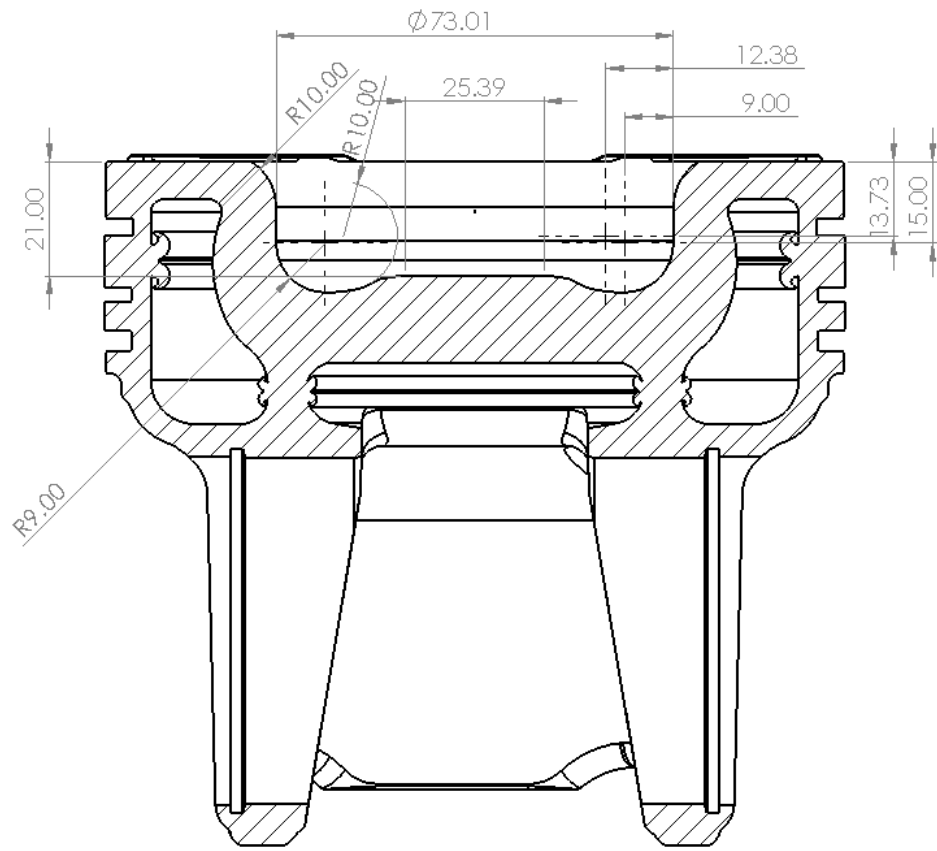
SECTION L-L

Figure Appendix - 7. Piston A bowl dimensions.



SECTION J-J

Figure Appendix - 8. Piston B bowl dimensions.



SECTION D-D
Figure Appendix - 9. Piston C bowl dimensions.

2

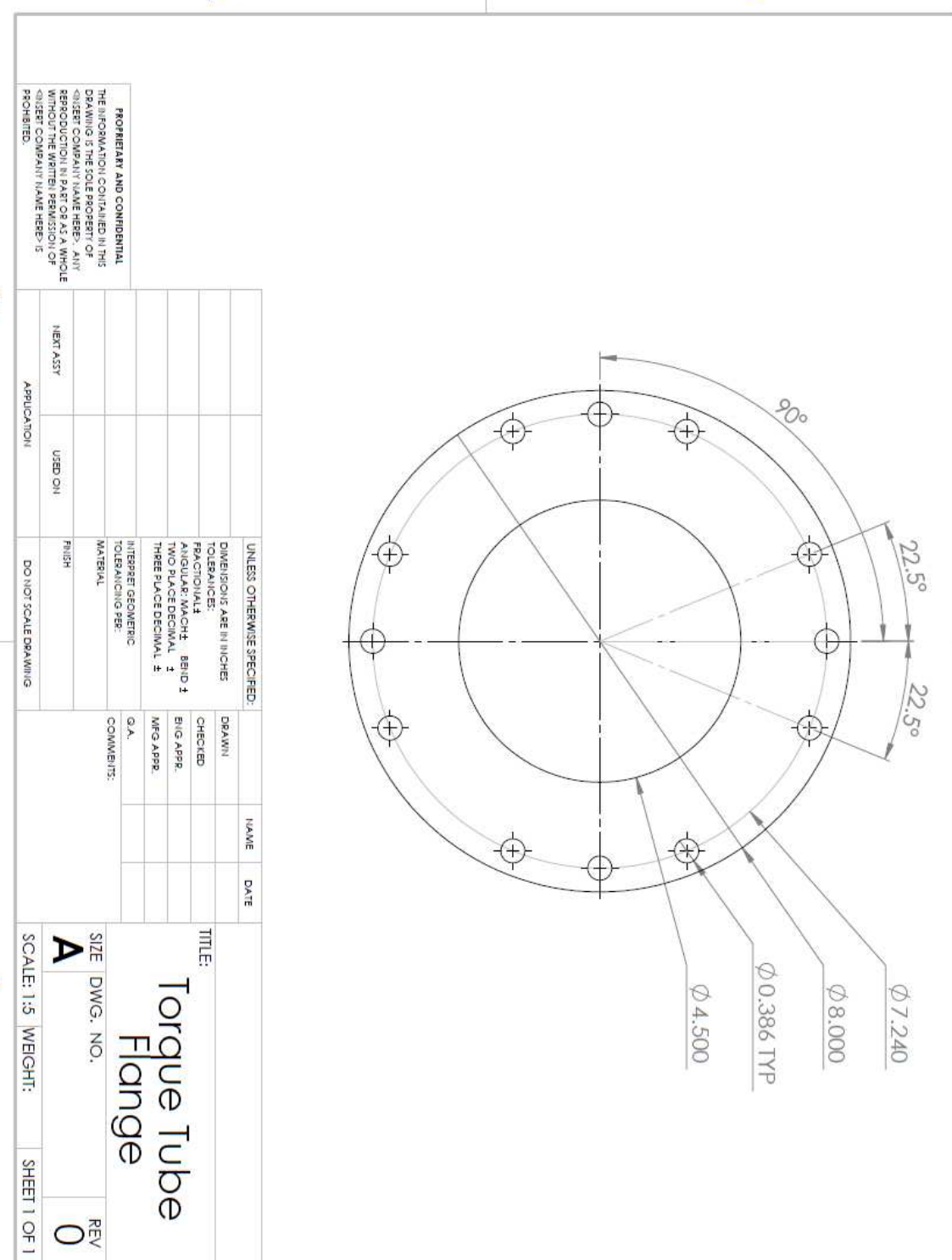
1

B

B

A

A



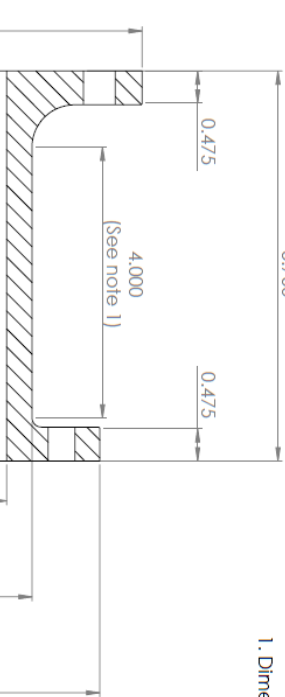
2

1

4
3
2
1

Notes:
1. Dimension is straight section length between fillets.

B



$\phi 8.500$

0.475

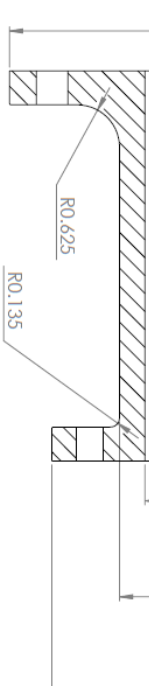
4.000

0.475

(See note 1)

$\phi 4.500$ $\phi 5.250$ $\phi 7.250$

A



R0.625

R0.135

Section View

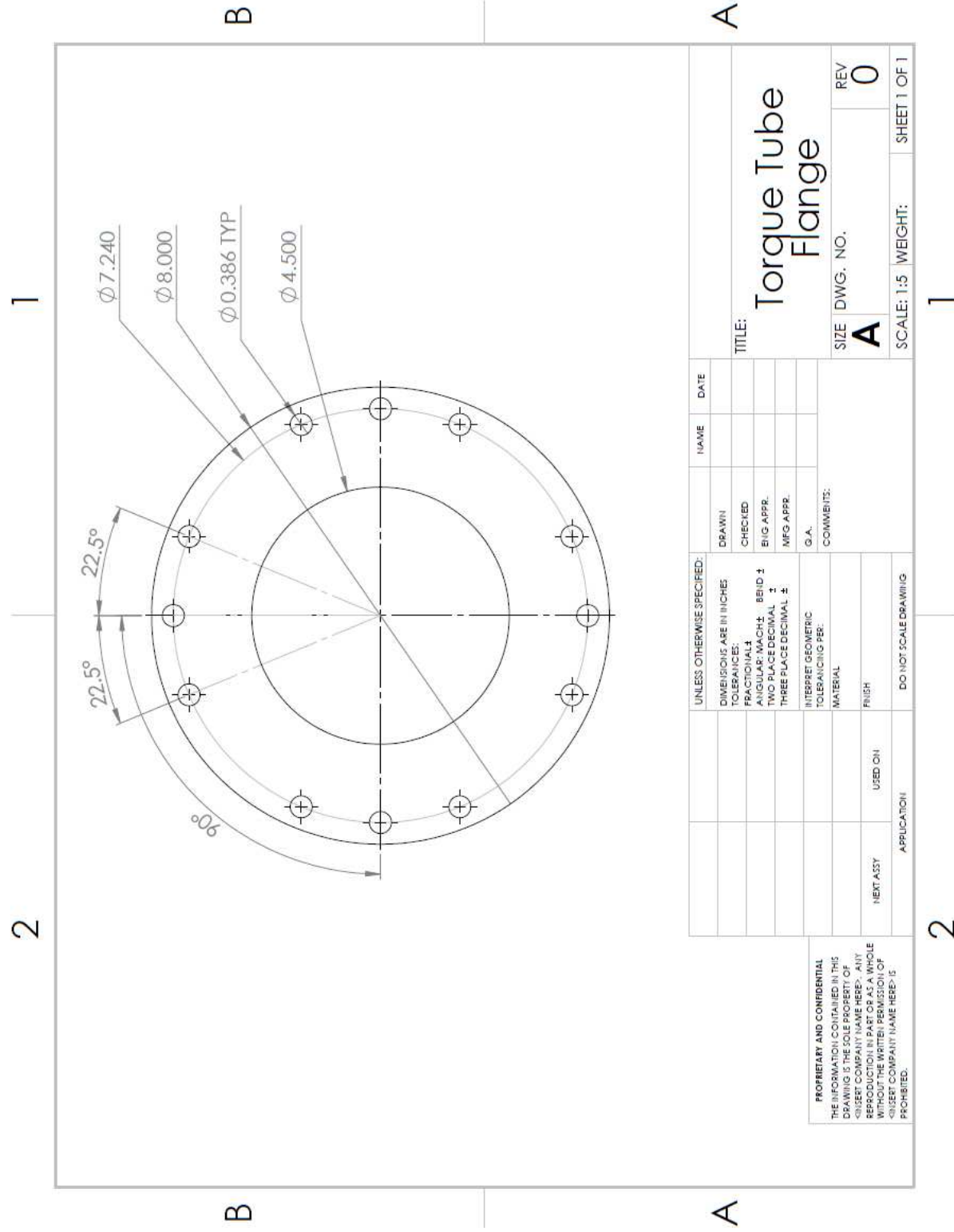
A

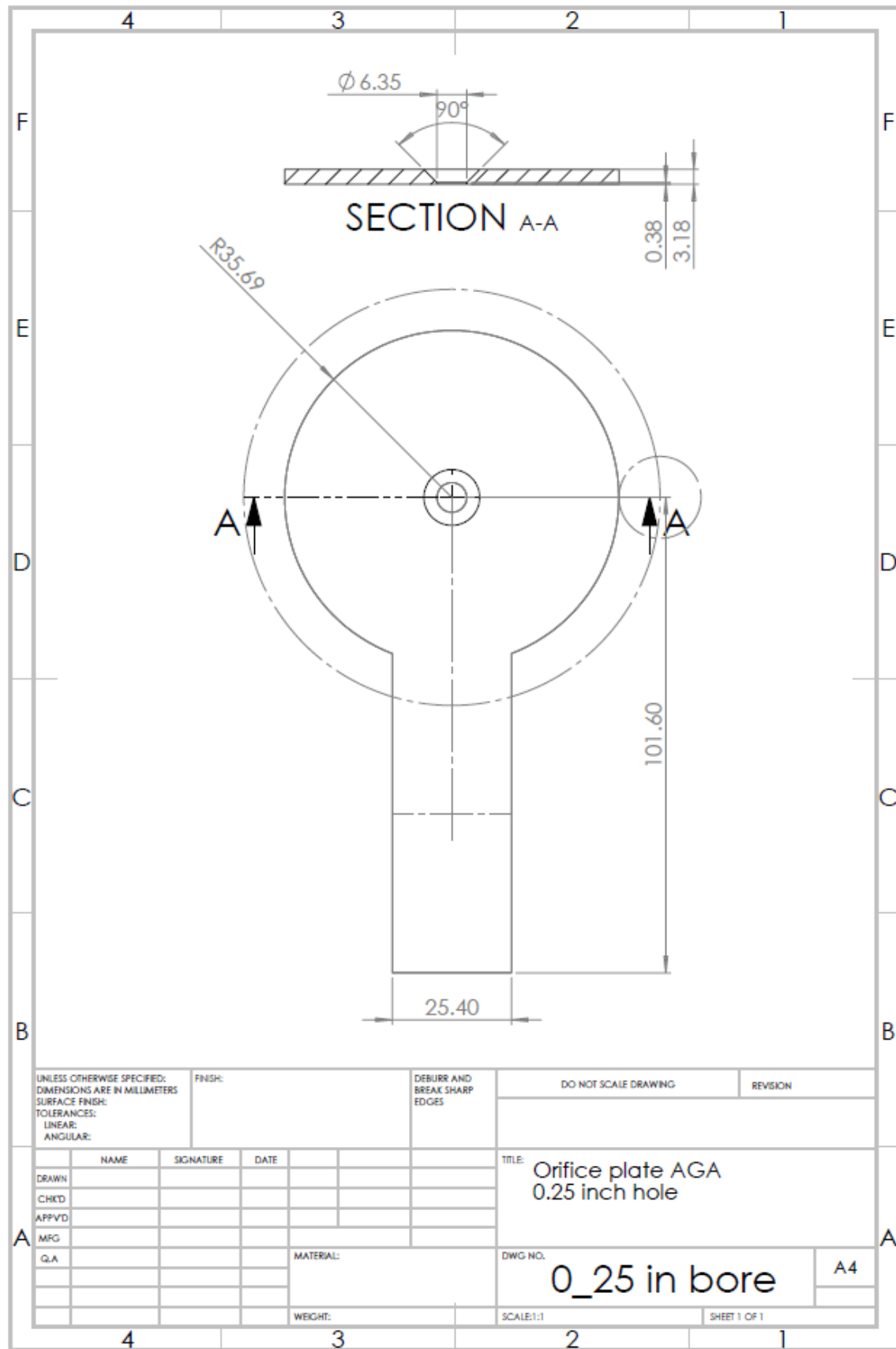
UNLESS OTHERWISE SPECIFIED:		NAME	DATE	TITLE:
DIMENSIONS ARE IN INCHES		DESIGN		
TO BE MAINTAINED		CHECKED		
FRACTIONAL				
ANGLES, LENGTHS, SPACINGS, ETC.,	SEE D			
ARE TO BE EXACT				
NOTICE: THIS DRAWING IS THE PROPERTY OF				
THE ENGINEER WHO MADE IT				
REPRODUCTION OR PART OR AS A WHOLE				
OR PART THEREOF, BY OTHER THAN THE				
ORIGINAL COMPANY NAME HEREIN, ANY				
REPRODUCTION IN PART OR AS A WHOLE				
OR PART THEREOF, BY OTHER THAN THE				
ORIGINAL COMPANY NAME HEREIN,				
IS PROHIBITED.				

INTERFERENT GEOMETRIC TOLERANCING PER:		COMMENTS:	SIZE	DWG. NO.	REV
MATERIAL	FINISH				
NEW ASSY	USED ON			B	Torque Tube Rev3
APPLICATION	DO NOT SCALE DRAWING			3	3

SCALE	WEIGHT	SHEET
1:5		1 OF 3

4
3
2
1





LECM wiring diagram.

The wiring diagram was provided by Woodward Inc., and it was designed by Jeff Carlson.

